8-2012

Iron Pnictides: Superconductivity in Multi-Orbital Systems

Andrew David Nicholson
anicho13@utk.edu

Recommended Citation

Nicholson, Andrew David, "Iron Pnictides: Superconductivity in Multi-Orbital Systems. " PhD diss., University of Tennessee, 2012.
https://trace.tennessee.edu/utk_graddiss/1411

To the Graduate Council:

I am submitting herewith a dissertation written by Andrew David Nicholson entitled "Iron Pnictides: Superconductivity in Multi-Orbital Systems." I have examined the final electronic copy of this dissertation for form and content and recommend that it be accepted in partial fulfillment of the requirements for the degree of Doctor of Philosophy, with a major in Physics.

Adriana Moreo, Major Professor

We have read this dissertation and recommend its acceptance:

Elbio Dagotto, Michael Guidry, Janice Musfeldt

Accepted for the Council:
Dixie L. Thompson

Vice Provost and Dean of the Graduate School

(Original signatures are on file with official student records.)

Iron Pnictides: Superconductivity in Multi-Orbital Systems

A Thesis Presented for
The Doctor of Philosophy
Degree
The University of Tennessee, Knoxville

Andrew Nicholson

May 2012

To my loving son, Max

Acknowledgements

I would like to thank to Professor Adriana Moreo for directing my research project and thesis. Her insight and knowledge has been a source of inspiration and support. I am also grateful to Dr. Maria Daghofer, who taught me so much about physics, computers and the world. I am also thankful to Professor Elbio Dagotto who's direction made everything possible. Professor Jose Riera provided me with foundation of the Lanczos code used in this thesis. Without his patience and assistance, I would not have been able to finish this work.

I am also grateful for the support of the U. S. Department of Energy, Office of Basic Energy Sciences, Materials Sciences and Engineering Division, and also by the National Science Foundation under grand DMR-1104386.

I would also like to thank my parents, Blythe Tennent and Roger Nicholson for their support and infinite patience.

There is a theory which states that if ever anybody discovers exactly what the Universe is for and why it is here, it will instantly disappear and be replaced by something even more bizarre and inexplicable. There is another theory which states that this has already happened.

Douglas Adams - *The Hitchhiker's Guide to the Galaxy*

Abstract

This work focuses on the development and implementation of microscopic models as well as their numerical and analytical study to elucidate the properties of the iron pnictides. There are many first principle and phenomenological studies of these materials, but there is a need for unbiased numerical calculations following an approach similar to the one used in the study of the Hubbard and t-J models for the cuprates.

First a two orbital model for the pnictides, focusing on two hybridized Fe-d orbitals (d_{xz} and d_{yz}) is formulated, including hoppings between nearest and next nearest neighbors as well as on site Coulomb interactions. This model is studied numerically on a tilted 8-site cluster. The magnetic tendencies and the pairing operators allowed by lattice and orbital symmetries are calculated including a study of which of these operators are favored in the model.

Next, Heisenberg terms, deduced from a strong coupling expansion, are added to enhance magnetic order found experimentally as well as to increase carrier attraction. Superconducting pairing symmetries are studied in both the hole and electron doped cases. In both cases, many pairing symmetries compete (A_{1g}, B_{2g}, B_{1g}) in the physical parameter regime suggesting that small changes in parameters may render any of these three channels stable. In the hole doped case, ground states with pseudocrystal momentum $\mathbf{k}$=(π,π) in the unfolded Brillouin zone are found. In the two Fe-atom unit cell, this indicates that the ground state involves anti-bonding, rather than bonding, combinations of the orbitals. The lowest state with **k**=(0,0) has only a slightly higher energy and may become the favored state in some regions of parameter space.

To investigate the role that degeneracy, hybridization and nesting play in the origin of magnetic order in the pnictides we introduce a phenomenological two orbital model composed of non-hybridized bands. Using a variety of techniques, in the weak coupling regime it is shown that only the model with hybridized bands develops magnetic order while the other does not have local magnetization. However, both models display similar insulating magnetic order in the strong coupling limit. These results indicate that nesting is a necessary but not sufficient condition for the development of ordered states with local magnetization in multi-orbital Hubbard systems; the additional requirement is that the nested portions of the bands have the same orbital flavor. This condition can be achieved via strong hybridization of the orbitals in the weak coupling limit or via Fermi surface reconstruction induced by Coulomb interactions in the strong coupling regime.

Finally, a three orbital model is developed which, in addition to the Fe 3-d_{xz} and d_{yz} orbitals, takes into account the Fe 3-d_{xy} orbital, which is found to have weight in a small region around the Fermi surface in bandstructure calculations. Mean field calculations are performed guided by the results of the two orbital model. The proceeds of this work include the discovery of four distinct magnetic phases in the model as well as the tabulation of a variety of pairing operators and their single particle spectral functions to be compared with experimental observations. Good agreement is found between both models for the magnetic tendencies and pairing symmetries.

Contents

List of Tables

List of Figures

Chapter 1

Introduction

Since the discovery in 2008 of superconducting transition temperatures in $\mathrm{LaFeAsO}_{1-x}\mathrm{F}_x$ up to T_c=26 K, there has been much research performed in this new family of superconductors [Kamihara et al. (2008); Chen et al. (2008a,b); Wen et al. (2008); Chen et al. (2008c); Ren et al. (2008c,b,a)]. The record critical temperature in these materials, 55 K in $\mathrm{SmO}_{1-x}\mathrm{F}_x\mathrm{FeAs}$, [Ren et al. (2008b)] is second only to those observed in the cuprates [Dagotto (1994)]. While crystalline structures of the members of this family differ, one common theme is the presence of iron along with a pnictogen (P, As, Sb) or a chalcogen (S, Se, Te). This work will focus mainly on the pnictogen family and of these the "1111" subgroup, which derives its name from the material's chemistry. Shown in Fig. 1.1 is the structure of LaOFeAs: red solid balls represent Fe atoms, yellow ones As atoms, blue balls O/F atoms and La by green balls. The Fe-As layers form conduction layers while the La-O/F layers are thought of as charge reservoirs. In the Fe-As layers, the iron atoms form a square lattice with As atoms alternating above and below the iron planes. Generally, the crystalline structure of these compounds is tetragonal at room temperature but orthorhombic at low temperature [Zhao et al. (2008)].

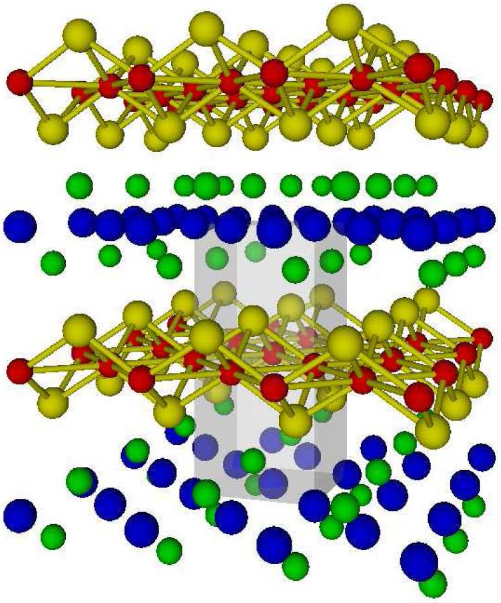

Figure 1.1: The crystalline structure of LaOFeAs as described in text [Graser et al. (2009)].

As in the cuprates, there is considerable evidence that the electron-phonon mechanism is too weak to give rise to the high $\mathrm{T_c}$ observed in iron-based superconductors [Boeri et al. (2008); Higashitaniguchi et al. (2008); Christianson et al. (2008)]. Experiments show that the pnictides share several properties with the high-T_c cuprates, such as the order of magnitude of the critical temperature, [Kamihara et al. (2008)] the existence of magnetic order in some of the parent compounds, [Dong et al. (2008); de la Cruz et al. (2008); Chen et al. (2008d); Krellner et al. (2008); Goldman et al. (2008)] and a possible exotic pairing mechanism [Boeri et al. (2008)]. However, there are differences in several aspects as well: the parent compound is a (bad) metal instead of a Mott insulator, [Dong et al. (2008); de la Cruz et al. (2008); Chen et al. (2008d); Krellner et al. (2008); Goldman et al. (2008)] which suggests that the regime of a large Hubbard coupling U, widely used in the context of the cuprates, may not be appropriate for a theoretical description of the pnictides. Although Fe-based and Cu-based superconductors have similar layered structure, the mechanisms of electron conduction are very different. In many of the cuprates, electrons move from

Cu to Cu via O atoms located in between nearest neighbor Cu atoms. Thus, nearest neighbor hoppings have much higher amplitudes than diagonal next nearest neighbor hoppings. In the pnictides, electrons move from Fe to Fe atom via As atoms which lie above or below the midpoint between diagonal next nearest neighbor Fe atoms. In this picture electrons move about the same distance to go between nearest neighbor and diagonal next nearest neighbor Fe sites making the hopping amplitudes of these two movements similar in magnitude. Also, several orbitals, as opposed to only one, have to be considered in order to reproduce the Fermi surface, which consists of hole and electron pockets [Lebegue (2007); Xu et al. (2008); Cao et al. (2008); Hai-Jun et al. (2009)]. Several band-structure calculations have shown that the Fermi surface of these and related compounds is made out of two small hole pockets centered at the Γ point, and small electron pockets at the X and Y points, in the notation corresponding to a square lattice of Fe atoms [Lebegue (2007); Singh and Du (2008); Xu et al. (2008); Cao et al. (2008); Hai-Jun et al. (2009)]. These calculations have also shown that the $3d$ levels of Fe play the dominant role in establishing the properties of these materials near the Fermi level. In addition, while clear experimental evidence and theoretical calculations indicate that the pairing state in the cuprates is nodal and has d-wave symmetry, [Dagotto (1994)] the properties of the pairing operator in the pnictides have not yet been well established. Experimentally, several angle resolved photo-emission (ARPES) studies [Kondo et al. (2008); Ding et al. (2008); Nakayama et al. (2009); Wray et al. (2008); Kim et al. (2010)] show constant nodeless gaps on all Fermi surfaces (FSs), but evidence for the existence of nodal gaps has been reported in many transport measurements as well [Shan et al. (2008); Gang et al. (2008); Ahilan et al. (2008); Nakai et al. (2008); Grafe et al. (2008); Wang et al. (2009b); Matano et al. (2008); Mukuda et al. (2008); Millo et al. (2008); Wang et al. (2009a); Dong et al. (2010)]. Even though the symmetry of the pairing operator is still in debate, a variety of experimental results suggest that the Cooper pairs are spin singlets [Grafe et al. (2008); Matano et al. (2008); Kawabata et al. (2008)].

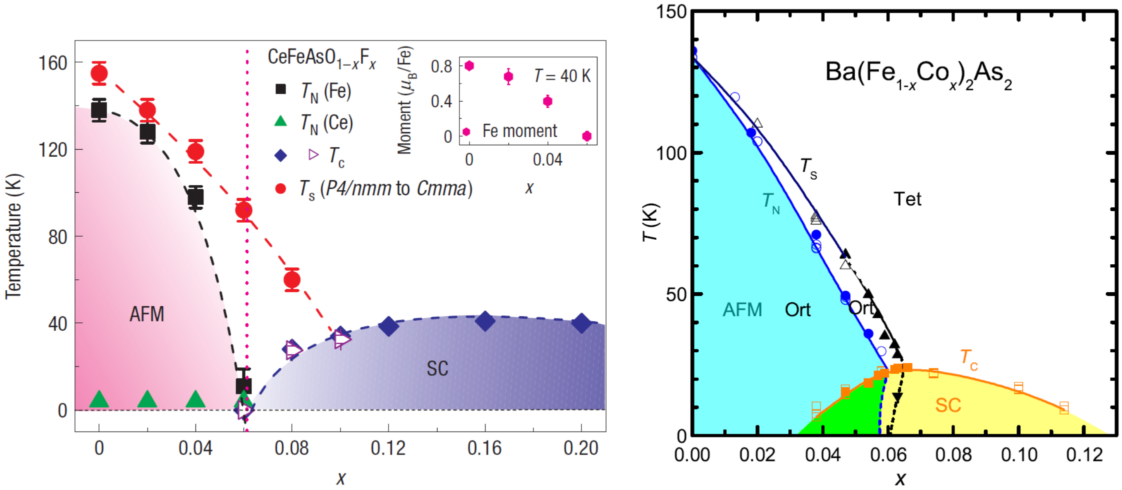

Figure 1.2: Temperature versus composition of 1111-type electron-doped polycrystalline CeFeAs$_{1-x}$F$_x$ [Zhao et al. (2008)] and 122-type electron doped single crystalline Ba(Fe$_{1-x}$Co$_x$)$_2$As$_2$ [Nandi et al. (2010)].

The undoped parent compound has long-range spin order in the ground state of most of the compounds [Dong et al. (2008)]. This colinear magnetic state has Fe spins along one of the Fe-Fe crystal axes ferromagnetically ordered, and is antiferromagnetically ordered in the perpendicular direction. According to neutron scattering experiments, in LaOFeAs the transition to this magnetic state occurs at 134 K, and the magnetic moment is 0.36 μ_B, which is smaller than anticipated [de la Cruz et al. (2008)]. For NdOFeAs, the Neel temperature is 141 K [Chen et al. (2008d)] and the magnetic moment is even smaller 0.25 μ_B. On the other hand, in resistivity, specific heat, and magnetic susceptibility measurements, the antiferromagnetic Neel temperature of SrFe$_2$As$_2$ was reported to be as high as 205 K, with a more robust Fe magnetic moment of value 1.7 μ_B [Krellner et al. (2008)]. Also, CaFe$_2$As$_2$ was investigated using neutron diffraction, and a Neel temperature 173 K with a moment 0.8 μ_B was reported [Goldman et al. (2008)]. Thus, although originally it was believed that the undoped materials had a very weak magnetic state, most recent results suggest that the colinear spin order may be very robust at least in some materials.

Experimentally, the phase diagrams (see Fig. 1.2) with hole or electron doping show competition between magnetism and superconductivity. For some materials, as in CeFeAsO, [Zhao et al. (2008)] the magnetic ordered phase is completely suppressed by superconductivity with F doping. For others such as SmFeAsO, [Nandi et al. (2010)] the magnetism is partly suppressed by superconductivity, resulting in coexistence of magnetism and superconductivity, which is a very interesting feature of iron-based superconductors, as well as cuprates [Dagotto (1994)]. It is believed that optimal superconductivity happens when the long-range SDW order is suppressed by doping or pressure, but dynamic short-range antiferromagnetic spin correlations survive [Johnston (2010)].

1.1 Overview

The research presented in this work focuses on the development and implementation of microscopic models as well as their numerical and analytical study to elucidate the properties of the pnictides. There are many first principle and phenomenological studies of these materials, but there is a need for unbiased numerical calculations following an approach similar to the ones used in the study of the Hubbard and t-J models for the cuprates [Dagotto (1994)]. The big difference between the study of these materials and the study of the cuprates, is the multi-orbital nature of the former compared to the single orbital character in the latter. The addition of more orbitals increases the complexity of the problem greatly. Because of this, there is a need to develop models which capture the basic physics of the pnictides with the smallest amount of degrees of freedom.

First, a two orbital model [Moreo et al. (2009b)] for the iron pnictides will be discussed in Chapter 2. This model focuses on two of the five Fe-3d orbitals, the Fe d_{xz} and d_{yz}. These orbitals are the most robust at the FS [Boeri et al. (2008)] and neglects the Fe d_{xy} orbital, which is found to have weight in a small part of the electron pockets, [Graser et al. (2009); Hai-Jun et al. (2009); Vildosola et al. (2008)]

see Fig 2.1. Its strength lies on its simplicity and the fact that it can be studied numerically. Numerical calculations on a tilted 8-site lattice will be performed. The magnetic properties as well as the pairing operators allowed by lattice and orbital symmetries will be studied.

In order to increase the strength of colinear magnetic order in the two orbital model and to enhance tightly bound-states upon doping, Heisenberg interactions will be introduced in Chapter 3. Both electron doping (Section 3.3) and hole doping (Section 3.4) cases will be considered. The effect of the Heisenberg terms on the magnetic order as well as favored superconducting pairing symmetries will be investigated.

In Chapter 4, to investigate the role of orbital hybridization and Fermi surface nesting in the origin of magnetic order in the pnictides, a phenomenological two orbital model consisting of two non-hybridized s-like orbitals will be compared to the two orbital model composed of hybridized Fe d-orbitals. The magnetic properties of both models will be discussed using Lanczos, mean field, and RPA methods.

In order to evaluate the merits and shortcomings of the two-orbital model, a three orbital mode was developed, see Chapter 5, taking into account the Fe d_{xy} orbital. The introduction of the third orbital makes numerical calculations unviable since the size of the Hilbert space becomes too large to perform Lanczos calculations on reasonably sized lattices. Instead, mean field calculations were performed guided by the numerical results in the two orbital model. The proceeds of this work include an investigation of the magnetic properties as well as the calculation of the spectral functions for a variety of superconducting pairing operators to be compared with experimental observations.

Before the presentation of these investigations a brief overview of the models and methods described in the main text is presented. The Hubbard model for multi-orbital systems will be introduced in Section 1.2, followed by a discussion on exact diagonalization, seen in Section 1.3.

1.2 Multi-orbital Hubbard Model

In systems where electron correlations in the d orbitals are important, the competition between localized and itinerant behavior is a difficult problem. One of the main consequences of electron correlation is the formation of localized magnetic moments, as described in the Heisenberg model. However, since the d electrons frequently contribute to the transport properties, these moments cannot be entirely localized. One of the first models proposed to deal with this challenge was put forth by Hubbard [Hubbard (1963)], who considered on-site Coulomb repulsion for electrons in a single band. A simple derivation of this model follows. The field operator for an electron with a given spin σ can be written as [Oles (1983)]

$$\psi_\sigma(\vec{x}) = \sum_i \psi_i(\vec{x}) d_{i,\sigma} \tag{1.1}$$

where $d_{i,\sigma}$ is the annihilation operator for an electron at site i of a crystal lattice with spin σ and $\psi_i(\vec{x})$ are the wave functions at site i in the lattice. The Hamiltonian, in second-quantization formalism, is:

$$\begin{aligned} H =& \sum_\sigma \int d^3x \psi_\sigma^\dagger(\vec{x})(-\frac{\hbar^2}{2m}\nabla^2 + V_1(\vec{x}))\psi_\sigma(\vec{x}) \\ &+ \frac{1}{2}\sum_{\sigma,\sigma'} \int d^3x d^3x' \psi_\sigma^\dagger(\vec{x})\psi_{\sigma'}^\dagger(\vec{x}')V_2(\vec{x}-\vec{x}')\psi_{\sigma'}^\dagger(\vec{x}')\psi_\sigma^\dagger(\vec{x}) \end{aligned} \tag{1.2}$$

where $\mathrm{V}_1(\vec{x})$ is the effective potential composed of the ionic potentials of single atoms and $\mathrm{V}_2(\vec{x}-\vec{x}')$ is the electron-electron interaction potential. The first term in Eqn. 1.2 describes an electron moving through an external potential $\mathrm{V}_1(\vec{x})$, with parameters given by [Oles (1983)]

$$t_{i,j} = \sum_\sigma \int d^3x \psi_i^\dagger(\vec{x})[-\frac{\hbar^2}{2m}\nabla^2 + V_1(\vec{x})]\psi_j(\vec{x}). \tag{1.3}$$

The second term contains electron-electron interactions. Since the d wave functions are well localized [Hubbard (1963)], inter-site interactions are much weaker than on-site ones and thus only on-site interactions will be considered. Also, due to the symmetry of the d functions, matrix elements must contain even powers of each wave function ψ_i. Taking all of this into consideration the Hamiltonian in Eqn. 1.2 may be written as:

$$H = \sum_{i,j} [t_{i,j} d^{\dagger}_{i,\sigma} d_{j,\sigma} + h.c.] + \sum_{i} U_{i,\uparrow} n_{i,\uparrow} n_{i,\downarrow} \tag{1.4}$$

where $n_{i,\sigma} = d^{\dagger}_{i,\sigma} d_{i,\sigma}$ is the number operator, and the interaction parameter, U, can be expressed as:

$$U = \int d^3x d^3x' |\psi_i(\vec{x})|^2 V_2(\vec{x} - \vec{x}') |\psi_i(\vec{x}')|^2. \tag{1.5}$$

This is the single band Hubbard model.

As was discussed in the Introduction, the pnictides require more than one orbital to reproduce the Fermi surface. Taking this additional degree of freedom into account, the field operators, $\psi_\sigma(\vec{x})$ defined in Eqn. 1.1, become:

$$\psi_\sigma(\vec{x}) = \sum_{i} \sum_{\alpha} \psi_{i,\alpha}(\vec{x}) d_{i,\alpha,\sigma} \tag{1.6}$$

where $d_{i,\alpha,\sigma}$ is the annihilation operator for an electron with spin σ, at site i, in orbital α, and $\psi_{i,\alpha}(\vec{x})$ are the wave functions at site i and orbital α. An equation identical to Eqn. 1.2 can be obtained in terms of $\psi_\sigma(\vec{x})$ defined in Eqn. 1.6. However, now the movement of electrons through the lattice is more complex with orbital dependent hoppings given by:

$$t^{\alpha,\beta}_{i,j} = \sum_{\sigma} \int d^3x \psi^{\dagger}_{i,\alpha}(\vec{x}) [-\frac{\hbar^2}{2m} \nabla^2 + V_1(\vec{x})] \psi_{j,\beta}(\vec{x}). \tag{1.7}$$

where $t_{i,j}^{\alpha,\beta}$ now allows electrons to "hop" between lattice sites i and j, and atomic orbitals α and β. Using the Hubbard argument once again (only considering on-site interactions), but allowing both intra- and inter-orbital interactions, the multi-orbital analog of Eqn. 1.4 becomes [Oles (1983)]:

$$\begin{aligned}H = &\sum_{i,j,\alpha,\beta}[t_{i,j}^{\alpha,\beta}d_{i,\alpha,\sigma}^{\dagger}d_{i,\beta,\sigma} + h.c.] + \sum_{i,\alpha}U_{\alpha,\alpha}n_{i,\alpha,\uparrow}n_{i,\alpha,\downarrow}\\ &+ \sum_{i,\alpha,\beta,\sigma}U_{\alpha,\beta}n_{i,\alpha,\sigma}n_{i,\beta,-\sigma} + \sum_{i,\alpha,\beta,\sigma}(U_{\alpha,\beta} - J_{\alpha,\beta})n_{i,\alpha,\sigma}n_{i,\beta,\sigma}\\ &- \sum_{i,\alpha,\beta,\sigma}J_{\alpha,\beta}d_{i,\alpha,\sigma}^{\dagger}d_{i,\alpha,-\sigma}d_{i,\beta,-\sigma}^{\dagger}d_{i,\beta,\sigma} + \frac{1}{2}\sum_{i,\alpha,\beta,\sigma}J_{\alpha,\beta}d_{i,\alpha,\sigma}^{\dagger}d_{i,\alpha,-\sigma}^{\dagger}d_{i,\beta,-\sigma}d_{i,\beta,\sigma}\end{aligned} \tag{1.8}$$

where the summations over α, β run only once over each pair of orbital indices. Neglecting crystal-field effects, all of the d orbitals are equivalent, so the inter-orbital parameters $\mathrm{U}_{\alpha,\beta}$ and $\mathrm{J}_{\alpha,\beta}$ become independent of the orbital indices α, β so that the interaction parameters can be expressed as:

$$\begin{aligned}U_{\alpha,\alpha} =&U = \int d^3xd^3x'|\psi_{i,\alpha}(\vec{x})|^2V_2(\vec{x}-\vec{x}')|\psi_{i,\alpha}(\vec{x}')|^2,\\ U_{\alpha,\beta} =&U' = \int d^3xd^3x'|\psi_{i,\alpha}(\vec{x})|^2V_2(\vec{x}-\vec{x}')|\psi_{i,\beta}(\vec{x}')|^2,\\ J_{\alpha,\beta} =&J = \int d^3xd^3x'\psi_{i,\alpha}^*(\vec{x})\psi_{i,\beta}^*(\vec{x}')V_2(\vec{x}-\vec{x}')\psi_{i,\alpha}(\vec{x}')\psi_{i,\beta}(\vec{x}).\end{aligned} \tag{1.9}$$

This imposes a new condition on the model parameters

$$U = U' + 2J \tag{1.10}$$

so that our model Hamiltonian can be rearranged as

$$\begin{aligned}H = &\sum_{i,j,\alpha,\beta,\sigma}[t_{ij}^{\alpha\beta}d_{i,\alpha,\sigma}^{\dagger}d_{j,\beta,\sigma} + h.c.] + U\sum_{i,\alpha}n_{i,\alpha,\uparrow}n_{i,\alpha,\downarrow} + (U' - \frac{1}{2}J)\sum_{i,\alpha,\beta}n_{i,\alpha}n_{i,\beta}\\ &- 2J\sum_{i,\alpha,\beta}S_{i,\alpha}\cdot S_{i,\beta} + J\sum_{i,\alpha,\beta}d_{i,\alpha,\uparrow}^{\dagger}d_{i,\alpha,\downarrow}^{\dagger}d_{i,\beta,\downarrow}d_{i,\beta,\uparrow}\end{aligned} \tag{1.11}$$

where the spin density in orbital α at site i is denoted by $S_{\mathbf{i},\alpha} = d^{\dagger}_{\mathbf{i},\alpha,a}\bar{\sigma}_{a,b}d_{\mathbf{i},\alpha,b}$, $\bar{\sigma}_{a,b}$ are the Pauli matrices, $n_{\mathbf{i},\alpha}$ is the electronic density in orbital α at site i. The first term represents the tight-binding movement of electrons in the lattice. The values of $t^{\alpha\beta}_{ij}$ depend on the geometry of the lattice and, thus, their values are material dependent. Sections 2.2 and 5.1 of this thesis are devoted to the calculation of the tight-binding parameters for the pnictides. The second (third) term represents on-site intraorbital (interorbital) repulsion between electrons. The fourth term is the Hund's rule spin coupling that favors the ferromagnetic alignment of spins in different orbitals at the same lattice site. Finally, the last term corresponds to "pair-hopping" and its coupling is equal to J by symmetry.

1.3 Exact Diagonalization - Lanczos Method

In the study of models of strongly correlated electrons, solutions involving mean field and variational approximations are self-consistent, but it is hard to see if they actually describe the properties of the actual ground state (rather than an excited state). To find the ground state of Hubbard-like models, unbiased methods are important and are useful to guide other calculations. One of these methods, exact diagonalization, allows one to obtain the ground state of the Hamiltonian on a finite lattice while keeping all basis states. In order to find the ground state eigenvector in the very large Hubbard Hilbert space, a Lanczos algorithm will be employed (see Sections 2.4, 3.3, 3.4, 4.3.2, 4.3.3).

The basic idea of the Lanczos algorithm is to take a large sparse Hamiltonian matrix and iteratively reconstruct the basis such that the Hamiltonian has a tridiagonal form. Once in tridiagonal form, standard linear algebra libraries can be used to diagonalize the Hamiltonian matrix quickly. To begin, a random vector in the Hilbert space of our Hamiltonian $|\phi_0\rangle$ is chosen [Dagotto (1994)]. To determine the next basis vector, the Hamiltonian $\hat{H}$ is applied to $|\phi_0\rangle$ and subtract the projection over $|\phi_0\rangle$:

$$|\phi_1\rangle = \hat{H}|\phi_0\rangle - \frac{\langle\phi_0|\hat{H}|\phi_0\rangle}{\langle\phi_0|\phi_0\rangle}|\phi_0\rangle \tag{1.12}$$

which is orthogonal to $|\phi_0\rangle$. Next, a second basis vector can be generated which is orthogonal to $|\phi_0\rangle$ and $|\phi_1\rangle$

$$|\phi_2\rangle = \hat{H}|\phi_1\rangle - \frac{\langle\phi_1|\hat{H}|\phi_1\rangle}{\langle\phi_1|\phi_1\rangle}|\phi_1\rangle - \frac{\langle\phi_0|\hat{H}|\phi_1\rangle}{\langle\phi_0|\phi_0\rangle}|\phi_0\rangle \tag{1.13}$$

After several iterations the basis vectors can be generalized as:

$$|\phi_{n+1}\rangle = \hat{H}|\phi_n\rangle - a_n|\phi_n\rangle - b_n^2|\phi_{n-1}\rangle \tag{1.14}$$

where n=0, 1, 2 ..., and the nonzero coefficients are

$$a_n = \frac{\langle\phi_n|\hat{H}|\phi_n\rangle}{\langle\phi_n|\phi_n\rangle}, b_n = \frac{\langle\phi_{n-1}|\hat{H}|\phi_n\rangle}{\langle\phi_{n-1}|\phi_{n-1}\rangle} \tag{1.15}$$

Also note that b_0=0 and $|\phi_{-1}\rangle = 0$. In this new basis the Hamiltonian becomes tridiagonal

$$H = \begin{vmatrix} a_0 & b_1 & 0 & 0 & \ldots \\ b_1 & a_1 & b_2 & 0 & \ldots \\ 0 & b_2 & a_2 & b_3 & \ldots \\ 0 & 0 & b_3 & a_3 & \ldots \\ \vdots & \vdots & \vdots & \vdots & \end{vmatrix}.$$

Standard library subroutines can now diagonalize this matrix easily. In order to diagonalize the full system the number of iterations equal to the size of the Hilbert space would be required. This would take a lot of CPU time. However, if only the ground state of the system is desired only a small number of iterations are required.

Even though the ground state properties of the system being studied can be found with relatively few iterations, the size of the Hilbert space poses problems. The model Hamiltonians used in this work are studied on finite clusters, with N sites. For single orbital models, the size of the Hilbert space grows as 4^N, since there are four possible electron configurations per site (empty, singly occupied by an electron with spin up or with spin down, or doubly occupied). For models with α orbitals, the Hilbert space grows as $4^{\alpha N}$ because now there are four possible states per site and per orbital. Due to an exponential growth of the Hilbert space with the lattice size memory limitations impose severe restrictions on the size of clusters which can be studied. For example, consider a cluster with N=8 sites with three orbitals (it has the same number of degrees of freedom as a single orbital model in a 24 site cluster). In this case the Hilbert space would include $\approx 2.814 \times 10^{14}$ states which is far beyond the limits of contemporary computers. In this work the Lanczos algorithm will only be used on an N=8 site cluster with two orbitals with periodic boundary conditions (see the eight site cluster in Fig. 1.3. This is the largest lattice size which can be accommodated on present day computers for our calculations.[*] Even though the Hilbert space for these finite clusters becomes very large, the problem can be alleviated by using symmetries of the Hamiltonian to reduce the matrix to block form. One such symmetry is the number of particles in the problem, another is the total spin projection S^z_{total}. If translational invariance exits, the total momentum K is conserved and is a good quantum number. For some lattices rotations and and reflections with respect to the lattice axes are also good quantum numbers.

While lattices containing NxN sites can be solved with Lanczos algorithms other "tilted" square clusters are used that completely cover the two dimensional square lattice [Oitmaa and Betts (1978)]. These special clusters have a "magic number" of sites with N= 4, 8, 10, 16, 18, 20, 26, 32, ... The general rule is N=n^2+m^2, where the positive integers n, m are positive integers that are both even or odd. See Fig. 1.3 for examples.

---

[*] The largest lattice size which has been studied for single orbital models is the 20 site lattice [Tohyama et al. (2005)], which required a supercomputer and large amounts of CPU time.

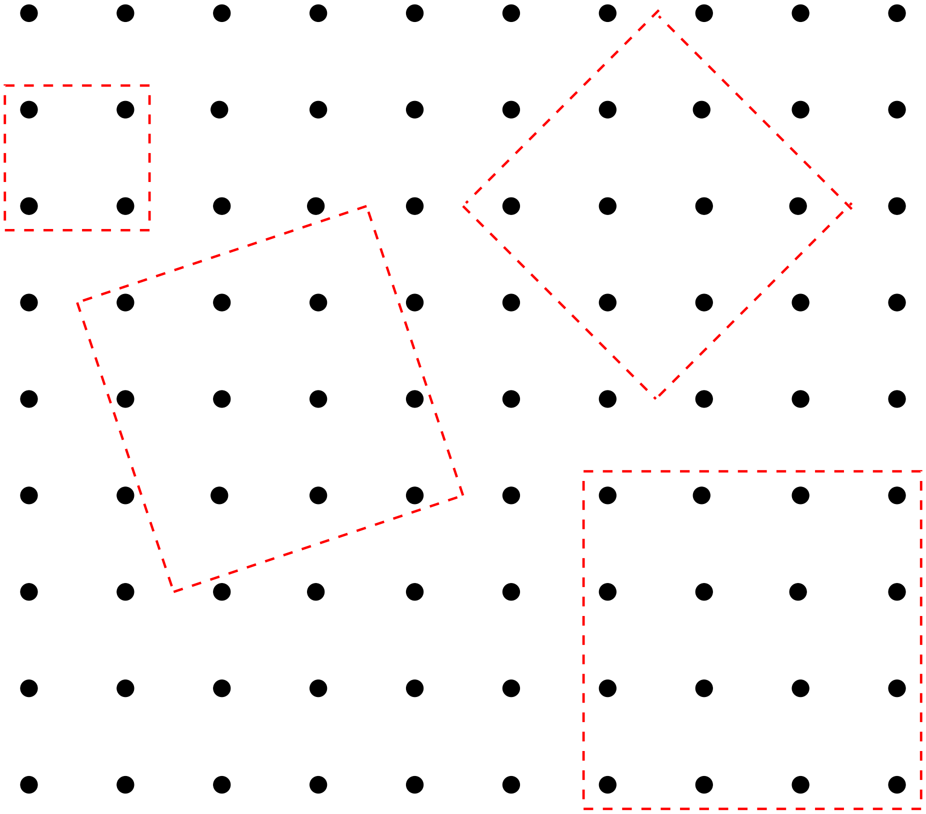

Figure 1.3: Shapes of some lattice clusters described in the text, each of which can be circumscribed by a square.

1.3.1 Dynamical Properties

One attractive feature of the Lanczos method is that it allows the calculation of dynamical properties of model Hamiltonians. In general this means the ability to calculate quantities such as

$$I(\omega) = -\frac{1}{\pi} Im[\langle\psi_0|\hat{O}^\dagger \frac{1}{\omega - E_0 + i\epsilon - \hat{H}} \hat{O}|\psi_0\rangle] \tag{1.16}$$

where $\hat{O}$ is an operator, $|\psi_0\rangle$ is the ground state of the Hamiltonian $\hat{H}$ whose ground-state energy is E (found via the Lanczos method), ω is the frequency and ϵ is a small real number introduced in the calculation to shift the poles of the Green's function into the complex plane. When using a complete basis, the projection $\sum_n |\psi_n\rangle\langle\psi_n| = 1$ and the following identity

$$\frac{1}{x + i\epsilon} = P\frac{1}{x} - i\pi\delta(x) \tag{1.17}$$

which is valid when $\epsilon \to 0$, where x is real and P denotes the principle part, our spectral function is reduced to

$$I(\omega) = \sum_n |\langle\psi_n|\hat{O}|\psi_0\rangle|^2 \delta(\omega - (E_n - E_0)) \tag{1.18}$$

The delta functions in the above equation are in practice approximated by Lorentzians

$$\delta(x) \to \frac{1}{\pi}\frac{\epsilon}{x^2 + \epsilon^2} \tag{1.19}$$

Instead of starting iterations in the Lanczos method with a random vector, it is useful to use the ground state vector ψ_0 found before to define the initial vector

$$|\phi_0\rangle = \frac{\hat{O}|\psi_0\rangle}{\sqrt{\langle\psi_0|\hat{O}^\dagger\hat{O}|\psi_0\rangle}} \tag{1.20}$$

Following [Fulde (1991)], consider the identity:

$$(z-\hat{H})(z-\hat{H})^{-1}=I \tag{1.21}$$

where $z=\omega+E_0+i\epsilon$ and I is the identity matrix. Using the initial vector defined in Eqn. 1.20 along with the Lanczos basis generation procedure defined in Eqn. 1.14, the above identity can be defined in the basis $|\phi_n\rangle$ as:

$$\sum_n (z-\hat{H})_{mn}(z-\hat{H})^{-1}_{np}=\delta_{mp} \tag{1.22}$$

For the special case, n=p=0,

$$(z-\hat{H})_{m0}x_0(z-\hat{H})^{-1}_{00}=\delta_{m0} \tag{1.23}$$

where $x_0=(z-\hat{H})^{-1}_{00}=\langle\phi_0|\frac{1}{(z-\hat{H})}|\phi_o\rangle$ is the quantity of interest. Using Cramer's rule Eqn. 1.23 can be solved for x_0:

$$x_0=\frac{detB_0}{det(z-\hat{H})} \tag{1.24}$$

where the above matrices can be expressed in the basis $|\phi_n\rangle$ as:

$$z-\hat{H}=\begin{vmatrix} z-a_0 & -b_1 & 0 & 0 & \ldots \\ -b_1 & z-a_1 & -b_2 & 0 & \ldots \\ 0 & -b_2 & z-a_2 & -b_3 & \ldots \\ 0 & 0 & -b_3 & z-a_3 & \ldots \\ \vdots & \vdots & \vdots & \vdots & \end{vmatrix}.$$

and

$$B_0 = \begin{vmatrix} 1 & -b_1 & 0 & 0 & \dots \\ 0 & z-a_1 & -b_2 & 0 & \dots \\ 0 & -b_2 & z-a_2 & -b_3 & \dots \\ 0 & 0 & -b_3 & z-a_3 & \dots \\ \vdots & \vdots & \vdots & \vdots & \end{vmatrix}.$$

where the coefficients a_n, b_n were defined in Eqn 1.15. The determinants of these matrices can be expanded as

$$det(z - \hat{H}) = (z - a_0)detD_1 - b_1^2 detD_2 \tag{1.25}$$

$$detB_0 = detD_1 \tag{1.26}$$

where D_n is obtained from 1.3.1 by removing the first n rows and columns. Using Eqns. 1.24 and 1.26, it is clear that

$$x_0 = \frac{detB_0}{det(z - \hat{H})} = \frac{1}{z - a_0 - b_1^2 \frac{detD_2}{detD_1}}. \tag{1.27}$$

The expansion can be continued to find the ratio of the determinants D_1 and D_2

$$\frac{detD_2}{detD_1} = \frac{1}{z - a_1 - b_2^2 \frac{detD_3}{detD_2}}. \tag{1.28}$$

If this procedure is repeated until a full continued fraction is constructed and recalling Eqn. 1.16, final expression for the dynamical response function can be written as:

$$I(\omega) = -\frac{1}{\pi} Im \left| \frac{\langle \psi_0 | \hat{O}^\dagger \hat{O} | \psi_0 \rangle}{z - a_0 - \frac{b_1^2}{z - a_1 - \frac{b_2^2}{z - a_2 - \dots}}} \right| \tag{1.29}$$

These functions will be useful in Sections 3.3.3 and 3.4.5.

Chapter 2

The Two Orbital Model

2.1 Introduction

In order to study the properties of $LaO_{1-x}F_xFeAs$ and related compounds, it is necessary to construct the simplest model which contains the minimum number of degrees of freedom that preserves the essential physics of the problem. Since most of the materials in this family have Fe - X planes (X=As,P...) this work will focus on these layers. Band structure calculations [Boeri et al. (2008)] have shown that Fe $3d$ orbitals carry the greatest weight at the Fermi surface. Of these Fe $3d$ orbitals, the d_{xz} and d_{yz} carry the most weight in the hole and electron pockets, Fig 2.1. Considering these two orbitals is a good staring point for a minimal model for these materials.

In this Chapter the development of a tight-binding two orbital model via the Slater-Koster method [Slater and Koster (1954)] will be shown in Section 2.2. Next, in Section 2.3, on-site Coulomb interactions will be added followed by an investigation of the magnetic tendencies as well as superconducting pairing properties at half filling and with two electrons added will be presented in Section 2.4.

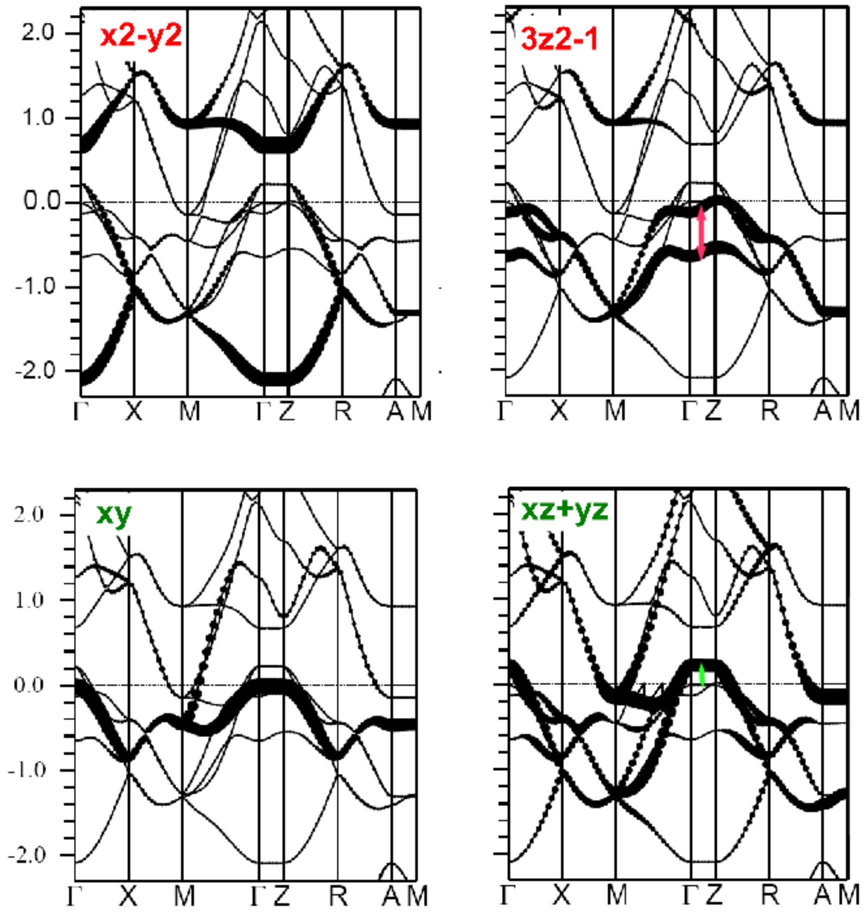

Figure 2.1: Bandstructure of LaOFeAs with the partial characters of the Fe-*d* bands shown by bold circles. The arrows indicate the splitting induced by the elongation/shrinking of the Fe-As tetrahedra [Boeri et al. (2008)].

Table 2.1: Coordinates of atoms in Figure 2.2(a).

Ion	x	y	z
As_0	0	0	-c
Fe_1	k	-k	0
Fe_2	k	k	0
Fe_3	-k	k	0
Fe_4	-k	-k	0
As_1	l	0	c
As_2	0	l	c
As_3	-l	0	c
As_4	0	-l	c

2.2 $LaO_{1-x}F_xFeAs$ Lattice Properties

In order to construct the tight-binding part of the Hamiltonian, it is necessary to calculate orbital overlaps. A cluster of 4 Fe atoms and 5 As atoms as in Figure 2.2 (a) will be considered. The coordinates of the atoms are shown in Table 2.1 where k, l and c are distances between atoms and are obtained from the material's structure. In Figure 2.2 (b) the nearest-neighbor (NN) Fe-Fe distance is $l = 2.854$ $\mathring{A}$, [Singh and Du (2008)] the distance between Fe and As atoms is $s = 2.327$ $\mathring{A}$ [Singh and Du (2008)]. The next nearest-neighbor (NNN) Fe-Fe distance $d = \sqrt{2}l = 4.037$ $\mathring{A}$, see Figure 2.2 (c). Finally the distance of the As atoms from the Fe plane is $c = \sqrt{s^2 - r^2}$ $= \sqrt{s^2 - l^2/2} = 1.158$ $\mathring{A}$. The director cosines l, m and n for each of the Fe atoms with respect to the center As atom located at (0,0,-c) are given in Table 2.2.

To calculate the orbital overlaps according to the lattice and orbital geometries, the procedure developed by Slater-Koster [Slater and Koster (1954)] will be followed. In Table 2.2 the relevant expressions corresponding to the overlap between d_{xz} and d_{yz} orbitals in the Fe with the p_x, p_y, p_z orbitals in the As according to the geometry of the Fe-As plans are given. These orbital overlap integrals will yield the hopping amplitudes used in the tight-binding Hamiltonian.

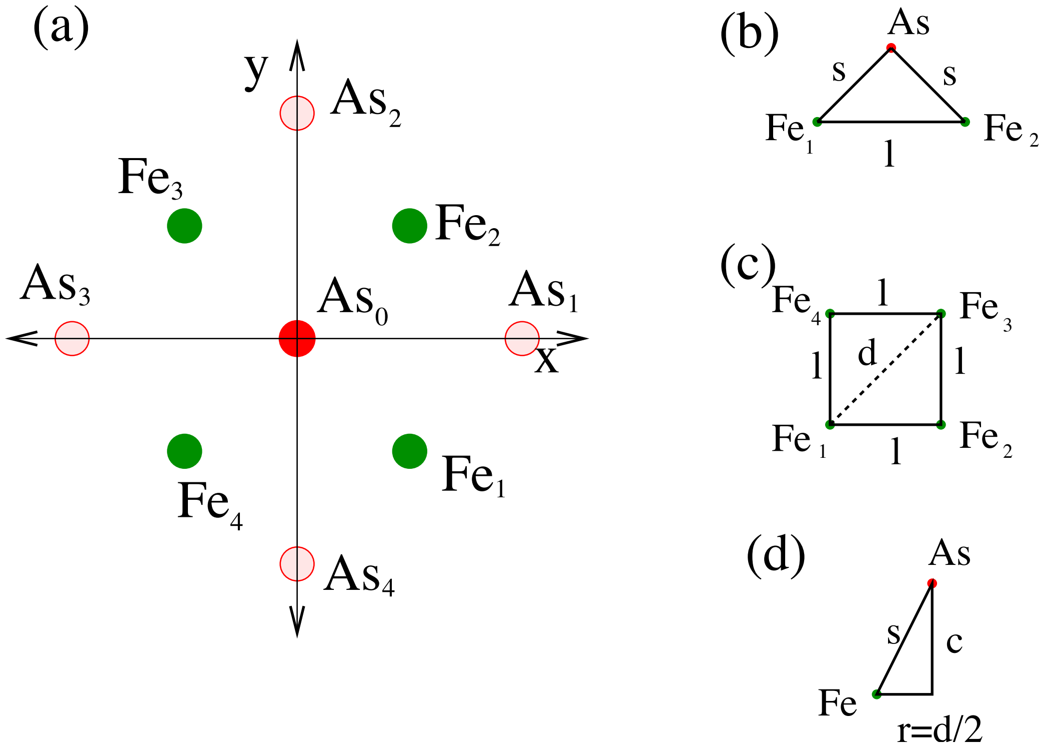

Figure 2.2: (a) The Fe-As cluster used in our calculations of the hoppings. Green circles are the Fe atoms. The red circle at the center is an As atom at a distance c below the plane, while the shaded red circles are the As atoms that are a distance c above the plane. (b) Distances s and l for NN Fe-Fe atoms. (c) The distance d along the diagonal of the Fe-Fe plaquettes. (d) The distance c for As atoms [Moreo et al. (2009b)].

Table 2.2: Director cosines of the Fe atoms with respect to As_0 (see Fig. 2.2 (a)).

Ion	l	m	n
Fe_1	k/s	-k/s	c/s
Fe_2	k/s	k/s	c/s
Fe_3	-k/s	k/s	c/s
Fe_4	-k/s	-k/s	c/s

2.2.1 Overlap Integrals between Fe d_{xz} and d_{yz} orbitals and As p_x and p_y orbitals

Using the energy integrals from Table 2.3 with the director cosines from Table 2.2 the hopping amplitudes can be determined:

$$|t_{x,yz}| = |t_{y,xz}| = a = \sqrt{3}\frac{k^2 c}{s^3}(pd\sigma) - 2\frac{k^2 c}{s^3}(pd\pi) \tag{2.1}$$

$$|t_{x,yz}| = |t_{y,xz}| = b = \sqrt{3}\frac{k^2 c}{s^3}(pd\sigma) + \frac{c}{s}(1 - 2\frac{k^2}{s^2})(pd\pi) \tag{2.2}$$

where $pd\sigma$ ($pd\pi$) are nearest neighbor overlap integrals for σ (π) bonds. After inputing the values of k, s and c (given above) the magnitude of these hopping parameters are:

$$a = 0.324(pd\sigma) - 0.374(pd\pi) \tag{2.3}$$

$$b = 0.324(pd\sigma) + 0.123(pd\pi) \tag{2.4}$$

Figure 2.3 shows the sign of the hopping amplitudes between Fe and As atoms. Next effective Fe-Fe hopping amplitudes will be calculated for both nearest and next nearest neighbor Fe atoms. First consider nearest neighbor d_{xz} orbitals. In the $\hat{y}$ direction, consider two possible paths between the d_{xz} orbitals in the Fe atoms and the As p_y orbitals : (1) $d_{xz}\mathrm{Fe}_1 - p_y\mathrm{As}_0 - d_{xz}\mathrm{Fe}_2$ and $d_{xz}\mathrm{Fe}_1 - p_y\mathrm{As}_1 - d_{xz}\mathrm{Fe}_2$. As seen in Figure 2.3 (a) each path contributes $-a^2$. Now in the $\hat{x}$ direction consider two more paths between d_{xz} and p_x orbitals: (3) $d_{xz}\mathrm{Fe}_1 - p_x\mathrm{As}_0 - d_{xz}\mathrm{Fe}_2$ and (4) $d_{xz}\mathrm{Fe}_1 - p_x\mathrm{As}_1 - d_{xz}\mathrm{Fe}_2$. Figure 2.3 (b) shows that each path contributes b^2. Putting all of this together, up to second order in perturbation theory [Fulde (1991)], the

Table 2.3: Slater-Koster energy integrals written in terms of director cosines and the orbital overlaps ($pd\sigma$, $pd\pi$, $dd\sigma$, $dd\pi$). Non-existing integrals can be found by cyclical permutation of the coordinates and the director cosines [Slater and Koster (1954)].

Orbitals	Energy Integral
x/xz	$\sqrt{3}l^2n(pd\sigma) + n(1-2l^2)(pd\pi)$
x/yz	$\sqrt{3}lmn(pd\sigma) - 2lmn(d\pi)$
y/xz	$\sqrt{3}lmn(pd\sigma) - 2lmn(pd\pi)$
y/yz	$\sqrt{3}m^2n(pd\sigma) + n(1-2m^2)(pd\pi)$
z/xz	$\sqrt{3}n^2l(pd\sigma) + l(1-2n^2)(pd\pi)$
z/yz	$\sqrt{3}n^2m(pd\sigma) + m(1-2n^2)(pd\pi)$
xz/xz	$3l^2n^2(dd\sigma) + (1^2 + n^2 - 4l^2n^2)(dd\pi)$ $+ln(m^2 + l^2n^2)(dd\delta)$
yz/yz	$3lm^2n^2(dd\sigma) + (m^2 + n^2 - 4m^2n^2)(dd\pi)$ $+(l^2 + m^2n^2)(dd\delta)$
xz/yz	$3lmn^2(dd\sigma) + lm(1-4n^2)[(dd\pi) - (dd\delta)]$

effective nearest neighbor hopping amplitude between Fe d_{xz}-d_{xz} orbital via p_x, p_y orbitals is :

$$t^{xz-xz}_{\hat{x},\hat{y}} = (-2a^2 + 2b^2)/\Delta = 2(b^2 - a^2)/\Delta \tag{2.5}$$

where $\Delta = 1.25$ eV [Goldman et al. (2008)] is the difference between the on-site energies of the d and p orbitals. The same procedure described above to can be used to calculate the nearest neighbor Fe d_{yz}-d_{yz} via As p_x, p_y orbitals:

$$t^{yz-yz}_{\hat{x},\hat{y}} = (-2a^2 + 2b^2)/\Delta = 2(b^2 - a^2)/\Delta = t^{xz-xz}_{\hat{x},\hat{y}} \tag{2.6}$$

Notice that nearest neighbor interorbital hoppings between Fe $d_{xz} - d_{yz}$ via As p_x, p_y orbitals is not possible.

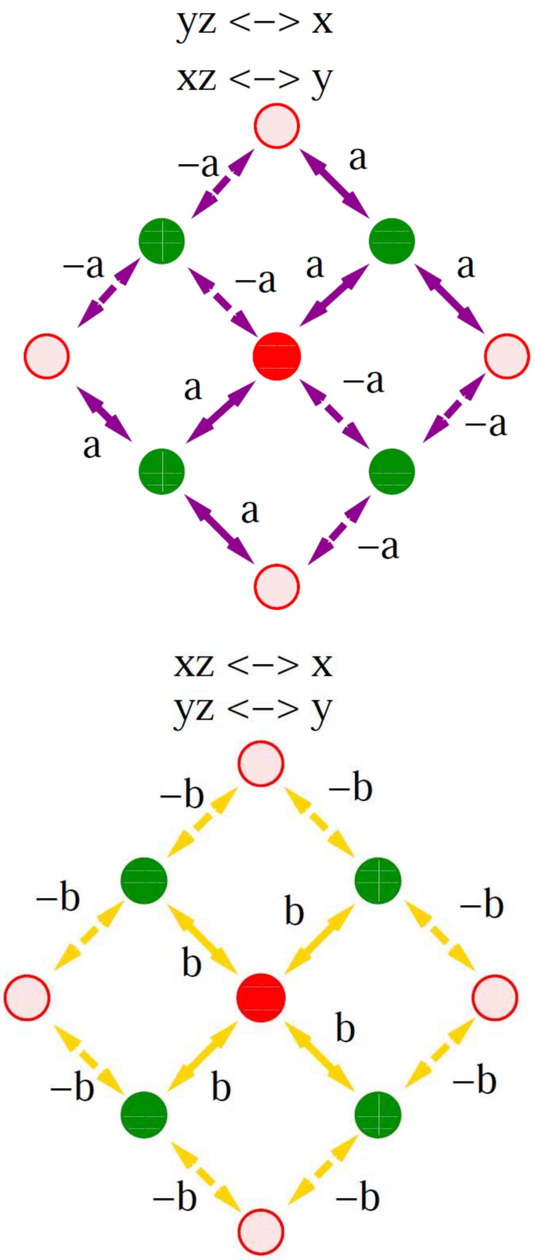

Figure 2.3: (a) Hoppings between $d_{yz}(d_{xz})$ orbitals in Fe and $p_x(p_y)$ orbitals in As for the cluster considered in Figure 2.2 (a). (b) Hoppings between $d_{xz}(d_{yz})$ orbitals in Fe and $p_x(p_y)$ orbitals.

To find the diagonal hopping t_d along the $\hat{x}\pm\hat{y}$ directions, the next nearest neighbor (NNN) hopping, consider paths from Fe_1 to Fe_3 and Fe_2 to Fe_4. In the first case the hopping path is $d_{xz}\mathrm{Fe}_1 - p_x\mathrm{As}_0 - d_{xz}\mathrm{Fe}_3$ which, again referring to Figure 2.3 (b), contributes b^2 to t_d^{xz} while the second path $d_{xz}\mathrm{Fe}_1 - p_y\mathrm{As}_0 - d_{xz}\mathrm{Fe}_3$, referring to Figure 2.3 (a), contributes a^2. It can be shown that the NNN intraorbital hopping between Fe d_{yz} orbitals gives the same result. Thus the form of our diagonal hopping is:

$$t^{xz-xz}_{\hat{x}\pm\hat{y}} = t^{yz-yz}_{\hat{x}\pm\hat{y}} = (a^2+b^2)/\Delta \tag{2.7}$$

In contrast to the NN Fe hoppings, the NNN Fe hoppings does have an interorbital component. In the $\hat{x}+\hat{y}$ direction, from Fe_2 to Fe_4, the contribution to the hopping is $2ab$ while in the $\hat{x}-\hat{y}$ direction, from Fe_1 to Fe_3, the contribution is $-2ab$ [Moreo et al. (2012)]. Thus in different directions the inter-orbital hopping changes signs:

$$t^{xz-yz}_{\hat{x}+\hat{y}} = 2ab/\Delta \tag{2.8}$$

$$t^{xz-yz}_{\hat{x}-\hat{y}} = -2ab/\Delta \tag{2.9}$$

2.2.2 Overlap between Fe d_{xz}, d_{yz} and As p_z

Again using the energy integrals from Table 2.3, a new hopping is obtained:

$$|t_{z,xz}| = |t_{z,yz}| = g = \sqrt{3}\frac{kc^2}{s^3}(pd\sigma) + \frac{k}{s}(1-2\frac{c^2}{s^2})(pd\pi) \tag{2.10}$$

Using the values of k,s, and c calculated above

$$g = 0.263(pd\sigma) + 0.31(pd\pi) \tag{2.11}$$

The signs for these hopping amplitudes can be seen in Figure 2.4 (a) and (b). Following the same procedure as in the last section, it can be shown that

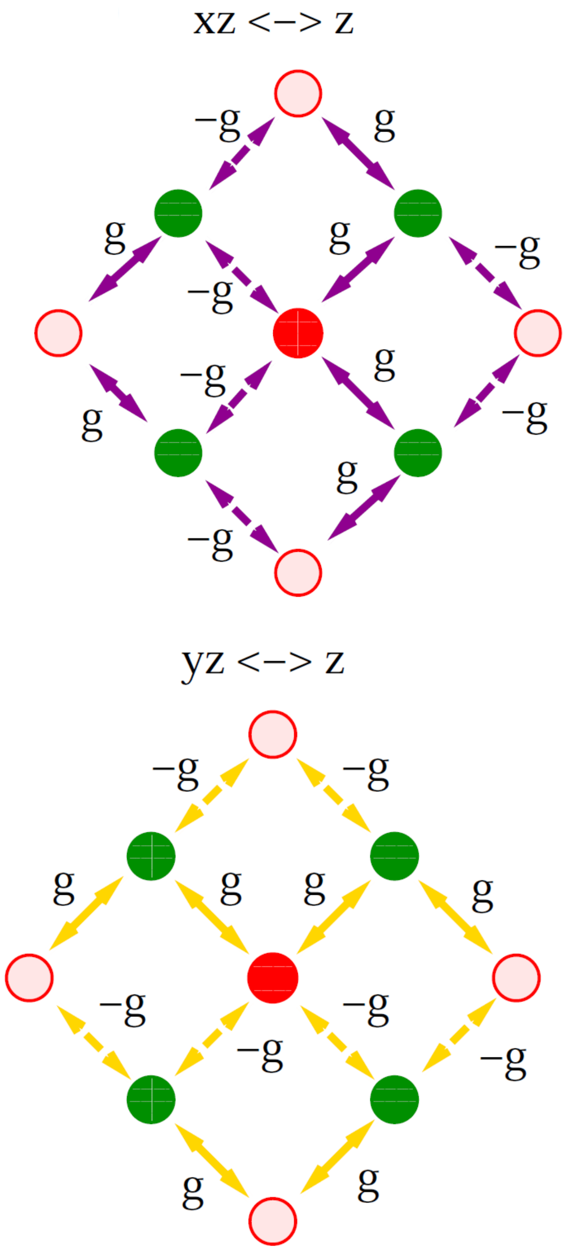

Figure 2.4: (a) Hoppings between d$_{xz}$ orbitals in Fe and p$_z$ orbitals in As for the cluster considered in Figure 2.2 (a). (b) Hoppings between d$_{yz}$ orbitals in Fe and p$_z$ orbitals in As [Moreo et al. (2009b)].

$$t_{\hat{x}}^{xz-xz} = t_{\hat{y}}^{yz-yz} = -2g^2/\Delta' \quad (2.12)$$

$$t_{\hat{y}}^{xz-xz} = t_{\hat{x}}^{yz-yz} = 2g^2/\Delta' \quad (2.13)$$

$$t_{\hat{x}\pm\hat{y}}^{xz-xz} = t_{\hat{x}\pm\hat{y}}^{yz-yz} = -2g^2/\Delta' \quad (2.14)$$

where Δ' is the difference between the Fe d and As p_z orbitals and has a magnitude of $\Delta' = 5$ eV [Goldman et al. (2008)].

Because the Fe-As cluster is invariant under translations in the $\hat{x}$ or $\hat{y}$ directions followed by a reflection on the x-y plane, it is possible to map the original unit cell, containing two As atoms and two Fe atoms (see Figure 2.5 (a)), to a unit cell containing only one Fe atom (see Figure 2.5 (b)). In this transformation, the lattice will be rotated by $\pi/4$ so the x$'$ and y$'$ axes are parallel to the vectors connecting nearest neighbor Fe atoms. One result of this transformation is that the Brillouin zone of the transformed unit cell is increased by a factor of two, Figure 2.5 (e). The transformed square Fe lattice has D_{4h} point group symmetry. Consideration of the symmetry operations in D_{4h} will be useful later on.

2.2.3 Direct Fe-Fe Hopping

Since the Fe-Fe distance, $l = 2.854$ $\mathring{A}$, is of the same order as the Fe-As distance, $s = 2.327$ $\mathring{A}$, not only hopping from Fe-Fe d orbitals via As p orbitals must be considered, but direct Fe-Fe d orbital overlaps will be discussed as well. Using the energy integrals from Table 2.3 ($E_{xz,xz}$, $E_{yz,yz}$, $E_{xz,yz}$) and noting that Fe atoms lie in a square array on the same plane (for NN : n=0, l=±1 with m=0 or l=0 with m=±1) the NN hopping amplitudes are:

$$t_{\hat{x}}^{xz,xz} = t_{\hat{y}}^{yz,yz} = -(dd\pi) \quad (2.15)$$

$$t_{\hat{y}}^{xz,xz} = t_{\hat{x}}^{yz,yz} = (dd\delta) \quad (2.16)$$

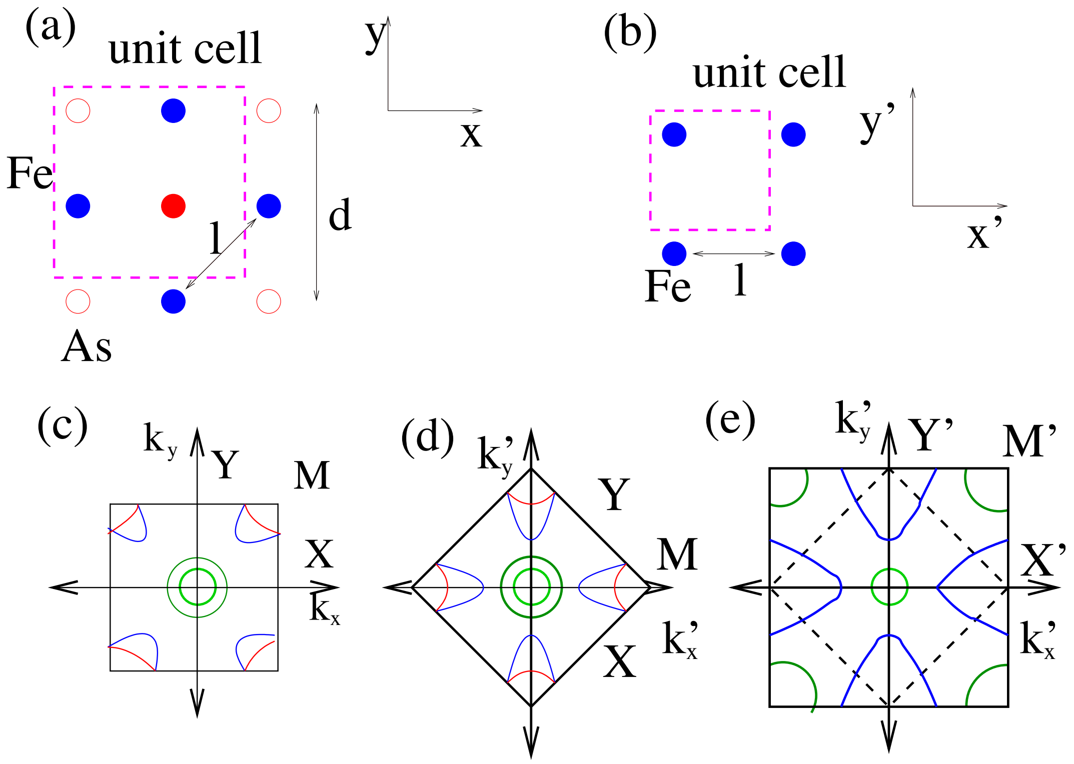

Figure 2.5: (a) Schematic representation of the Fe-As plane. Blue circles are the Fe atoms. The red filled circle is an As atom at a distance c below the plane, while the red open circles are As atoms at a distance c above the plane. (b) Unit cell for the effective Fe-only square lattice. The Fe-Fe lattice has been rotated by 45°. (c) Schematic first Brillouin Zone (FBZ) for the Fe-As plane. The point X is at $(2\pi/d, 0)$, with $d = \sqrt{2}l$. (d) FBZ for the Fe-As lattice after a 45° rotation. (e) FBZ for the rotated Fe-Fe shown in (b). $X' = (2\pi/l, 0)$ and it is equivalent to the M point for the Fe-As plane in (c). The electron and hole Fermi surfaces obtained by band-structure calculations are schematically indicated. Panels c-e will be useful for the discussion related to the nodal structure of the superconducting state in Section 2.4 [Moreo et al. (2009b)].

For NNN Fe-Fe hoppings :

$$t^{xz,xz}_{\hat{x}\pm\hat{y}} = t^{yz,yz}_{\hat{x}\pm\hat{y}} = -(dd\pi' + dd\delta')/2 \tag{2.17}$$

$$t^{xz,yz}_{\hat{x}+\hat{y}} = -(dd\pi' - dd\delta')/2 \tag{2.18}$$

$$t^{xz,yz}_{\hat{x}-\hat{y}} = (dd\pi' - dd\delta')/2 \tag{2.19}$$

where $dd\pi'$, $dd\delta'$ denote NNN overlap integrals.

2.2.4 Two Orbital Tight-Binding Hamiltonian

Collecting the terms calculated in the previous section, the kinetic energy part of the effective Hamiltonian consisting of only Fe d_{xz} and d_{yz} orbitals is given by:

$$\begin{aligned}
H^{xz,yz}_{TB} &= -t_1 \sum_{\mathbf{i},\sigma} (d^\dagger_{\mathbf{i},x,\sigma} d_{\mathbf{i}+\hat{y},x,\sigma} + d^\dagger_{\mathbf{i},y,\sigma} d_{\mathbf{i}+\hat{x},y,\sigma} + h.c.) \\
&- t_2 \sum_{\mathbf{i},\sigma} (d^\dagger_{\mathbf{i},x,\sigma} d_{\mathbf{i}+\hat{x},x,\sigma} + d^\dagger_{\mathbf{i},y,\sigma} d_{\mathbf{i}+\hat{y},y,\sigma} + h.c.) \\
&- t_3 \sum_{\mathbf{i},\hat{\mu},\hat{\nu},\sigma} (d^\dagger_{\mathbf{i},x,\sigma} d_{\mathbf{i}+\hat{\mu}+\hat{\nu},x,\sigma} + d^\dagger_{\mathbf{i},y,\sigma} d_{\mathbf{i}+\hat{\mu}+\hat{\nu},y,\sigma} + h.c.) \\
&+ t_4 \sum_{\mathbf{i},\sigma} (d^\dagger_{\mathbf{i},x,\sigma} d_{\mathbf{i}+\hat{x}+\hat{y},y,\sigma} + d^\dagger_{\mathbf{i},y,\sigma} d_{\mathbf{i}+\hat{x}+\hat{y},x,\sigma} + h.c.) \\
&- t_4 \sum_{\mathbf{i},\sigma} (d^\dagger_{\mathbf{i},x,\sigma} d_{\mathbf{i}+\hat{x}-\hat{y},y,\sigma} + d^\dagger_{\mathbf{i},y,\sigma} d_{\mathbf{i}+\hat{x}-\hat{y},x,\sigma} + h.c.) \\
&- \mu \sum_{\mathbf{i}} (n^x_{\mathbf{i}} + n^y_{\mathbf{i}})
\end{aligned} \tag{2.20}$$

where $d^\dagger_{\mathbf{i},\alpha,\sigma}$ creates an electron with z-axis spin projection σ in orbital α at the site i of the Fe lattice. The chemical potential is denoted by μ and $n^\alpha_{\mathbf{i}} = \sum_\sigma d^\dagger_{\mathbf{i},\alpha,\sigma} d_{\mathbf{i},\alpha,\sigma}$ is the number operator and $\hat{\mu} = \hat{x}$ or $\hat{y}$. The hopping parameters in terms of the hopping amplitudes found previously are:

$$\begin{aligned}
t_1 &= -2[(b^2-a^2)/\Delta + g^2/\Delta'] - dd\delta \\
t_2 &= -2[(b^2-a^2)/\Delta - g^2/\Delta'] - dd\pi \\
t_3 &= -[(a^2+b^2)/\Delta + g^2/\Delta'] - (dd\pi' + dd\delta')/2 \\
t_4 &= -(2ab/\Delta - g^2/\Delta') - (dd\pi' - dd\delta')/2
\end{aligned} \tag{2.21}$$

While the overlap integrals can be estimated using tabulated values on the orbital overlaps and distances between the atoms in the pnictides, the focus in this section will be on hopping parameters fitted to band-structure calculations (see Figure 2.6 (a),(b)) [Raghu et al. (2008)].

The tight-binding Hamiltonian in Eqn. (2.20) can be represented in momentum space via the Fourier transform

$$d^{\dagger}_{\mathbf{k},\alpha,\sigma} = \frac{1}{\sqrt{N}} \sum_{\mathbf{j}} e^{-i\mathbf{k}\cdot\mathbf{j}} d^{\dagger}_{\mathbf{j},\alpha,\sigma} \tag{2.22}$$

where $\mathbf{k}$=(k_x, k_y) with $k_x = \frac{2\pi n_x}{N}$ for n_x=0,...,.$N-1$ is the wave vector and N is the number of sites on the lattice.

$$\begin{aligned}
H^{xz,yz}_{TB} = &\sum_{k_x,k_y,\sigma} (-2t_1 cosk_y - 2t_2 cosk_x - 4t_3 cosk_x cosk_y) d^{\dagger}_{\mathbf{k},xz,\sigma} d_{\mathbf{k},xz,\sigma} \\
&+ \sum_{k_x,k_y,\sigma} (-2t_1 cosk_x - 2t_2 cosk_y - 4t_3 cosk_x cosk_y) d^{\dagger}_{\mathbf{k},yz,\sigma} d_{\mathbf{k},yz,\sigma} \\
&+ \sum_{k_x,k_y,\sigma} (-4t_4 sink_x sink_y) d^{\dagger}_{\mathbf{k},xz,\sigma} d_{\mathbf{k},yz,\sigma} - \mu \sum_{\mathbf{k},\hat{\mu}} (n^x_{\mathbf{k}} + n^y_{\mathbf{k}}),
\end{aligned} \tag{2.23}$$

where, for the fitted parameters t$_i$ of [Raghu et al. (2008)], μ = 1.54 eV for the undoped case (with each orbital half filled). The band structure/Fermi surface are shown in Figure 2.6 in the extended Brillouin zone. In the reduced Brillouin zone, the hole pockets depicted at $\mathbf{k}$=(π, π) are folded to make a second hole pocket at

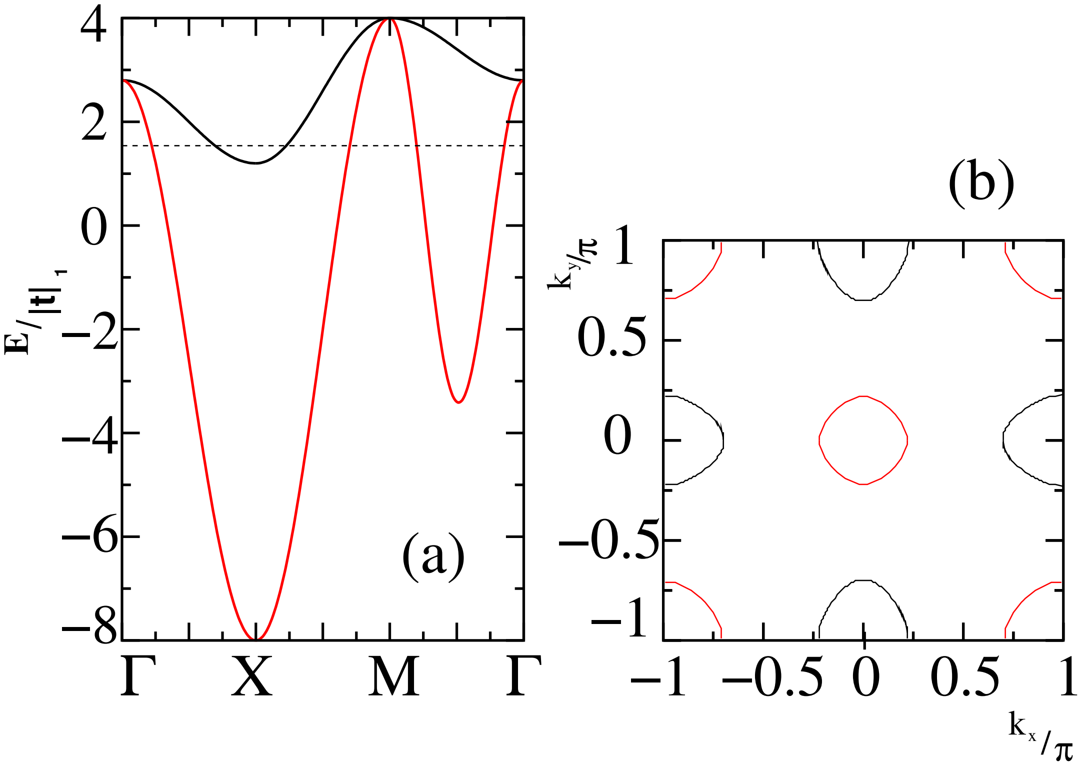

Figure 2.6: :
$t_1 = -1.0$, $t_2 = 1.3$,$t_3 = t_4 = -0.85$ (all in eV units).](a) Energy vs. momentum for the non-interacting tight-binding Hamiltonian Eqn. (20) using hopping amplitudes obtained from fits of band-structure calculations [Raghu et al. (2008)]: $t_1 = -1.0$, $t_2 = 1.3$,$t_3 = t_4 = -0.85$ (all in eV units). Results are plotted along the path (0,0)-(π,0)-(π,π)-(0,0). (b) Fermi surface for the half-filled system [Moreo et al. (2009b)].

k=(0,0). Furthermore, while energy bands are composed of hybridized Fe-d orbitals in most parts of the BZ, along directions of high symmetry, $\Gamma \rightarrow X$ ($\Gamma \rightarrow Y$) the energy bands are made of pure orbitals, see Figure 2.7.

2.3 Interactions

In order to create the full two-orbital model for the pnictides, Coulomb interactions must be added to the tight-binding Hamiltonian. These Coulomb terms are, introduced in section 1.2 but put in terms of the Fe d_{xz} and d_{yz} orbitals is::

$$H_{\text{int}} = U \sum_{\mathbf{i},\alpha} n_{\mathbf{i},\alpha,\uparrow} n_{\mathbf{i},\alpha,\downarrow} + (U' - J/2) \sum_{\mathbf{i}} n_{\mathbf{i},x} n_{\mathbf{i},y}$$

$$- 2J \sum_{\mathbf{i}} \mathbf{S}_{\mathbf{i},x} \cdot \mathbf{S}_{\mathbf{i},y} + J \sum_{\mathbf{i}} (d^{\dagger}_{\mathbf{i},x,\uparrow} d^{\dagger}_{\mathbf{i},x,\downarrow} d_{\mathbf{i},y,\downarrow} d_{\mathbf{i},y,\uparrow} + h.c.), \tag{2.24}$$

where $\alpha = xz, yz$ denotes the orbital, the spin density in orbital α at site $\mathbf{i}$ is denoted by $S_{\mathbf{i},\alpha}$, $n_{\mathbf{i},\alpha}$ is the electronic density in orbital α at site $\mathbf{i}$. The first (second) term represents on-site intraorbital (interorbital) repulsion between electrons. The third term is the Hund's rule spin coupling that favors the ferromagnetic alignment of spins in different orbitals at the same lattice site. Finally, the last indicates "pair-hopping" and its coupling is equal to J by symmetry.

2.4 Exact Diagonalization Results

As discussed in Section 1.3, models of strongly correlated electrons only have analytical solutions in a few special cases. For this reason, numerical numerical methods are an important tool in the study of these systems. The advantage of considering only two of the Fe-*d* orbitals is that the number of degrees of freedom in the system is such that a Lanczos algorithm, introduced in 1.3, on a tilted $\sqrt{8} \times \sqrt{8}$ lattice (seen in Figure 2.8) can be used (which is not the case when three or more

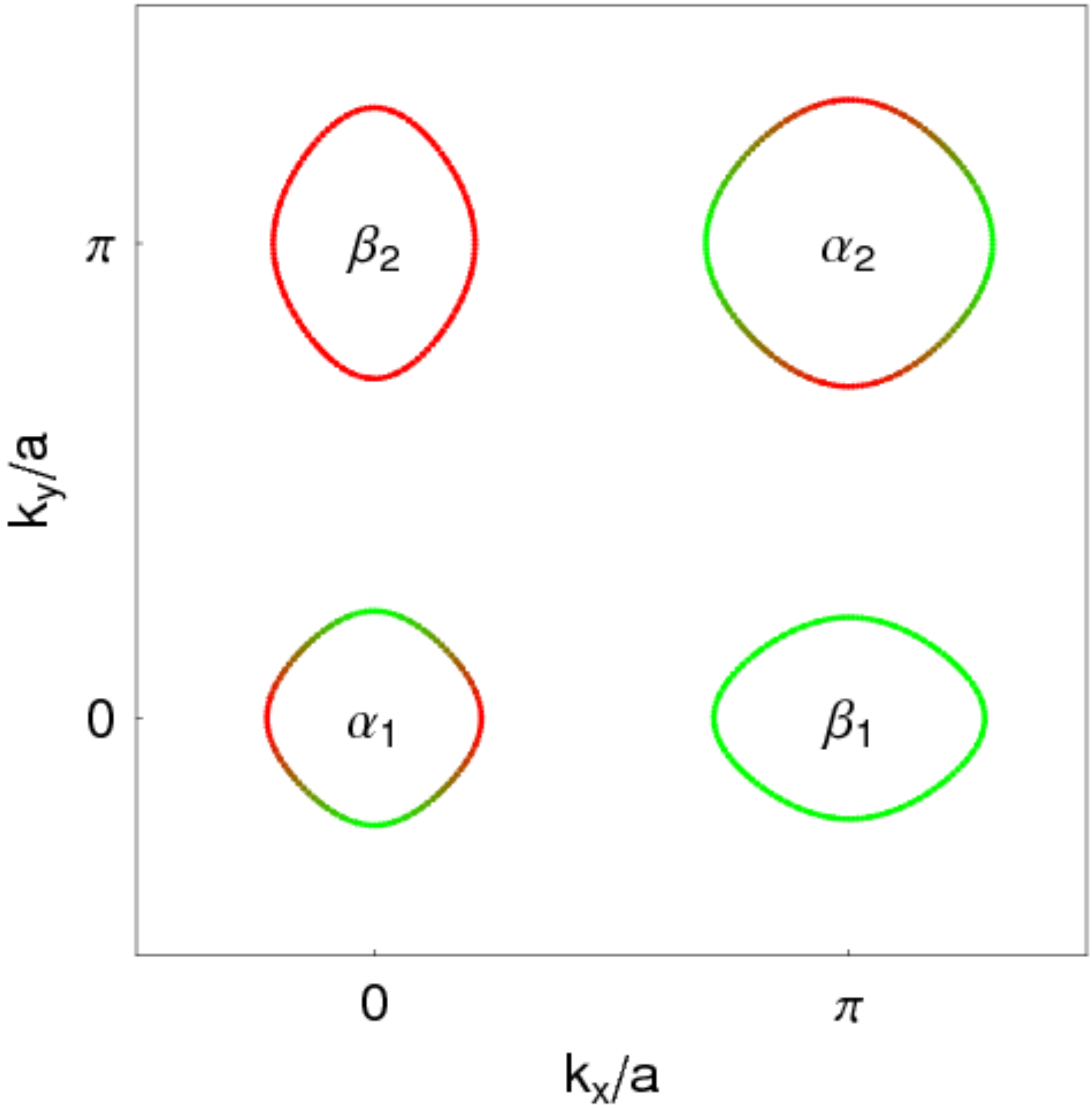

Figure 2.7: Orbital contribution to the energy bands at the Fermi energy are denoted by red (d_{xz}) and green (d_{yz}). For the basis used in this model, the Γ-X/Y directions are highly symmetric. In these directions the energy bands are composed of only one orbital in both the electron and hole pockets [Graser et al. (2009)].

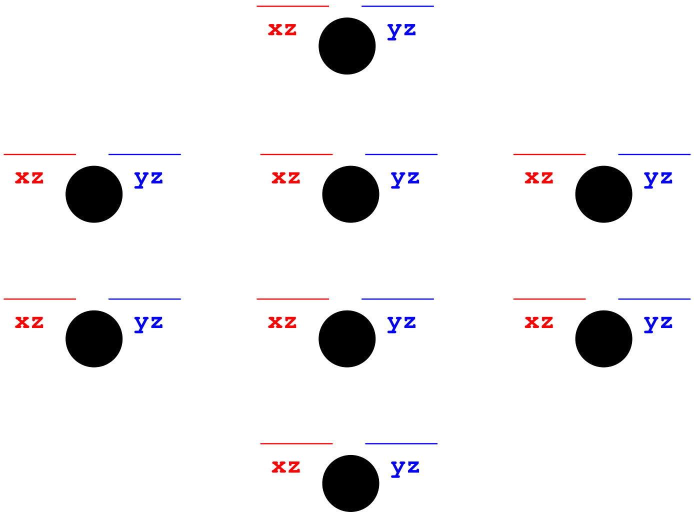

Figure 2.8: The tilted $\sqrt{8} \times \sqrt{8}$ cluster used in exact diagonalization calculations. Black circles represent Fe atoms, red (blue) lines represent d_{xz} (d_{yz}) orbitals.

orbitals are taken into account) [Dagotto (1994); Daghofer et al. (2008); Moreo et al. (2009b)]. On this lattice, magnetic and superconducting pairing properties are studied and presented below.

At half-filling colinear or $(0,\pi)/(\pi,0)$ antiferromagnetic order arises and is enhanced by increasing on-site repulsion U at fixed J, or increasing J at fixed U see (Figure 2.9). Increasing J leads to larger localized moments allowing for a stronger overall collective spin ordering. This magnetic order is found experimentally, see Ref [de la Cruz et al. (2008)]. As seen in Figure 2.10, after doping, the antiferromagnetic order decreases, following the trend in the phase diagrams presented in Figure 1.2.

In Figure 2.11, the ground state symmetries for states with two extra electrons above half filling are listed for different values of U v. J/U. The symmetries are found by comparing the symmetry of the half filled ground state with the symmetry of the ground state with two extra electrons. As can be seen from the figure, U promotes singlet states and at very large values of U a negative binding energy is found. Since the half filled state has 16 electrons in the 8-site lattice with orbitals, binding energy

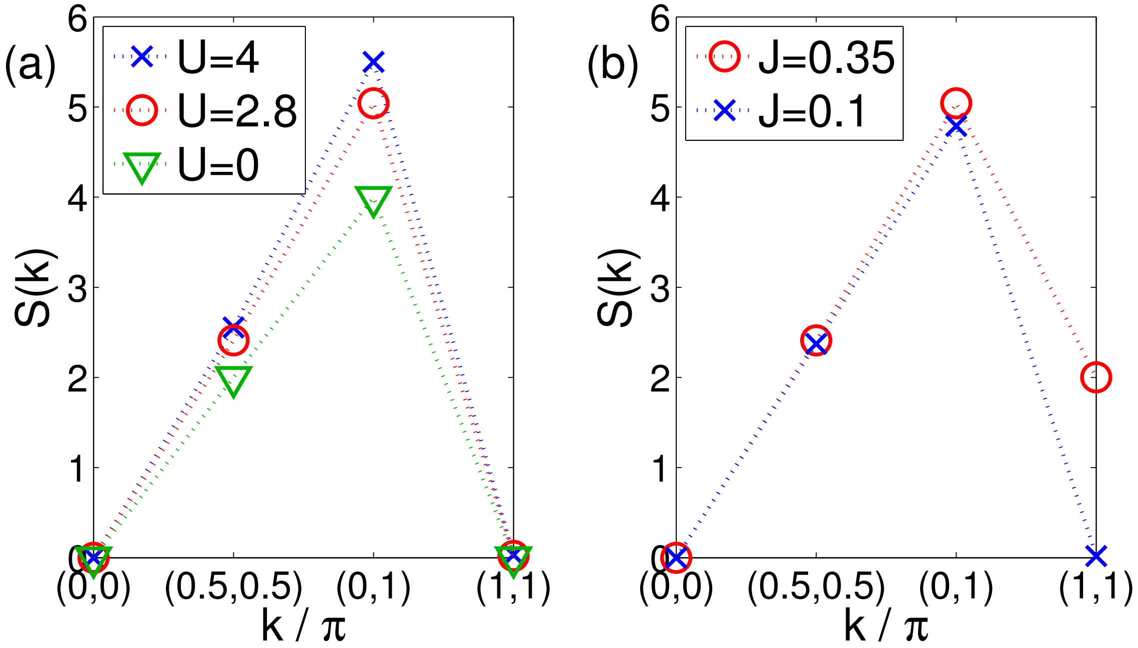

Figure 2.9: Spin structure factor S(**k**) for (a) results for several values of U and J/U=1/8; (b) results for two values of J, with U=2.8 eV fixed [Moreo et al. (2009b)].

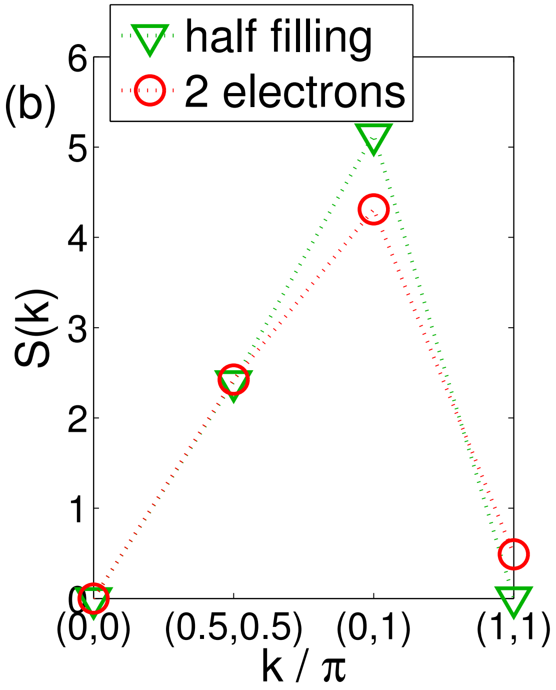

Figure 2.10: Spin structure factor S(**k**) for half filling and half filling plus two electrons for U=2.8 and J=0.1 (in eV units) [Moreo et al. (2009b)].

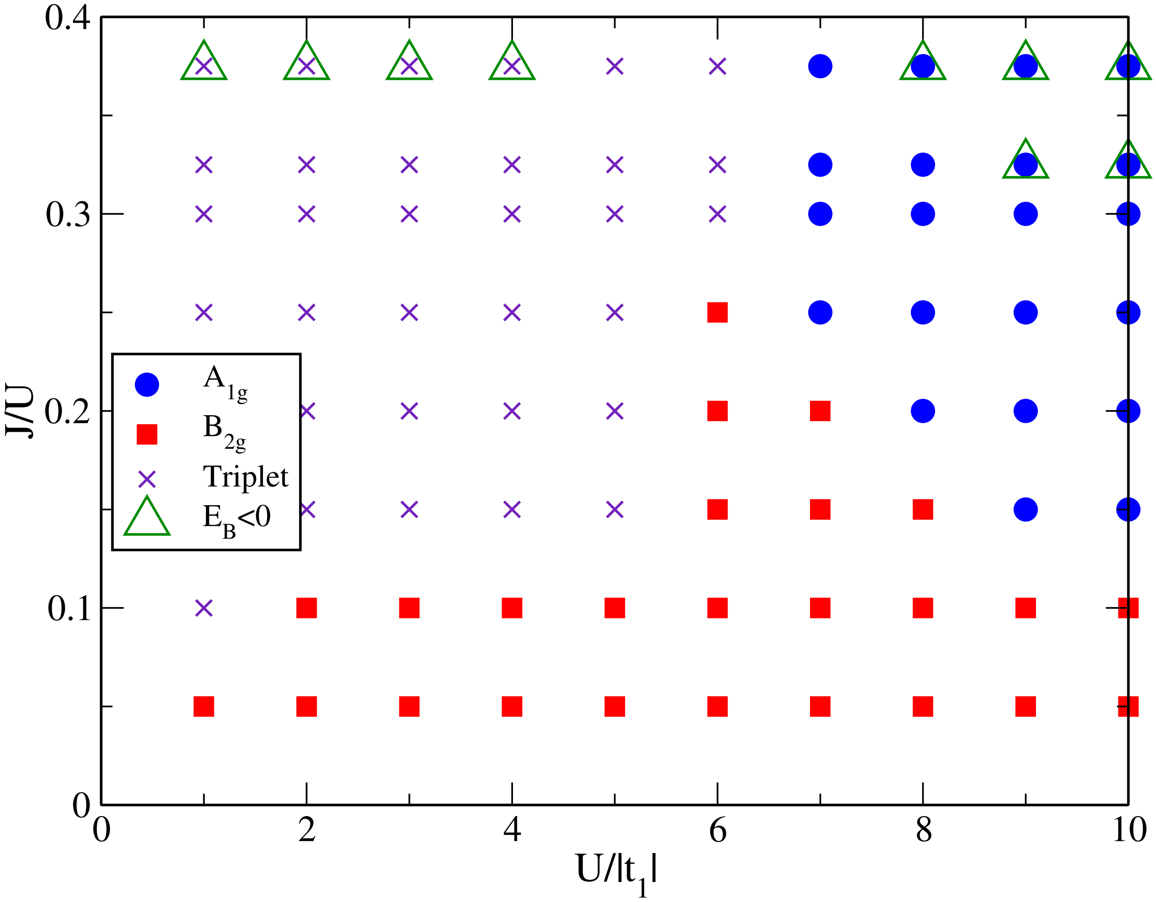

Figure 2.11: Dominant pairing tendencies of the ground state for two more electrons than half-filling. Red squares indicate B_{2g}, blue circles A_{1g} and purple Xs show triplet pairing symmetry. The green triangles show the regions where binding energy is less than zero.

is defined as

$$E_B = (E(18) - E(16)) - 2(E(17) - E(16)), \tag{2.25}$$

with $E(N)$ being the ground state for N particles.

To find pairing operators that are allowed by lattice and orbital symmetries in the two orbital model, the two orbital tight-binding Hamiltonian given in Eqn. (2.25) will be rewritten in terms of the Pauli matrices τ_i, along with the identity matrix τ_0 [Wan and Wang (2009)]. Doing this H_{TB} becomes :

$$H_{TB}(\mathbf{k}) = \sum_{\mathbf{k},\sigma} \Psi^{\dagger}_{\mathbf{k},\sigma} \xi_k \Psi_{\mathbf{k},\sigma} \tag{2.26}$$

where $\Psi^{\dagger}_{\mathbf{k},\sigma} = [d^{\dagger}_{xz}(\mathbf{k}), d^{\dagger}_{yz}(\mathbf{k})]$ and

$$\xi_k = \alpha_k \tau_0 + \beta_k \tau_1 + \epsilon_k \tau_3 \tag{2.27}$$

with

$$\begin{aligned} \alpha_k &= 2(t_1 + t_2)(cosk_x + cosk_y) - 4t_3 cosk_y cosk_x \\ \beta_k &= -4t_4 sink_x sink_y \\ \epsilon_k &= 2(t_1 - t_2)(cosk_x - cosk_y) && (2.28) \\ & && (2.29) \end{aligned}$$

As mentioned before, the Fe lattice has D_{4h} point group symmetry, thus every element in the equations above transform according to one of the irreducible representations of this group.

Since the Hamiltonian must transform according to A_{1g} (the Hamiltonian is invariant under the symmetry operations of the group), the Pauli matrices in the orbital basis chosen here transform as indicated in Table 2.4. In multi-orbital systems the general form of a spin-singlet pairing operator is given by [Moreo et al. (2009b)]

$$\Delta^\dagger(\mathbf{k}) = f(\mathbf{k})(\sigma_i)_{\alpha,\beta}(d^\dagger_{\mathbf{k},\alpha,\uparrow}d^\dagger_{-\mathbf{k},\beta,\downarrow} - d^\dagger_{\mathbf{k},\beta,\uparrow}d^\dagger_{-\mathbf{k},\alpha,\downarrow}) \tag{2.30}$$

where a sum over repeated indices is implied; the operators $d^\dagger_{\mathbf{k},\alpha,\sigma}$ have been defined in the previous sections, $f(\mathbf{k})$ is the form factor that transforms according to one of the irreducible representations of the crystal's symmetry group, and σ_i is a spin matrix defined in orbital space. Although $f(\mathbf{k})$ may, in general, have a very complicated form, a short pair-coherence length requires the two electrons that form the pair to be very close to each other. Consequently, this work will focus on nearest and diagonal next-nearest neighbors, and form factors that are allowed in a lattice with D_{4h} symmetry. The momentum-dependent expression, as well as the irreducible representation according to which each form factor transforms, are given in Table 2.6. In multi-orbital systems the symmetry of the superconducting pairing operator (OP) depends not only on the symmetry of the spacial form factor but on the symmetry of the orbital component as well [Moreo et al. (2009a)]. This means that while a given form factor may transform as A_{1g}, if combined with an orbital matrix with B_{2g} symmetry, the entire OP will transform according to B_{2g} symmetry. The product table in Table 2.5 shows the total symmetry of the product of all possible pairs of the irreducible representations of the D_{4h} point group. Table 2.7 gives the total symmetry of all form factors combined with the orbital matrices.

In addition to comparing the symmetry of the half filled ground state with the ground state with two extra electrons, overlaps ($\langle\Psi_{N+2}|\Delta^\dagger|\Psi_N\rangle$) with the pairing operators listed above acting on the half filled ground state ($\Delta^\dagger|\Psi_N\rangle$) with the state with two more electrons were explored ($\langle\Psi_{N+2}|$). From this analysis, two dominant spin-singlet pairing operators were found. The first, is favored for low to intermediate values of U. The interaction binds pairs in NN sites in different orbitals and has B_{2g} symmetry. The second is found to be favored at large values of U. It pairs electrons in NN sites in the same orbital and has A_{1g} symmetry. Also there is a region in parameter

Table 2.4: Symmetry properties of the terms/matrices in the tight-binding Hamiltonian.

Term/Matrix	IR
α_k	A_{1g}
β_k	B_{2g}
ϵ_k	B_{1g}
τ_0	A_{1g}
τ_1	B_{2g}
τ_3	B_{1g}

Table 2.5: D_{4h} multiplication table.

IR	A_{1g}	A_{2g}	B_{1g}	B_{2g}	E_g
A_{1g}	A_{1g}	A_{2g}	B_{1g}	B_{2g}	E_g
A_{2g}	A_{2g}	A_{1g}	B_{2g}	B_{1g}	E_g
B_{1g}	B_{1g}	B_{2g}	A_{1g}	A_{2g}	E_g
B_{2g}	B_{2g}	B_{1g}	A_{2g}	A_{1g}	E_g
E_g	E_g	E_g	E_g	E_g	A_{1g}+A_{2g}+ B_{1g}+ B_{2g}

space where the pairing operator is a triplet. Since a variety of experimental data suggest that the Cooper pairs are spin singlets [Grafe et al. (2008); Matano et al. (2008); Kawabata et al. (2008)], the triplet region will not be discussed.

See Figure 2.11 for the locations of these symmetries. From this analysis the form of the B_{2g} pairing operator can be obtained:

$$\Delta^{\dagger}_{B_{2g}} = \frac{1}{2N_{sites}} \sum_{\mathbf{i},\alpha,\mu} (d^{\dagger}_{\mathbf{i},-\alpha,\uparrow} d^{\dagger}_{\mathbf{i}+\hat{\mu},\alpha,\downarrow} - d^{\dagger}_{\mathbf{i},\alpha,\downarrow} d^{\dagger}_{\mathbf{i}+\hat{\mu},-\alpha,\uparrow}) \tag{2.31}$$

where $\mathbf{i}$=1,...,N_{sites} denotes the lattice site, $\hat{\mu} = \hat{x}, \hat{y}$ is the unit vector connecting NN sites, and $\alpha = xz, yz$ indicates the d_{xz} and d_{yz} orbitals, respectively.

The A_{1g} pairing operator is given by:

$$\Delta^{\dagger}_{A_{1g}} = \frac{1}{2N_{sites}} \sum_{\mathbf{i},\alpha,\mu} (d^{\dagger}_{\mathbf{i},\alpha,\uparrow} d^{\dagger}_{\mathbf{i}+\hat{\mu},\alpha,\downarrow} - d^{\dagger}_{\mathbf{i},\alpha,\downarrow} d^{\dagger}_{\mathbf{i}+\hat{\mu},\alpha,\uparrow}) \tag{2.32}$$

The Fourier transformed form factors of both of these operators can be found in Table 2.7 as 2 (5) for the A_{1g} (B_{2g}) pairing operator. The numerical results of the

Table 2.6: Form factors f($\mathbf{k}$) for pairs up to distance (1,1) classified according to their symmetry under D_{4h} operations.

Distance	f($\mathbf{k}$)	IR
NN	$\cos k_x + \cos k_y$	A_{1g}
NN	$\cos k_x - \cos k_y$	B_{1g}
NNN	$\cos k_x \cos k_y$	A_{1g}
NNN	$\sin k_x \sin k_y$	B_{2g}

Table 2.7: Pairing operators up to distance (1,1) allowed by lattice and orbital symmetries.

No.	Distance	IR	f($\mathbf{k}$)σ_i
1	NN	B_{2g}	$(\cos k_x + \cos k_y)\tau_1$
2	NN	A_{1g}	$(\cos k_x + \cos k_y)\tau_0$
3	NN	A_{2g}	$(\cos k_x - \cos k_y)\tau_1$
4	NN	B_{1g}	$(\cos k_x - \cos k_y)\tau_0$
5	NN	B_{1g}	$(\cos k_x + \cos k_y)\tau_3$
6	NN	A_{1g}	$(\cos k_x - \cos k_y)\tau_3$
7	NNN	A_{1g}	$(\cos k_x \cos k_y)\tau_0$
8	NNN	B_{2g}	$(\sin k_x \sin k_y)\tau_0$
9	NNN	B_{2g}	$(\cos k_x \cos k_y)\tau_1$
10	NNN	A_{1g}	$(\sin k_x \sin k_y)\tau_1$
11	NNN	B_{1g}	$(\cos k_x \cos k_y)\tau_3$
12	NNN	A_{2g}	$(\sin k_x \sin k_y)\tau_3$

two orbital model reproduce the magnetic order observed experimentally and capture the A_{1g} pairing state that is argued in several theoretical approaches [Mazin et al. (2008); Kuroki et al. (2008)] but a nodal B_{2g} state also appears which should be considered to interpret experiments where evidence of nodes is found [Shan et al. (2008); Gang et al. (2008); Ahilan et al. (2008); Nakai et al. (2008); Grafe et al. (2008); Wang et al. (2009b); Matano et al. (2008); Mukuda et al. (2008); Millo et al. (2008); Wang et al. (2009a); Dong et al. (2010)].

2.5 Conclusions

A minimal model, consisting of the Fe d_{xz} and d_{yz} orbitals, capable of reproducing the basic physics of the pnictides was developed using the Slater-Koster approach. This model was investigated via exact diagonalization on a tilted $\sqrt{8} \times \sqrt{8}$ cluster. The magnetic properties of the undoped parent compound found in neutron scattering experiments are reproduced. Also, upon electron doping the magnetic order is suppressed. Spin-singlet pairing states that respect orbital and lattice symmetry were formulated. Pairing states transforming according to the A_{1g} and B_{2g} irreducible representations of the D_{4h} point group were found to be favored in exact diagonalization calculations.

Chapter 3

Two Orbital t-U-J Model

3.1 Introduction

The goal of this Chapter is to study the most favorable pairing channels of a two-orbital Hubbard model using small-cluster exact diagonalization techniques (namely, the Lanczos algorithm) for electron and hole doping, and to contrast the results of the two cases since the model is not particle-hole symmetric [Nicholson et al. (2011a, 2012); Daghofer et al. (2008); Moreo et al. (2009b)]. To reduce the severe constraints imposed by the small size of the clusters that can be diagonalized in present day computers, a modification to the Hubbard model for the pnictides will be here applied. For this purpose, Heisenberg "J" terms will be added to the original Hubbard model to enhance spin order and pairing tendencies, but without projecting out doubly occupied sites and charge fluctuations. These terms help to establish tightly bound-states upon doping that can be studied with Lanczos methods on the small clusters currently accessible with state-of-the-art computers.

The organization of this chapter is as follows: the model and the method are reviewed in Section 3.2, the main results for electron and hole doping are presented in Sections 3.3 and 3.4.

3.2 Model and Method

The model studied here is based on the well-known and widely used two-orbital Hubbard model introduced in Section 2.2.4 [Daghofer et al. (2008); Moreo et al. (2009b); Raghu et al. (2008)] that employs the d_{xz} (x) and d_{yz} (y) Fe orbitals. These orbitals provide the largest contribution to the pnictides' band structure at the FS, see Fig. 2.1 of Section 2.1. The reduction in the actual number of active orbitals in the pnictides is necessary in order to perform Lanczos studies. Calculations with more orbitals for the same cluster size studied here are simply not possible at present.

The parameters of the electronic hopping terms of the model were previously chosen to provide a close agreement with the band structure calculations obtained with density-functional theory [Raghu et al. (2008)]. In addition to the hopping terms, the model also includes the on-site Coulomb interaction consisting of intra- and inter-orbital Coulomb repulsions with couplings U and U', the Hund's rule coupling J_{H}, and the pair-hopping term with strength J' in Eqn. 2.24.

Naively, it may seem that selecting a stronger on-site Hubbard interaction would stabilize a stronger antiferromagnetic state. However, this procedure also induces an insulator, and actually the strength of the effective coupling between the Fe-spins decreases as $1/U$ with increasing U. To avoid this problem, in early studies of the one-band t-U-J model [Daul et al. (2000)] Heisenberg terms have been added and shown to enhance pairing tendencies. Since our aim is to investigate the symmetries of the Cooper pairs, the additional magnetic interactions must have the same symmetries as the original Hamiltonian. To make sure that the symmetries are properly handled, the additional Heisenberg interaction is given by the operatorial form that corresponds to the super-exchange terms derived from the strong-coupling (large-U) limit. In the case of the one-band Hubbard model, this is a Heisenberg term with spin $S = 1/2$. In the case of a multi-orbital model away from half-filling, the corresponding super-exchange contains an orbital degree of freedom in addition to the spin and it is of a Kugel-Khomskii type [Kugel and Khomskii (1982); Krüger et al. (2009)].

In the present case of a half-filled two-orbital model, the low-energy Hilbert space for the strong-coupling limit, with both U and $J_{\rm H}$ large, is given by doubly occupied sites with singly occupied orbitals. Due to the Hund's coupling, the two electrons per site form a triplet state, with an energy $E_0 = U' - J_{\rm H} = U - 3J_{\rm H}$, compared to $E_1 = U' + J_{\rm H} = U - J' = E_0 + 2J_{\rm H}$ and $E_2 = U + J_{\rm H} = E_0 + 4J_{\rm H}$ for inter- and intra-orbital singlet states. The low-energy Hilbert space is, thus, given by a spin $S = 1$ at each site. The interaction between these spins can be obtained by second-order perturbation theory in an analogous manner as the well-known derivation of the Heisenberg model from the one-orbital Hubbard model. The calculation for the two orbitals is the most easily carried out when the hopping term preserves orbital flavor, because the first hopping process, which creates a virtual excitation with energy $U + J_{\rm H}$, then has to involve the same orbital as the second, which goes back to the low-energy Hilbert subspace. By this procedure it can be shown that the result is the isotropic Heisenberg interaction for $S = 1$ with a coupling

$$J_{\rm eff} = \frac{2}{3}\frac{t_a^2 + t_b^2}{U + J_{\rm H}} \,, \tag{3.1}$$

where t_a and t_b are the hopping parameters corresponding to the two orbitals. With the notation $t_{a/b} = t_{1/2}$ [Raghu et al. (2008)], the nearest-neighbor (NN) coupling $J_{\rm NN}$ can be derived. For a next-nearest–neighbor (NNN) coupling, which is natural since in the original Hubbard model the hoppings involve both NN and NNN Fe atoms, it is convenient to transform to a rotated orbital basis $(|xz\rangle \pm |yz\rangle)/\sqrt{2}$, where the hoppings are diagonal in orbital space and given by $t_3 \pm t_4$, leading to

$$J_{\rm NNN} = \frac{4}{3}\frac{t_3^2 + t_4^2}{U + J_{\rm H}} = 2\frac{t_3^2 + t_4^2}{t_1^2 + t_2^2} J_{\rm NN} \,. \tag{3.2}$$

To avoid the proliferation of parameters, the ratio $J_{\rm NNN}/J_{\rm NN}$ is kept fixed to 0.93, which is the value that results from the two orbital model's hoppings $t_1 = -1$, $t_2 = 1.3$, $t_3 = t_4 = -0.85$ as can be seen in Section 2.2.4 [Raghu et al. (2008)].

The extended two-orbital Hubbard Hamiltonian is exactly investigated using the Lanczos algorithm [Dagotto (1994); Parlett (1980)] on a tilted $\sqrt{8} \times \sqrt{8}$ cluster, as done in the previous Chapter (see Section 2.4) [Dagotto (1994); Daghofer et al. (2008); Moreo et al. (2009b)]. In spite of the small size of the cluster, this still requires substantial computational resources. More specifically, even exploiting the Hamiltonian symmetries the calculation of the undoped-limit ground state of the eight-sites cluster still requires a basis with $\sim$ 2-20 M states (slightly more demanding than a 16-site cluster one-band Hubbard model), depending on the subspace explored. Runs applying the Lanczos technique had to be performed for all the allowed momenta $\mathbf{k}$ of the cluster, and for all the quantum numbers under rotations and reflections (i.e. all the irreducible representations A_{1g}, A_{2g}, B_{1g}, B_{2g}, and E_g of the D_{4h} symmetry group [Moreo et al. (2009b)]), and also for all the z-axis total spin projections. In addition, the computation of binding energies for the case of hole doping requires calculations for a number of electrons N equal to 14, 15, and 16, varying U, J_{H}, and J_{NN} using a fine grid. For these reasons, the overall effort amounted to $\sim 8,000$ diagonalizations of the cluster, supplemented also by calculations of dynamical properties, using a Penguin 128GB Altus 3600 computer.

3.3 Electron Doped

3.3.1 Binding stabilization

As discussed in the Introduction, here the spin background with wavevectors $(\pi, 0)$-$(0, \pi)$ will be magnified via the addition of extra Heisenberg terms with the expectation that carrier attraction will become stronger, leading to $E_{\text{B}} < 0$ pairing. As can be seen in Fig. 3.1(a), the desired goal is reached since increasing J_{NN} eventually leads to E_{B} becoming negative for all the studied (U, J_{H}) couplings. The spin-triplet region virtually disappears (Fig. 3.2(b)) and it is mainly replaced by the $B_{2\text{g}}$ state which itself becomes confined to $U < 4\ |t_1|$ (squares) due to the expansion of the $A_{1\mathrm{g}}$ region. The symmetries shown in Fig. 3.2(b) were obtained with the smallest super-exchange values $(J_{\mathrm{NN}}, J_{\mathrm{NNN}})$ that produce binding of two electrons at each (U, J_{H}) point. In Fig. 3.1(a), where the binding energy *vs.* J_{NN}/U is shown at several U's and at a fixed (realistic) J_{H}/U=0.2. Increasing J_{NN} eventually induces binding for all U's. The value of J_{NN}/U for which binding occurs decreases as U increases.

Figure 3.3 shows the spin structure for half filling calculated along the dot-dashed (red) line of of Figure 3.1. The magnetic order with wavevectors (0, π)-(π, 0) clearly dominates at all couplings investigated, ranging from a region without binding, to B_{2g} binding, and ending in A_{1g} binding. Moreover, as expected, increasing the magnitude of J_{NN}/U enhances the strength of the (0, π)-(π, 0) peak. In the figure, the ratio $\mathrm{J}_{NN}/\mathrm{J}_{NNN}$ is fixed to 0.93.

Studying E_{B} and the relative symmetry between the N=16 and 18 GS's, phase diagrams in the $(U, J_{\mathrm{NN}}/U)$ plane were constructed. In Fig. 3.1(b), typical results for J_{H}/U=0.2 are shown. The bound state has $A_{1\mathrm{g}}$ symmetry in most of the binding region, but a $B_{2\mathrm{g}}$ symmetric state also prevails at small U values ($\sim 2\ |t_1|$). Both symmetries appear inside the proper magnetic/metallic region of the undoped limit, according to mean-field calculations [Yu et al. (2009); Luo et al. (2010)] extended to incorporate J_{NN}. While the results in Figs. 3.1(a,b) keep a fix ratio of $\mathrm{J}_{NN}/\mathrm{J}_{NNN} =$ 0.93, varying $J_{\mathrm{NN}}/J_{\mathrm{NNN}}$ in the range [0.5,1.5] gives qualitatively the same behavior, as can be seen in Fig. 3.4. The only interesting change observed by this procedure is that in- creasing (decreasing) $\mathrm{J}_{NN}/\mathrm{J}_{NNN}$ favors more the pairing B_{2g} (A1g).

3.3.2 Overlaps

Consider now the pairing operators that produce the electronic bound states. The overlap

$$\langle\Psi(N=18)|\Delta^{\dagger}_{\mathbf{k},i}|\Psi(N=16)\rangle \tag{3.3}$$

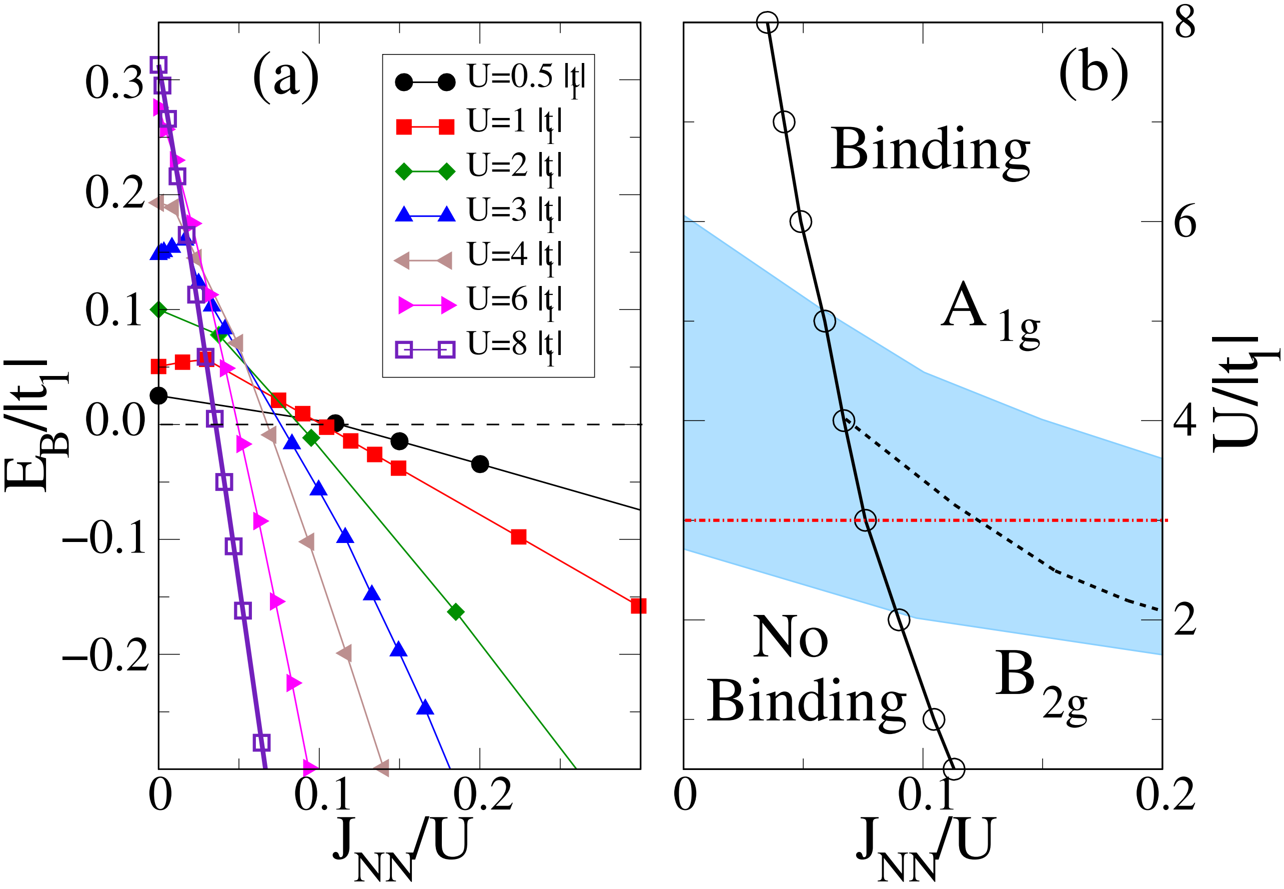

Figure 3.1: (a) $E_{\mathrm{B}}/|t_1|$ *vs.* J_{NN}/U for different values of $U/|t_1|$ and J_{H}/U=0.2. (b) Phase diagram showing "Binding" and "No Binding" regions and the symmetry of the two-electron bound state varying $U/|t_1|$ and J_{NN}/U, for J_{H}/U=0.2. The shaded area is where the antiferromagnetic/metallic state is stabilized in the mean-field approximation for the undoped limit. The dot-dashed line is for Fig. 3.5 [Nicholson et al. (2011a)].

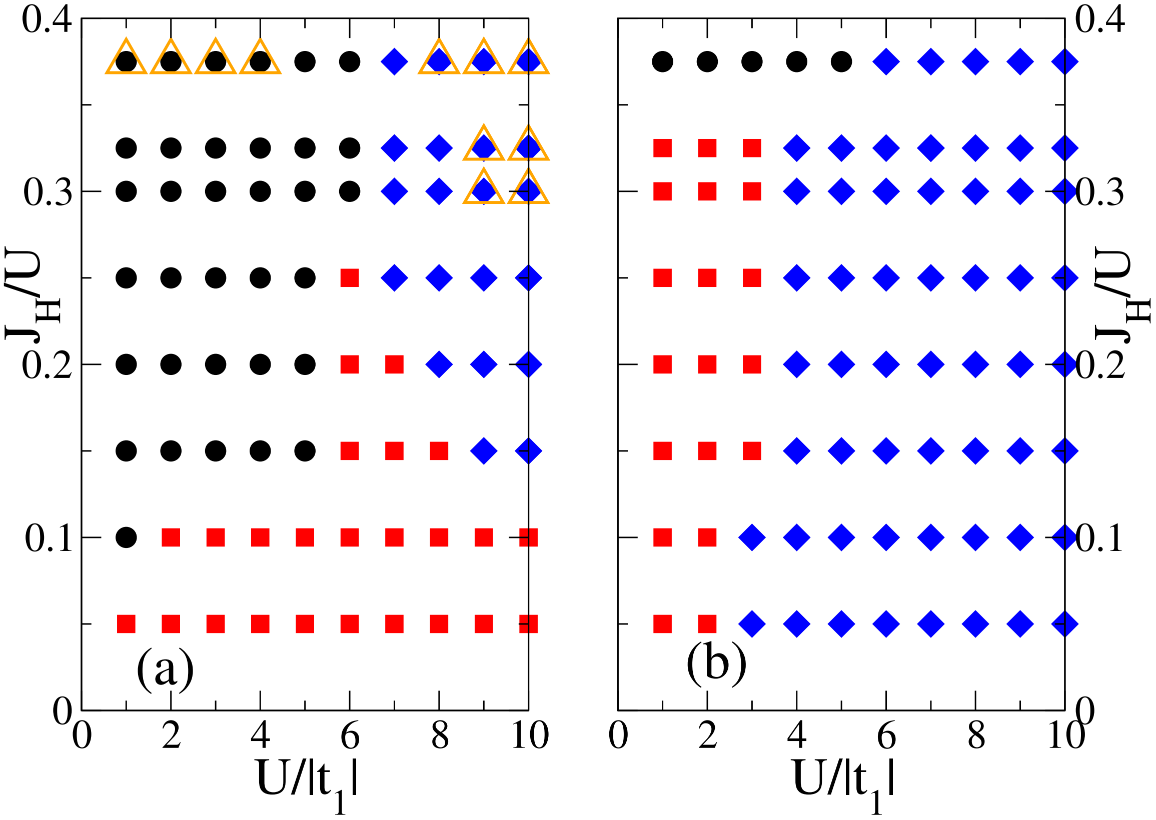

Figure 3.2: Relative symmetry between the N=16 (undoped) and N=18 GS's, varying U and J_{H}/U. Circles denote triplet states, squares $B_{2\mathrm{g}}$-symmetric singlets, and diamonds $A_{1\mathrm{g}}$-symmetric singlets. (a) Results for couplings J_{NN}=$J_{\mathrm{NNN}} = 0$. Open triangles indicate binding. (b) Results for the lowest value of $(J_{\mathrm{NN}}, J_{\mathrm{NNN}})$ where binding appears [Nicholson et al. (2011a)].

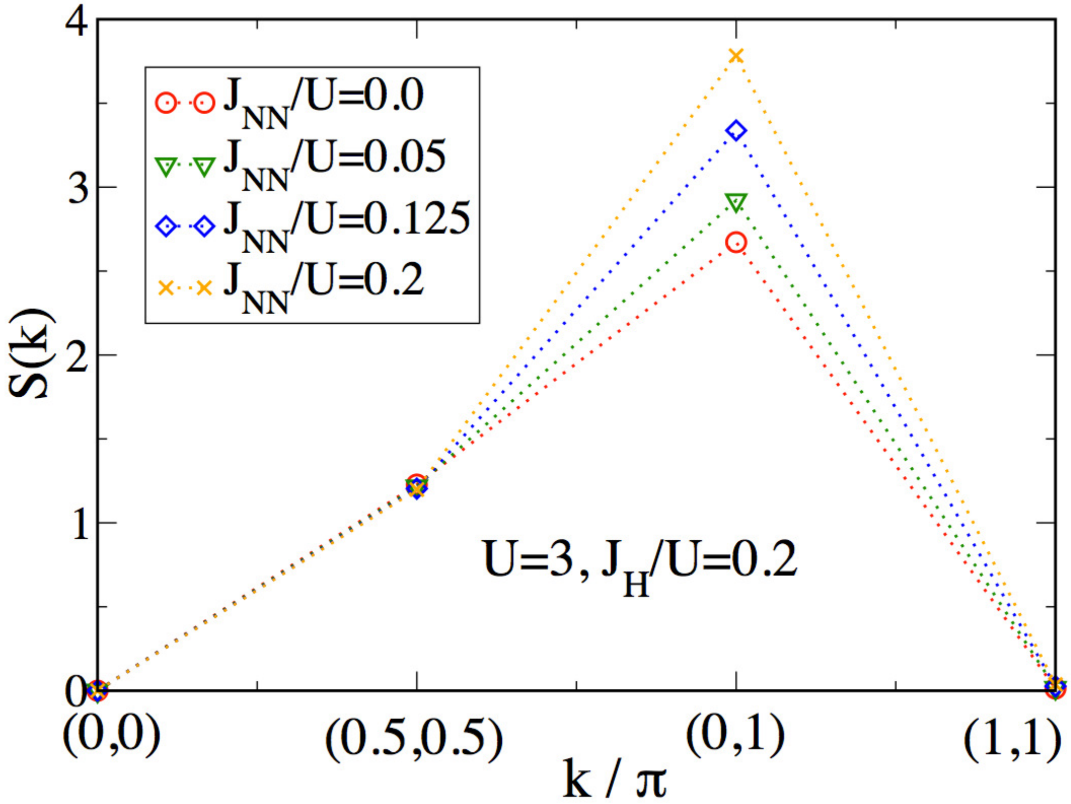

Figure 3.3: Spin structure factor S(k) evaluated using the Lanczos method on an 8-site cluster, at the values of U and J$_H$/U indicated, parametric with J$_{NN}$/U as shown in the inset, and with the ratio J$_{NN}$/J$_{NNN}$ fixed to 0.93. The addition of the superexchange terms clearly enhances the (0, π) (degenerate with (π, 0)) magnetic order. The number of electrons used is 16 [Nicholson et al. (2011a)].

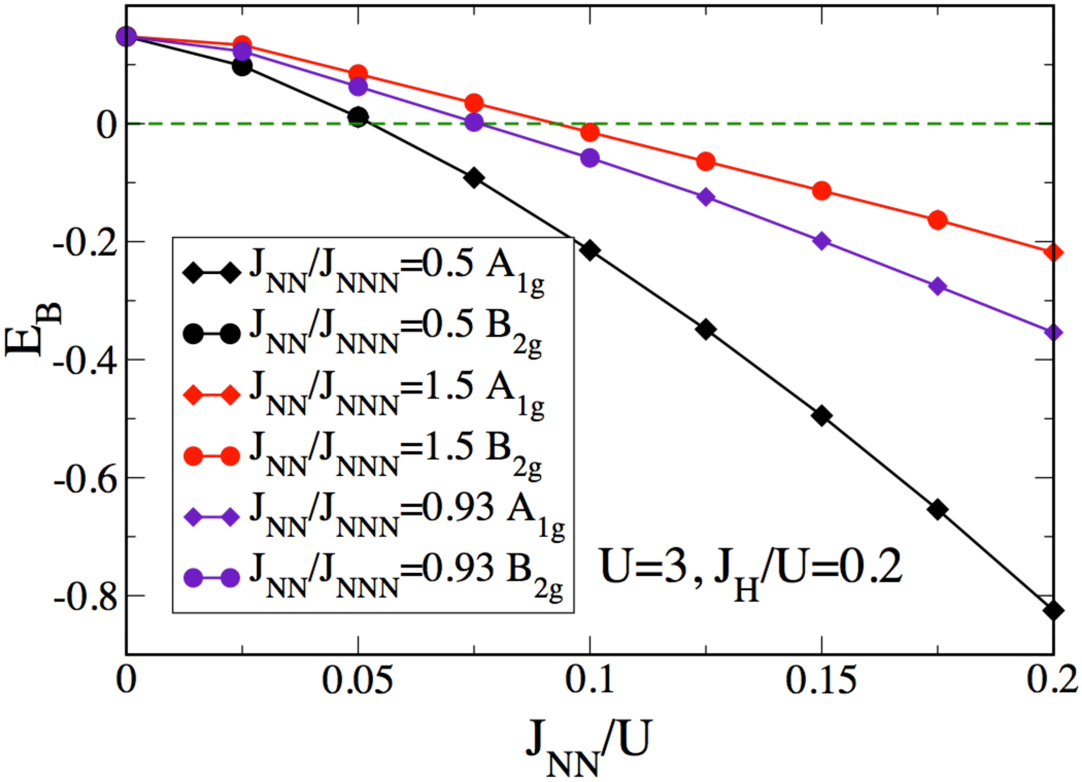

Figure 3.4: Binding energy E_B vs. J_{NN}/U, along the dot-dashed (red) line of Fig. 3.1, parametric with J_{NN} /J_{NNN} . A negative (positive) E_B indicates the formation (the absence) of electronic pairs. The results suggest that there is no qualitative change in varying J_{NN}/J_{NNN} in the range from 0.5 to 1.5. The only quantitative modification is that A_{1g} is more favored decreasing J_{NN} /J_{NNN} , while increasing this ratio favors more the B_{2g} symmetry [Nicholson et al. (2011a)].

was calculated, where $|\Psi(N)\rangle$ is the GS in the subspace of N electrons and

$$\Delta^{\dagger}_{\mathbf{k},i} = \sum_{\alpha\beta} f(\mathbf{k})(\sigma_i)_{\alpha\beta} d^{\dagger}_{\mathbf{k},\alpha,\uparrow} d^{\dagger}_{\mathbf{k},\beta,\downarrow}, \tag{3.4}$$

with $d^{\dagger}_{\mathbf{k},\alpha,\sigma}$ creating an electron with spin z-axis projection σ, at orbital $\alpha = x, y$, and with momentum $\mathbf{k}$. The structure factor $f(\mathbf{k})$ arises from the spatial location of the electrons forming the pair [Moreo et al. (2009b)], and σ_i are the Pauli matrices ($i = 1, 2, 3$) or the 2×2 identity matrix σ_0 ($i = 0$) (note that σ_1 and σ_2 imply an interorbital pairing). Overlaps for all the symmetries in [Moreo et al. (2009b)], and with NN and NNN locations for the electronic pairs, were evaluated.

For all operators respecting the relative symmetry between the doped and undoped states, finite overlaps were found, although of different values. As a trend, as the binding grows, pairing involving NNN operators prevail over the NN ones. For example, in the A_{1g} region in Fig. 3.1(b) there are four pairing operators with finite overlap (shown in Fig. 3.5(a) for U=3$|t_1|$ and J_{H}/U=0.2) characterized by $f(\mathbf{k})\sigma_i$ equal to: (i) $(\cos k_x + \cos k_y)\sigma_0$ (full circles); (ii) $(\cos k_x \cos k_y)\sigma_0$ (full squares); (iii) $(\sin k_x \sin k_y)\sigma_1$ (full diamonds); and (iv) $(\cos k_x - \cos k_y)\sigma_3$ (full triangles). Close to the boundary with the B_{2g} phase where the binding is weak ($E_{\mathrm{B}}\approx$-0.05 $|t_1|$), operators (i) and (ii) present the largest, and almost equal, overlaps. With increasing binding the (i) overlap decreases while (ii) becomes stronger. The overlaps for operators (iii) and (iv) are clearly smaller.

Note that (ii) is the simplest expression of a nodeless $s\pm$ pairing operator [Mazin et al. (2008); Kuroki et al. (2008)]. Our results indicate that this type of pairing dominates *only* when the binding energy is large, which occurs at very large U or J_{NN}. At intermediate values of couplings, a *symmetric* linear combination of (i) and (ii) with almost equal weights is optimal, and it leads to a "quasi-nodal" $s\pm$ pairing state (Fig. 3.5(b)). From this perspective, the most "natural" A_{1g} pairing operator arises from a linear combination of (i) and (ii), as opposed to just (ii) as in $s\pm$ scenarios. The gaps in Fig. 3.5(b) were calculated from mean-field approximations as

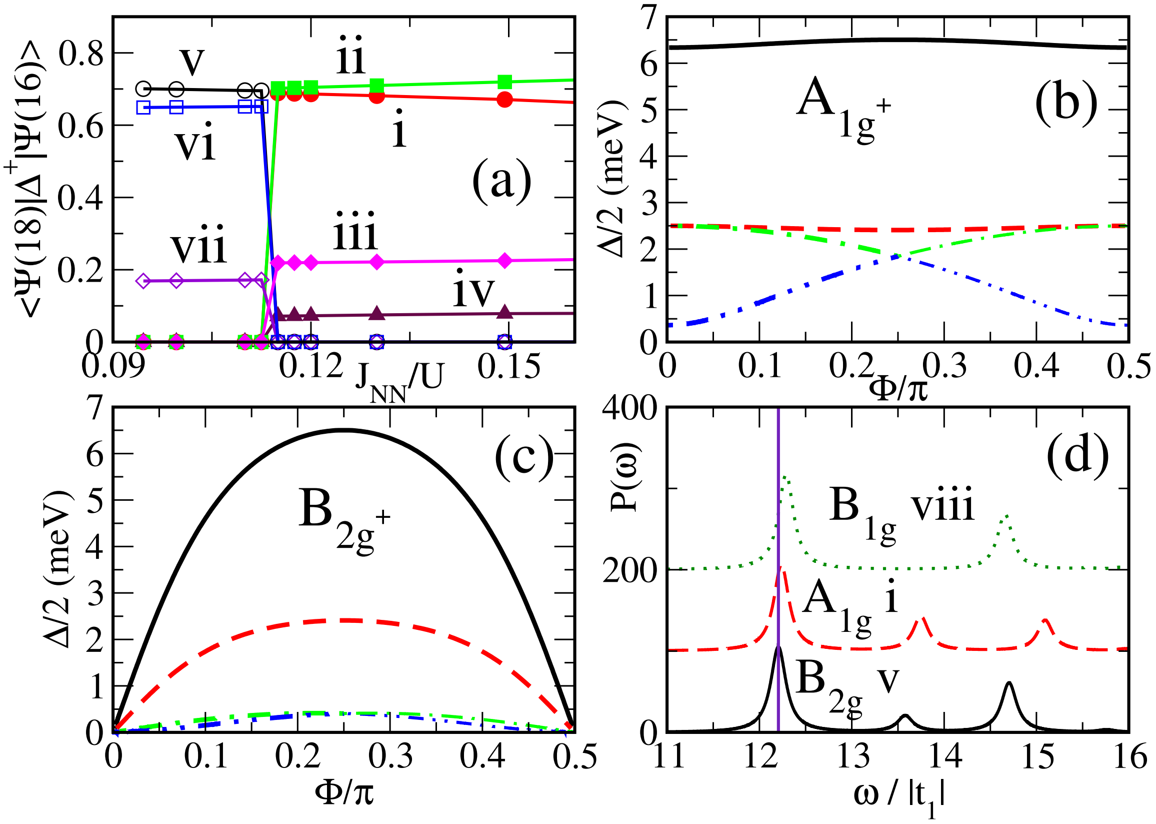

Figure 3.5: (a) Overlap $\langle\Psi(N{=}18)|\Delta^{\dagger}_{\mathbf{k},i}|\Psi(N{=}16)\rangle$ *vs.* $J_{\rm NN}/U$ for the indicated pairing operators, at $U{=}3\ |t_1|$ and $J_{\rm H}/U{=}0.2$. (b) Superconducting gap at the FS: internal hole pocket (continuous line), external hole pocket (dashed line). The dot-dashed and double dot-dashed lines are for the two electron pockets which intersect at the Brillouin zone boundary ($\Phi{=}\pi/4$) of the folded zone. The $A_{\rm 1g^+}$ symmetric linear combination of $A_{\rm 1g}$ operators (i) and (ii) is used, with equal weight. The angle Φ is measured from the positive x-axis to the positive y-axis. (c) Same as (b) but for the $B_{\rm 2g^+}$ symmetric combination of the $B_{\rm 2g}$ operators (v) and (vi). (d) Dynamic pairing susceptibility for the pairing operators indicated (see text), at $U{=}3\ |t_1|$, $J_{\rm H}/U{=}0.2$, and $J_{\rm NN}/U{=}0.095$. The vertical line indicates $E(18){-}E(16)$ [Nicholson et al. (2011a)].

in [Moreo et al. (2009b)] and [Daghofer et al. (2010)], and choosing a pairing strength V_0 such that the gap order-of-magnitude in meV's agrees with experiments. Note that the linear combination $A_{\rm 1g^+}$ for the hole pockets closely reproduces (full and dashed lines) the ARPES results in the superconducting state, with both gaps only weakly $\mathbf{k}$-dependent, and with the interior (exterior) pocket gap ~ 12 (6) meV. The electron pockets, on the other hand, present strongly $\mathbf{k}$-dependent gaps, and a quasi-node is found along the x- (y-) axes for the pocket at X (Y). In the folded zone, this implies that the quasi node is on the outer pocket, in agreement with angle-resolved specific heat measurements [Zeng et al. (2010)].

Note that the presence of a d_{xy} "patch" on the electron pockets has been discussed before by many groups as possibly responsible for gap nodes (or minima) on the electron pockets. The present results show that such a minimum (or nodes) can arise *without* such an xy-patch, which is important to assess the impact of the various orbitals. The one-particle spectral function $A(\mathbf{k}, \omega)$ was also calculated, see Fig. 3.6. The left panels of Fig. 3.6 are for typical values of U and J$_H$/U in the regions of interest varying J$_{NN}$/U as indicated. The upper left panel is in the region of no binding, the middle left has B$_{2g}$ binding, while the lower left panel has A$_{1g}$ binding, when doped with two electrons. The quasiparticle-peak weights Z do not change much with respect to the noninteracting limit U=0. The right panels of Fig. 3.6 show the behavior of A(k,ω) now at fixed J$_{NN}$/U and J$_H$/U, varying U all the way to a regime where the system is insulating with a large gap. In spite of this gap opening and formation of the lower and upper Hubbard bands, the quasiparticle weights Z remain robust for the 8-site cluster here used. In fact, the weight reduction is not larger than 50 % at the largest U=20 (|t$_1$| units) investigated. Features on the scale of the magnetic or superconducting gaps cannot be resolved within the few momenta available, but the higher energy features at intermediate couplings are similar to non-interacting bands [Yu et al. (2009); Luo et al. (2010)], in agreement with ARPES experiments and with local density plus dynamical mean-field theory calculations [Aichhorn et al. (2009); Hansmann et al. (2010)].

As mentioned before, in physically relevant portions of the phase diagram [Yu et al. (2009); Luo et al. (2010)] the pairing symmetry $B_{2\mathrm{g}}$ competes with $A_{1\mathrm{g}}$. Three $B_{2\mathrm{g}}$ pairing operators with finite overlaps were found in this region: (v) $(\cos k_x + \cos k_y)\sigma_1$, (vi) $(\cos k_x \cos k_y)\sigma_1$, and (vii) $(\sin k_x \sin k_y)\sigma_0$. From Fig. 3.5(a) the interorbital operators (v) and (vi) have a much larger GS overlap than the intraorbital operator (vii). The mean-field calculation of the gaps for the symmetric combination of the

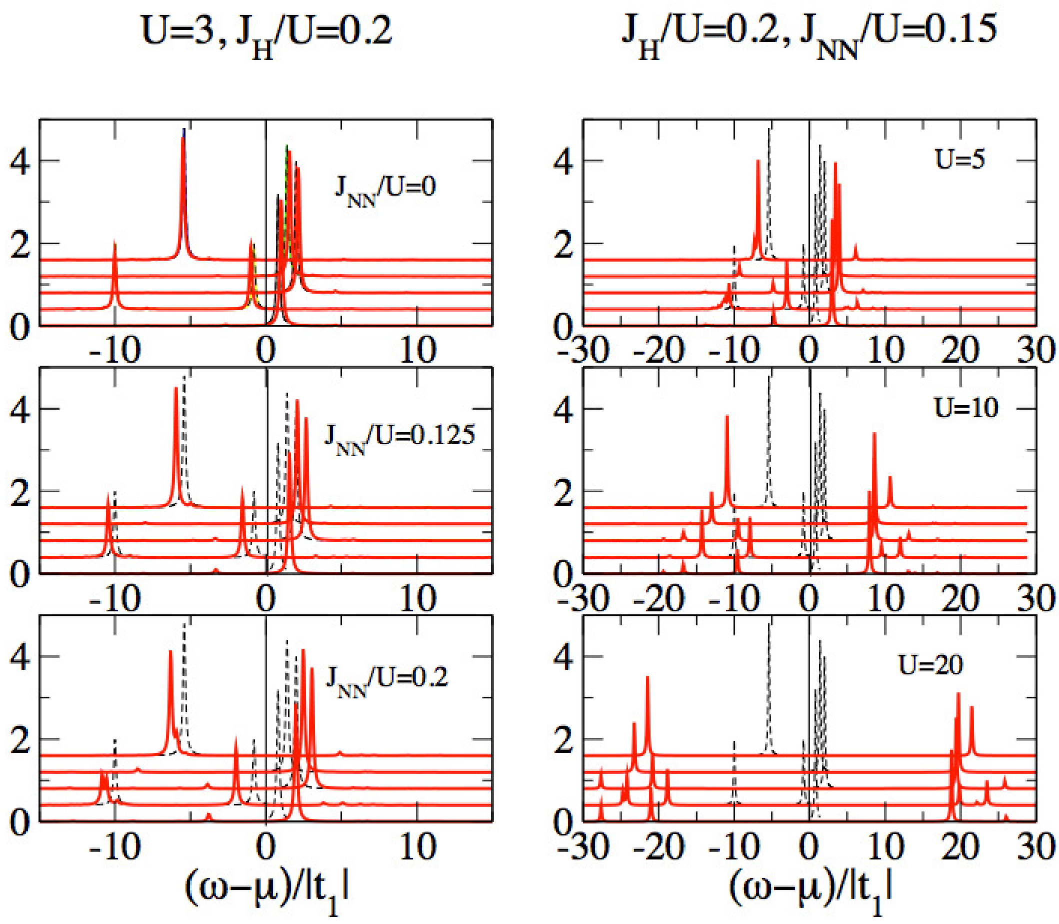

Figure 3.6: Spectral function A(k,ω) obtained with the Lanczos method on an 8-site cluster and with 16 electrons. Results shown are obtained varying couplings J$_{NN}$/U on the left panels and U on the right panels, as indicated. The momenta from the bottom to the top are (0, 0), (0, π), (π, π), ($\pi/2$, $\pi/2$), and ($\pi/2$, $\pi/2$). The results in the noninteracting limit U=J$_H$=J$_{NN}$=J$_{NNN}$=0 are indicated as dashed lines in all the panels for easy comparison. The quasiparticle weights remain robust in a wide range of couplings as compared with the noninteracting limit, at least for the small cluster here studied [Nicholson et al. (2011a)].

prevailing $B_{2\text{g}}$ pairing operators, i.e. (v)+(vi), is in Fig. 3.5(c). All the gaps have nodes along the x and y axes, also in good agreement with [Zeng et al. (2010)]. A strong $\mathbf{k}$ dependence is observed for all FS pockets, and the electron-pocket gaps are small ($\sim$ 1 meV).

3.3.3 Dynamical Pair Susceptibilities

To complete our analysis the dynamical pair susceptibilities, defined by

$$P(\omega) = \int_{-\infty}^{\infty} dte^{i\omega t} \langle \Delta_{\mathbf{k},i}(t) \Delta^{\dagger}_{\mathbf{k},i}(0) \rangle, \tag{3.5}$$

were also studied in the state with N=16 for the pairing operators $\Delta_{\mathbf{k},i}$. A procedure used in the context of the cuprates will be followed [Dagotto et al. (1990)]. Results for U=3 $|t_1|$, J_H/U=0.2, and several values of J_NN/U were obtained along the dot-dashed line (red) of Fig. 3.1(b). The overlaps calculation already indicated that for N=18 there are several low-lying energy states with different symmetries near the GS. The dynamical pair susceptibilities show that most of these low lying states have a large overlap with $\Delta^{\dagger}_{\mathbf{k},i}|\Psi_{N=16}(0)\rangle$ for $\Delta^{\dagger}_{\mathbf{k},i}$ with the appropriate symmetry. This is *qualitatively different* to the cuprates' t-J model, where the overlap of the doped GS with $\Delta^{\dagger}_{\mathbf{k},i}|\Psi(0)\rangle$ was large for Δ with d-wave symmetry but negligible for s-wave symmetry [Dagotto et al. (1990)]. In that s-wave case the spectral weight in $P(\omega)$ accumulates at high energies, while $P(\omega)$ for the d-wave pairing operator showed a well defined sharp peak at the GS energy of the doped state [Dagotto et al. (1990)]. This is not the case for the two-orbital model. For example, in Fig. 3.5(d) at J_NN/U=0.095, where the doped GS has symmetry $B_{2\text{g}}$, a sharp peak occurs in $P(\omega)$ for the $B_{2\text{g}}$ pairing operator (v), but a similar behavior is found in $P(\omega)$ for the $A_{1\text{g}}$ pairing operator (i) (the low-lying peak originates in a low-lying excited state with $A_{1\text{g}}$ symmetry). In addition, the susceptibility for a pairing operator (viii) $(\cos k_x + \cos k_y)\sigma_3$, NN version of the $B_{1\text{g}}$ operator (ix) $(\cos k_x \cos k_y)\sigma_3$, is also competitive (Fig. 3.5(d)).

3.3.4 Conclusions

The effects of NN and NNN Heisenberg terms on the symmetry and the binding energy of two electrons added to the undoped state of the two-orbital Hubbard model were studied using Lanczos techniques on small clusters. Quasi-nodal $A_{1\mathrm{g}}$ bound states are stabilized for physical values of J_H/U, in the intermediate/large U region, in agreement with RPA results [Graser et al. (2009)]. Our results also indicate that a competing $B_{2\mathrm{g}}$ state may become stable in physically relevant regimes of $U/|t_1|$. In addition, the pairing susceptibility presents low-lying excitations with $B_{2\mathrm{g}}$, $A_{1\mathrm{g}}$, and $B_{1\mathrm{g}}$ symmetries. Thus, pairing correlations with any of these symmetries could be stabilized by small modifications in the model parameters, in agreement with Refs. [Graser et al. (2009); Daghofer et al. (2008); Moreo et al. (2009b); Si and Abrahams (2008); Seo et al. (2008)]. This suggests that a similar sensitivity to small details may occur among different compounds of the pnictide family.

3.4 Hole Doped

An important characteristic of the widely studied Hubbard models for the pnictides/chalcogenides is that they are not particle-hole symmetric. On the experimental side, superconductivity has been found both upon electron and hole doping, but it seems that hole-doped materials belonging to the 122 family are more suitable for the use of surface-sensitive techniques which have revealed mostly nodeless gaps, while electron-doped materials belonging to the 1111 family are more easily studied with bulk techniques where indications of nodal superconductivity states have been found [Kondo et al. (2008); Ding et al. (2008); Grafe et al. (2008); Dong et al. (2010)]. Then, it is natural to wonder whether a potential source of the differences in the experimental results regarding the pairing symmetries may arise from the nature of the dopants.

As described in Chapter 2.2, due to the symmetry of the Fe-As planes [Raghu et al. (2008); Lee and Wen (2008)], it is possible to describe the pnictides using Fe-only effective models where the As atoms merely provide a bridge for the electronic hopping between the irons. Under this approximation only one Fe atom is left per unit cell to describe these materials. As a result of these considerations, the number of orbitals to be considered is reduced by half, which is a computational advantage, and the size of the Brillouin zone (BZ) is doubled. For this reason, the momentum in the unfolded zone is dubbed "pseudocrystal" momentum [Lee and Wen (2008)]. In order to relate the model results to experiments addressing the BZ corresponding to two Fe atoms, it is necessary to "fold" the extended BZ in such a way that the pseudocrystal momentum $\mathbf{k} = (\pi, \pi)$ is folded onto momentum $(0, 0)$. The physical difference between states with $\mathbf{k} = (0, 0)$ and (π, π) is that the first indicates a bonding and the second an anti-bonding combination of the d-orbitals in the two Fe atoms in the two-atoms unit cell. In the presentation of our results below, $\mathbf{k}$ will stand for pseudocrystal momentum.

3.4.1 Phase diagram

The relative symmetry between the undoped ($N = 16$) ground state (GS) and the $N = 14$ GS has been studied with the Lanczos technique varying $U/|t_1|$ and J_{H}/U. The undoped GS was found to have momentum $\mathbf{k} = (0, 0)$ and it transforms according to the A_{1g} representation of the D_{4h} group, for all the values of J_{H} and U studied here, in agreement with previous results [Moreo et al. (2009b)]. However, a surprising result found in the present study of the hole-doped extended two-orbital model is the presence of many competing low-energy states not only with different symmetries as in the electron doped case [Nicholson et al. (2011a)], but also with different pseudocrystal momenta $\mathbf{k}$. In other words, low lying states with both $\mathbf{k} = (0, 0)$ and (π, π) were found in our Lanczos investigation. This is compatible with previous mean-field approximation results that also reported low-energy spin-singlet pair states with momentum (π, π) [Gao et al. (2010)].

The competition among low-lying states with different symmetries and with different values of $\mathbf{k}$ is presented in Fig. 3.7 for the case $J_{\mathrm{H}}/U = 0.20$, without the extra "J" terms. Numerically, it was found that the ground state for 14 electrons has crystal momentum (π, π). For small values of U this state is a triplet with A_{2g} symmetry (open circles in the figure). With increasing U, a transition (via a level crossing) occurs at $U \sim 6|t_1|$ to a spin-singlet ground state with B_{2g} symmetry (open squares in the figure). However, it can be observed that there are states with $\mathbf{k} = (0, 0)$ that have very similar energies. For example, for this pseudocrystal momentum, and in the weak coupling regime, a spin-singlet state with B_{1g} symmetry (represented with filled triangles in the figure) is the closest in energy to the ground state, while for $U \geq 3|t_1|$ a spin-singlet state with A_{1g} symmetry prevails (represented with filled diamonds in the figure).

Similar results were found for all the values of U and J_{H} studied, i.e., the $N = 14$ ground state has total momentum $\mathbf{k} = (\pi, \pi)$ but there are $\mathbf{k} = (0, 0)$ states close in energy with a different symmetry. For this reason, the phase diagrams obtained by varying J_{H}/U and $U/|t_1|$ for *both* values of the pseudocrystal momentum will be presented.

The relative symmetry between the ground state with two electrons less than half filling with total pseudocrystal momentum $\mathbf{k} = (0, 0)$ and the undoped ground state is shown in Fig. 3.8(a), varying J_{H}/U and $U/|t_1|$. A region with symmetry B_{1g}, indicated by the triangles, is found for small $U/|t_1|$ (roughly $U/|t_1| \leq 3$) and moderate to large values of J_{H}/U. For larger values of $U/|t_1|$, the symmetry changes to A_{1g}. A similar transition from B_{1g} to A_{1g} (extended s-wave) has been found using the RPA technique for an electron-doped five-orbital model at $J_{\mathrm{H}} = 0$ [Graser et al. (2009)]. The binding energy E_{B}, defined as $E_{\mathrm{B}} = E(14) + E(16) - 2E(15)$, where $E(N)$ is the GS energy for N electrons, was also calculated. It was found that without the addition of Heisenberg terms there are no regions with binding.

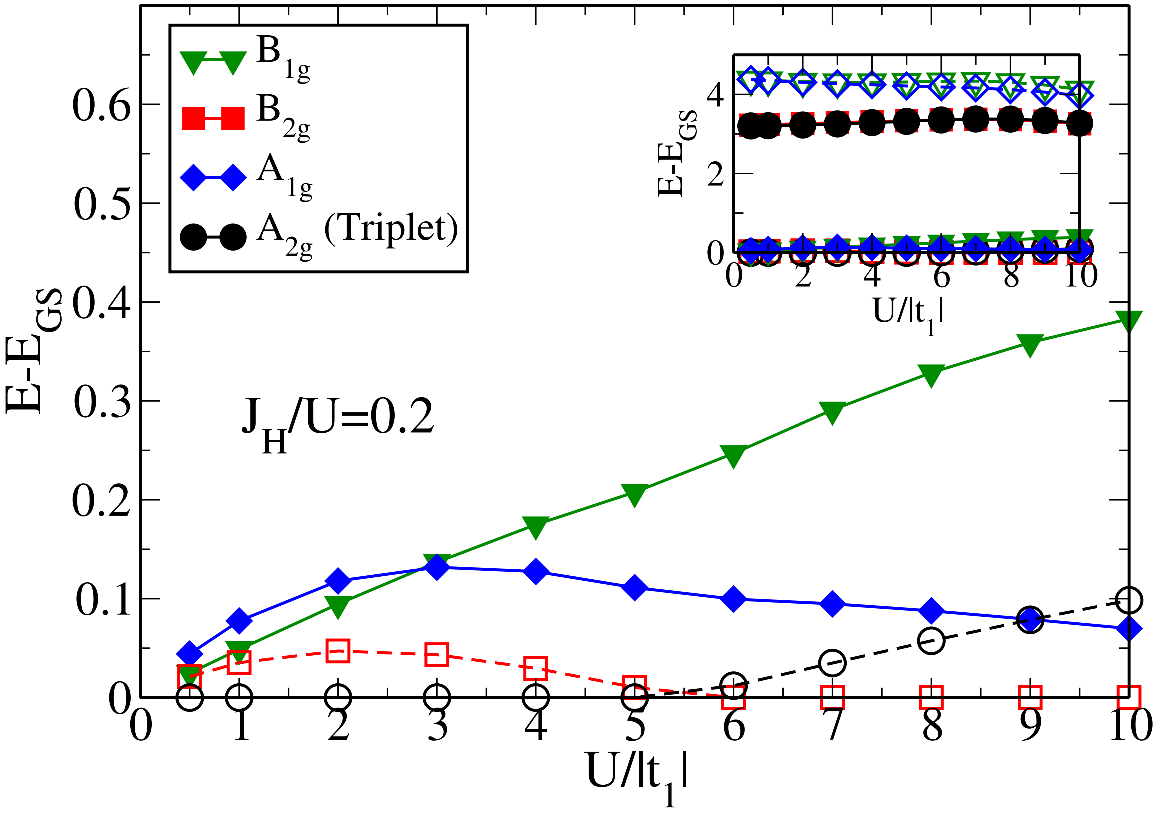

Figure 3.7: Difference between the energy of the lowest excited state with the symmetry and momentum indicated and the ground state. Full (open) symbols denote $\mathbf{k} = (0, 0)$ ($\mathbf{k} = (\pi, \pi)$). The results are obtained using the Lanczos algorithm for the two-orbital model in an eight-site cluster with 14 electrons (two holes doping), varying the Hubbard repulsion U, and at a fixed $J_{\mathrm{H}}/U = 0.20$. The inset shows a larger energy range in which the lowest lying state with each symmetry is displayed. The results shown in this figure are without the extra J_{NN} and J_{NNN} terms [Nicholson et al. (2012)].

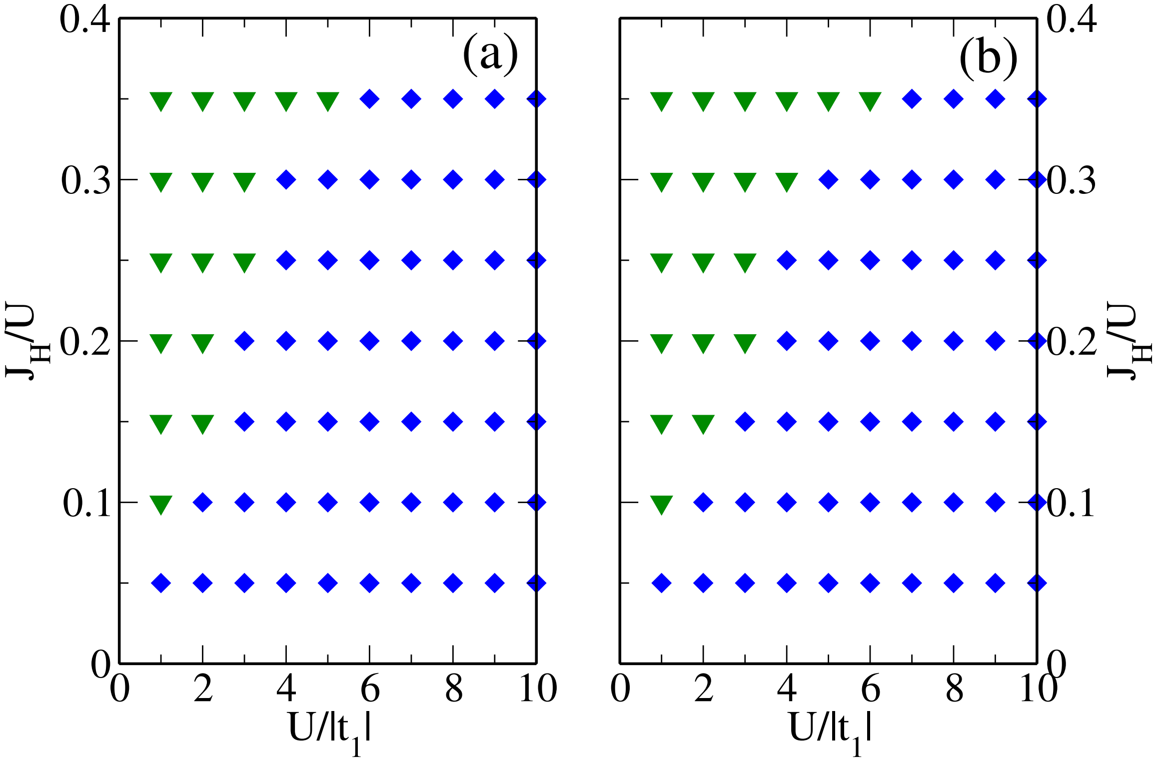

Figure 3.8: Relative symmetry between the N=16 (undoped) and N=14 (with $\mathbf{k} = (0,0)$) ground states, varying U and J_{H}/U. Triangles denote B_{1g}-symmetric singlets, and diamonds A_{1g}-symmetric singlets. (a) Results for couplings $J_{\mathrm{NN}} = J_{\mathrm{NNN}} = 0$. (b) Results for the lowest value of $(J_{\mathrm{NN}}, J_{\mathrm{NNN}})$ where binding appears with a fixed ratio $J_{\mathrm{NN}}/J_{\mathrm{NNN}} = 0.93$ [Nicholson et al. (2012)].

For the other case of a pseudocrystal momentum $\mathbf{k} = (\pi, \pi)$, the analogous numerical results are shown in Fig. 3.9(a). It was found that an A_{2g} spin-triplet ground state, indicated by circles in the figure, dominates for large values of J_{H}/U and small $U/|t_1|$. For the electron-doped model, an A_{2g} spin-triplet with momentum $(0, 0)$ was similarly observed at large J_{H} and small U [Daghofer et al. (2008); Moreo et al. (2009b)]. For smaller J_{H}/U and larger $U/|t_1|$, a spin-singlet ground state with B_{2g} symmetry is the ground state. For this pseudocrystal momentum, the binding energy was calculated as well: binding was obtained for $J_{\mathrm{H}}/U = 0.35$ where a spin-triplet ground state with symmetry A_{2g} prevails (see open triangles in the figure).

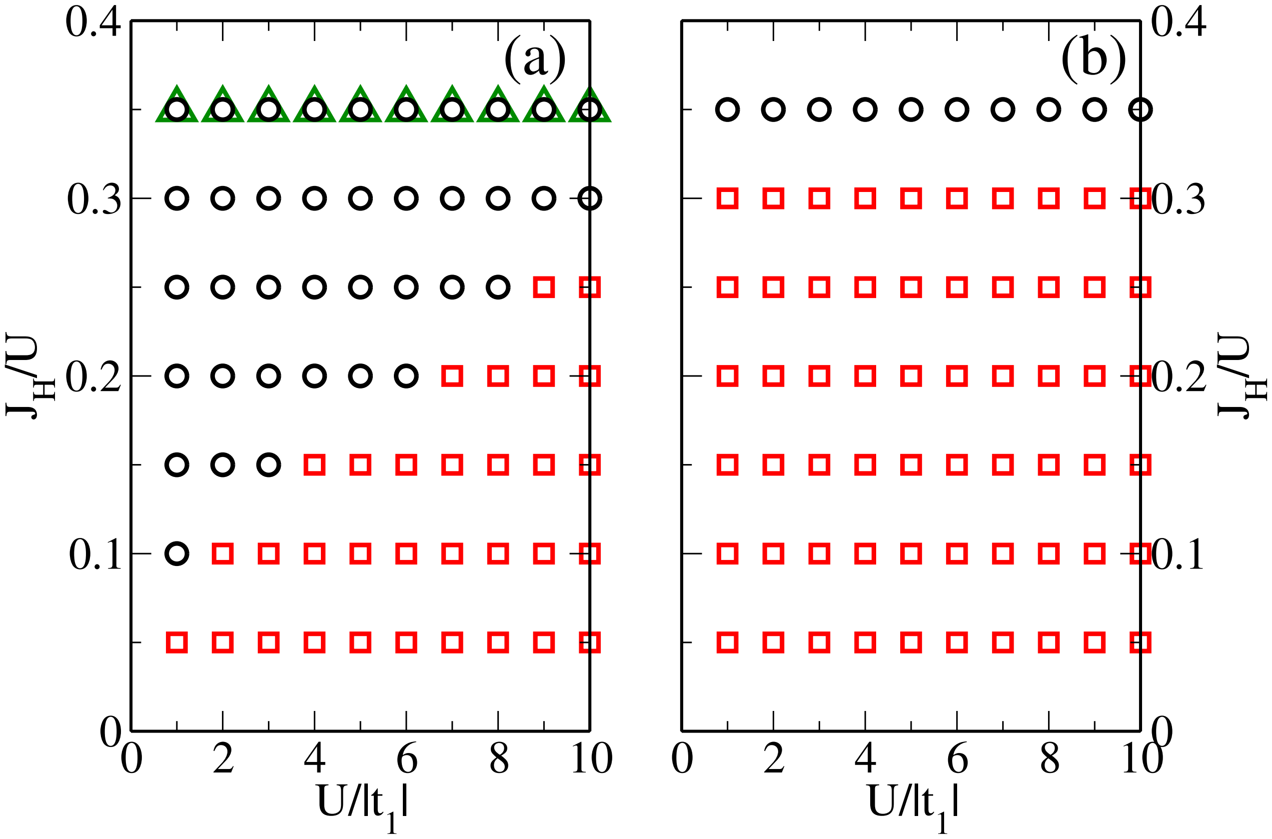

Figure 3.9: Relative symmetry between the N=16 (undoped) and N=14 (with $\mathbf{k} = (\pi, \pi)$) ground states varying U and $J_{\rm H}/U$. Circles denote spin-triplet states and squares B_{2g}-symmetric singlets. (a) Results for couplings $J_{\rm NN} = J_{\rm NNN} = 0$. Open triangles indicate binding. (b) Results for the lowest value of $(J_{\rm NN}, J_{\rm NNN})$ where binding appears with a fixed ratio $J_{\rm NN}/J_{\rm NNN} = 0.93$ [Nicholson et al. (2012)].

3.4.2 Binding stabilization

To stabilize hole binding in the two-orbital model, this section proceed in a similar manner as in the electron doped case described in Section 3.3 by adding extra Heisenberg terms, namely a NN coupling J_{NN} and a NNN coupling J_{NNN} as discussed in Section 3.2. As in the electron doped case, and as already explained, J_{NN} will be varied while $J_{\text{NN}}/J_{\text{NNN}}$ will be kept fixed at the value 0.93 [Nicholson et al. (2011a)].

The results for pseudocrystal momentum $\mathbf{k} = (0, 0)$ are presented in Fig. 3.8(b), showing the symmetry of the hole-doped ground state for the lowest value of J_{NN} where binding of holes is achieved. The phase diagram remains largely unchanged by the addition of the Heisenberg terms except for the B_{1g} region that has expanded slightly towards larger values of U. On the other hand, for states with momentum $\mathbf{k} = (\pi, \pi)$ the spin-triplet region virtually disappears (Fig. 3.9(b)), except for those triplet states that already had $E_B < 0$ at $J_{\text{NN}} = 0$, leaving behind a much larger B_{2g} region in parameter space.

In Fig. 3.10(a), the binding energy E_B *vs.* J_{NN}/U for states with momentum $\mathbf{k} = (0, 0)$ is shown for several values of U and at a fixed (realistic) $J_{\text{H}}/U = 0.2$. Increasing J_{NN} eventually induces binding for all U's. The value of J_{NN}/U where binding occurs decreases as U increases. Figure 3.11(a) shows the same information but for the states with momentum $\mathbf{k} = (\pi, \pi)$, where a similar qualitative behavior is observed.

A study of the binding energy E_{B} and the relative symmetry between the N=16 and 14 GS's allows us to construct phase diagrams in the $(U, J_{\text{NN}}/U)$ plane. In Fig. 3.10(b), typical results for the case $J_{\text{H}}/U = 0.2$ are shown for the states with total momentum $\mathbf{k} = (0, 0)$. The bound state has A_{1g} symmetry in most of the binding region, but a state with B_{1g} symmetry prevails at smaller U values ($\sim 3|t_1|$). In Fig. 3.11(b) the same information is displayed but for states with total momentum $\mathbf{k} = (\pi, \pi)$. In this case, the entire binding region, except for $J_{\text{H}}/U > 0.3$, has B_{2g} symmetry. All of the above symmetries appear inside the proper magnetic/metallic region of the undoped limit (indicated with shading in the figures) that were obtained in previous mean-field calculations [Yu et al. (2009); Luo et al. (2010)] extended to incorporate J_{NN} [Nicholson et al. (2011a)].

3.4.3 Magnetism

Since the two-orbital Hubbard model for the pnictides is not particle-hole symmetric, it is interesting to study how the nature of the doping, namely electrons vs. holes, affects the intensity of the magnetic order. In the actual materials, experimental results have shown that the in-plane resistivity of electron and hole-doped FeAs-based pnictides displays a larger anisotropy in the electron-doped case [Ying et al. (2011)]. Thus, it has been conjectured that the xz/yz magnetism is stronger in the electron-doped case, while in the hole-doped case it is weaker with a growing contribution of the xy orbital, disregarded in the two-orbital model, that forms the hole pocket around M [Ying et al. (2011)]. A similar conclusion was reached via the FLEX approximation for the case of electron and hole doping of a five-orbital Hubbard model [Ikeda et al. (2010)].

The results for the two-orbital model studied here are shown in Fig. 3.12 where the magnetic structure factor $S(\mathbf{k})$ is shown in the undoped (crosses), electron doped (circles), and hole-doped (diamonds) regimes, at fixed couplings $U = 3$, $J_{\mathrm{H}}/U = 0.2$, and $J_{\mathrm{NN}}/U = 0.2$, namely in the mean-field calculated "physical region" indicated in Fig. 3.11. While doping reduces the strength of the peak at $\mathbf{k} = (\pi, 0)$, it is interesting to notice that the intensity is slightly more reduced in the hole-doped case. These results lend qualitative support to the notion that the magnetism in the xz and yz orbitals is stronger in the electron-doped case, and it becomes reduced when holes are introduced.

3.4.4 Overlap Integrals

In this subsection, the functional forms of the hole pairing operators that produce the hole bound states will be analyzed. With this goal, the overlap defined by

$$\langle \Psi_{(N=14)}(\mathbf{k}')|\Delta_{\mathbf{k}'-\mathbf{k},i}|\Psi_{(N=16)}(\mathbf{k}=(0,0))\rangle \tag{3.6}$$

was calculated using the Lanczos algorithm along the paths indicated by the dotted lines in the phase diagrams shown in panels (b) of Figs. 3.10 and 3.11. Notice that for $|\Psi_{14}(\mathbf{k}')\rangle$ the pseudocrystal momentum $\mathbf{k}'$ will take the values $(0,0)$ and (π,π) and, thus, a pairing operator with the appropriate $\mathbf{k}'-\mathbf{k}$ has to be used to ensure a non-zero overlap. The ground state $|\Psi(N)\rangle$ in the subspace of N electrons was used, and the operator in Eqn. (3) was defined as

$$\Delta_{\mathbf{k},i} = \sum_{\alpha\beta} f(\mathbf{k})(\sigma_i)_{\alpha\beta} d_{\mathbf{k},\alpha,\uparrow} d_{\mathbf{k},\beta,\downarrow}, \tag{3.7}$$

where $d_{\mathbf{k},\alpha,\sigma}$ destroys an electron with spin z-axis projection σ, at orbital $\alpha = x, y$, and with momentum $\mathbf{k}$. The structure factor $f(\mathbf{k})$ arises from the spatial location of the fermions forming the pair, [Moreo et al. (2009b)] and σ_i are the Pauli matrices $(i = 1, 2, 3)$ or the 2×2 identity matrix σ_0 $(i = 0)$. Note that σ_1 and σ_2 imply an inter-orbital pairing. Overlaps for all the symmetries in Ref. [Moreo et al. (2009b)], and with NN and NNN locations for the electronic pairs, were numerically evaluated.

In Fig. 3.13(a), the overlaps for pairing operators with pseudocrystal momentum $\mathbf{k} = (0,0)$ are presented for values of U and J_{H} along the dotted path in Fig. 3.10(b). In the A_{1g} region in Fig. 3.13(a), the same four pairing operators that have a finite overlap in the electron doped case [Nicholson et al. (2011a)] also have one here. However, the relative strength of the overlaps differ. For consistency, the same labeling for the operators will be used as in Ref. [Nicholson et al. (2011a)]. The A_{1g} operator with the largest overlap is the operator (ii), i.e. the $s_{\pm}$ operator characterized by $f(\mathbf{k})\sigma_i = (\cos k_x \cos k_y)\sigma_0$, as in the electron doped case; [Nicholson et al. (2011a)] it is indicated by hollow diamonds in Fig. 3.13(a). However, in the hole-doped system the overlap for the pairing operator (iv) characterized by $(\cos k_x - \cos k_y)\sigma_3$ (hollow circles) follows in strength; this operator had the weakest overlap in the electron doped case [Nicholson et al. (2011a)]. The pairing operator (i) with $(\cos k_x + \cos k_y)\sigma_0$ (hollow squares) has an overlap almost as strong as in the electron-doped case. Finally, the overlap corresponding to the operator (iii)$(\sin k_x \sin k_y)\sigma_1$ (hollow triangles) is even more suppressed upon hole doping than upon electron doping.

In the region where the pairs have B_{1g} symmetry there are three pairing operators with large overlaps : (viii) $(\cos k_x + \cos k_y)\sigma_3$ (solid circles); (ix) $(\cos k_x \cos k_y)\sigma_3$ (solid diamonds); and (x) $(\cos k_x - \cos k_y)\sigma_0$ (solid squares). At small values of J_{NN}/U, (ix) has the largest overlap amplitude followed by (x) and (viii). However, as J_{NN}/U increases (viii) overtakes (ix).

For the case of pairing operators with pseudocrystal momentum $\mathbf{k} = (\pi, \pi)$, there is one contribution that clearly dominates, see Fig. 3.13(b): (vi′) $(\cos k_x \cos k_y)\sigma_1$ which corresponds to a NNN pair with B_{2g} symmetry. The prime in the label is used to remind the reader that the operator has a different pseudocrystal momentum from the B_{2g} state with the same label discussed in the electron-doped case [Nicholson et al. (2011a)]. The only other nonzero pairing overlap occurs for (vii′) $(\sin k_x \sin k_y)\sigma_0$ and has a much smaller amplitude than (vi′). Interestingly, the nearest-neighbor B_{2g} operator (v) characterized by $(\cos k_x + \cos k_y)\sigma_1$ that had the strongest overlap in the electron doped case [Nicholson et al. (2011a)] has zero overlap in the case studied in this manuscript. All the gaps for the pairing operators with B_{2g} symmetry have nodes along the x and y axes.

3.4.5 Dynamical Pair Susceptibilities

To complete our analysis, the dynamical pair susceptibilities defined as

$$P(\omega) = \int_{-\infty}^{\infty} dt e^{i\omega t} \langle \Delta^{\dagger}_{\mathbf{k},i}(t) \Delta_{\mathbf{k},i}(0) \rangle, \tag{3.8}$$

were also studied in the state with $N = 16$ for the pairing operators $\Delta_{\mathbf{k},i}$ introduced in Sec. 3.4.4. Notice that the calculated spectral decomposition involves excited states with $N = 14$. The procedure described in Ref. [Dagotto et al. (1990)] in the context of the cuprates will be followed. As discussed above, for $N = 14$ there are several low-energy states near the ground state that have different symmetries. The dynamical pair susceptibilities show that most of these low-lying states have a large overlap with $\Delta_{\mathbf{k},i}|\Psi_{\mathrm{N}=16}(0)\rangle$ for $\Delta_{\mathbf{k},i}$ with the appropriate symmetry. In Fig. 3.14, results for $U = 3|t_1|$, $J_{\mathrm{H}}/U = 0.2$, and $J_{\mathrm{NN}}/U = 0.10$ are presented. Large overlaps with low-lying $N = 14$ states are observed for operators (ii) and (iv) with A_{1g} symmetry and (viii) and (x) with B_{1g} symmetry, as well as for operator (vi′) with B_{2g} symmetry and pseudocrystal momentum $\mathbf{k} = (\pi, \pi)$.

It is interesting to compare the results obtained for the dynamical pair susceptibility upon hole doping with those obtained for electron doping [Nicholson et al. (2011a)]. In both cases, large susceptibilities for the low-lying states with A_{1g}, B_{1g}, and B_{2g} symmetries are found. This is remarkably different from the case of models for the cuprates where an analogous low-lying overlap analysis showed that $d_{x^2-y^2}$-wave symmetry clearly dominates over all others [Dagotto et al. (1990)].

Returning to pnictides, a similarity between the electron and hole-doped cases is that the B_{1g} pairing operator that has the highest susceptibility, state (viii), is different from the B_{1g} pairing state for the cuprates. It corresponds to Cooper pairs mainly located on NNN sites, as opposed to the dominant NN contribution in the cuprates, and in the orbital basis used here the B_{1g} symmetry is realized by the orbital degree of freedom. In addition, the susceptibilities indicate that while NN pairs are favored in the electron doped case, NNN have larger susceptibilities upon hole doping for A_{1g} and B_{2g} symmetries.

3.4.6 Conclusions

The properties of a recently introduced two-orbital extended Hubbard model for the pnictides have been studied upon hole doping with the help of the Lanczos method. The results were contrasted with the electron-doped case discussed in Section 3.3. Due to the lack of particle-hole symmetry in the Hamiltonian, the results, as expected, are quantitatively different in both cases. However, an additional surprising characteristic of the hole-doped ground state is that it has pseudocrystal momentum (π, π). In the reduced Brillouin zone representation corresponding to the physical two Fe-atoms per unit cell description of the pnictides, having a nonzero pseudocrystal momentum means that the ground state is characterized by anti-bonding rather than bonding combinations of the orbitals of the two Fe atoms in the unit cell. In terms of the pairing operators that are favored, it means that the pairs would arise from hole carriers located at the hole pockets at Γ and at M in the unfolded Brillouin zone. Interestingly, the five-orbital model for the pnictides [Kemper et al. (2010)] shows that upon hole doping a hole pocket, absent in the electron-doped case, develops around M and the role of this pocket plays an important role in the properties of the hole-doped materials [Kemper et al. (2010); Ikeda et al. (2010)]. Our results may indicate that a simple toy model, such as the two-orbital model, could be used to study the role that a hole-pocket at M plays when multi-orbital Hubbard models are hole-doped.

In spite of this difference in the pseudocrystal momentum quantum number, there are several commonalities between the hole- and electron-doped two-orbital Hubbard models. The most important feature is that there are several low-lying states with different symmetries close to the undoped ground state. For this reason, the symmetry of the doped states is strongly dependent on the actual values of the interaction parameters. Spin-singlet states that transform according to the irreducible representations A_{1g}, B_{1g}, and B_{2g} were obtained both for hole and for electron doping. The richness of the phase diagrams unveiled here, and in the cited previous investigations, suggests that the symmetry of the pairing state in the pnictides is likely to depend on the material as well as on the type of doped carriers (electrons or holes) and on the density of dopants.

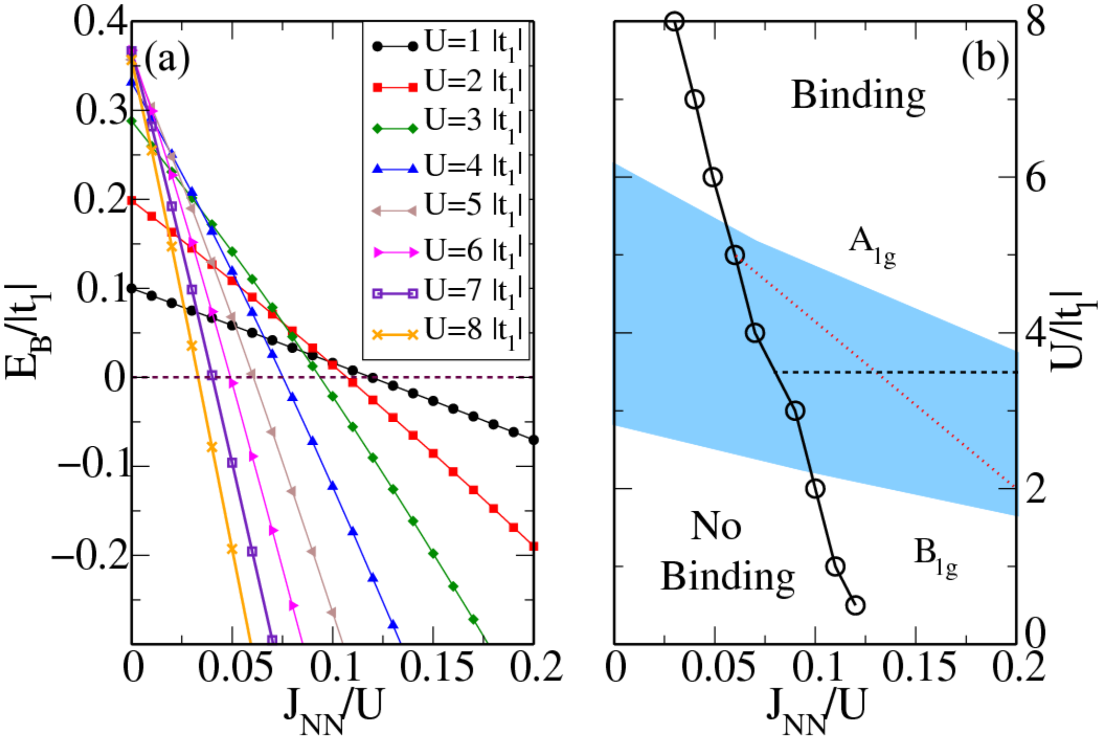

Figure 3.10: Results for states with total momentum $\mathbf{k} = (0, 0)$. (a) $E_{\mathrm{B}}/|t_1|$ *vs.* J_{NN}/U for different values of $U/|t_1|$, at $J_{\mathrm{H}}/U = 0.2$ and $J_{\mathrm{NN}}/J_{\mathrm{NNN}} = 0.93$. (b) Phase diagram showing “Binding” and “No Binding” regions and the symmetry of the two-hole bound state varying $U/|t_1|$ and J_{NN}/U, at a fixed $J_{\mathrm{H}}/U = 0.2$ [Nicholson et al. (2012)]. The shaded area indicates the so-called “physical region” obtained from standard mean-field calculations that were compared with neutrons, transport, and photoemission experimental results [Luo et al. (2010)]. The doted line is for Fig. 3.13 (a).

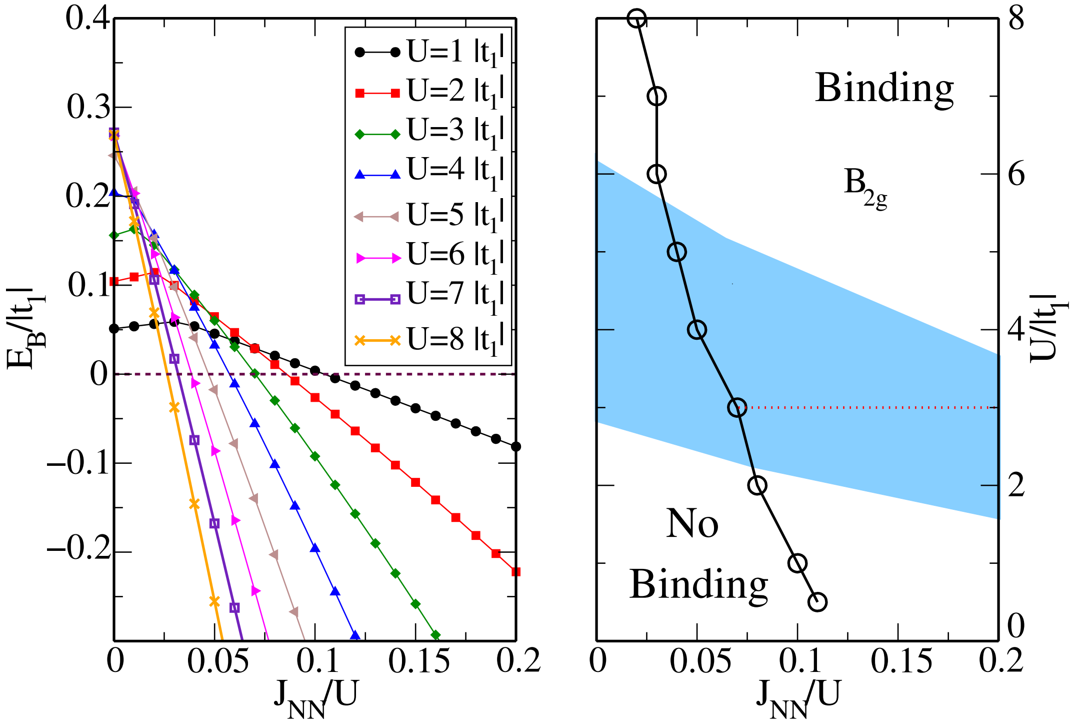

Figure 3.11: Results for states with total momentum $\mathbf{k} = (\pi, \pi)$. (a) $E_\mathrm{B}/|t_1|$ *vs.* J_NN/U for different values of $U/|t_1|$, at $J_\mathrm{H}/U = 0.2$ and $J_\mathrm{NN}/J_\mathrm{NNN} = 0.93$. (b) Phase diagram showing "Binding" and "No Binding" regions and the symmetry of the two-hole bound state varying $U/|t_1|$ and J_NN/U, at a fixed $J_\mathrm{H}/U = 0.2$ [Nicholson et al. (2012)]. The shaded region indicates the "physical region" according to standard mean-field calculations [Luo et al. (2010)]. The doted line is for Fig. 3.13(b).

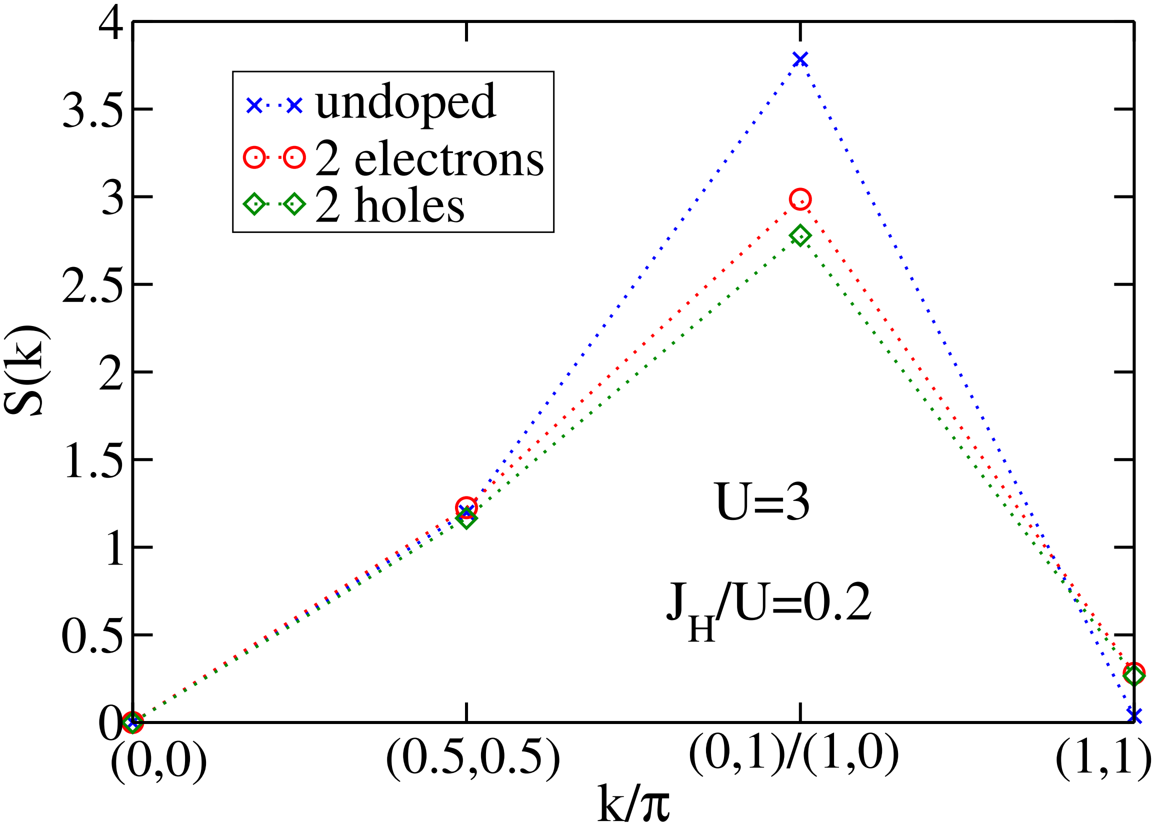

Figure 3.12: Numerically calculated magnetic structure factor $S(\mathbf{k})$, as a function of the momentum, using an eight sites cluster. Results for the undoped N=16, electron-doped N=18, and hole-doped N=14 cases are indicated, for couplings $U/|t_1| = 3$, $J_{\rm H}/U = 0.2$, and $J_{\rm NN}/U = 0.2$ [Nicholson et al. (2012)].

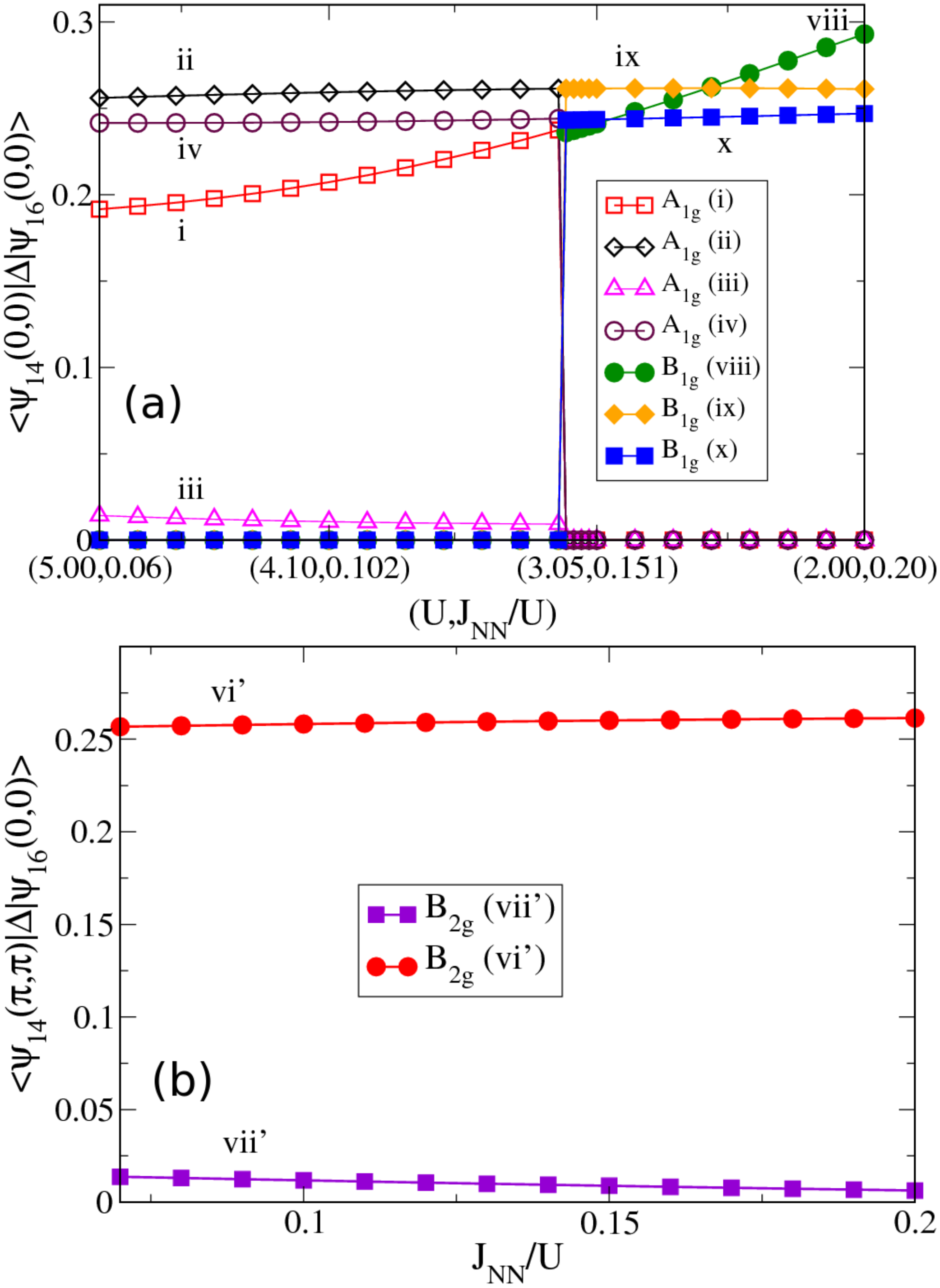

Figure 3.13: Overlap $\langle\Psi(N=14)|\Delta_{\mathbf{k},i}|\Psi(N=16)\rangle$ *vs.* $J_{\rm NN}/U$ for the indicated pairing operators, at $U = 3\ |t_1|$ and $J_{\rm H}/U = 0.2$, for (a) states with total momentum $\mathbf{k} = (0,0)$ along the dotted path in Fig. 3.10(b), and (b) states with total momentum $\mathbf{k} = (\pi,\pi)$ along the dotted path in Fig. 3.11(b) [Nicholson et al. (2012)].

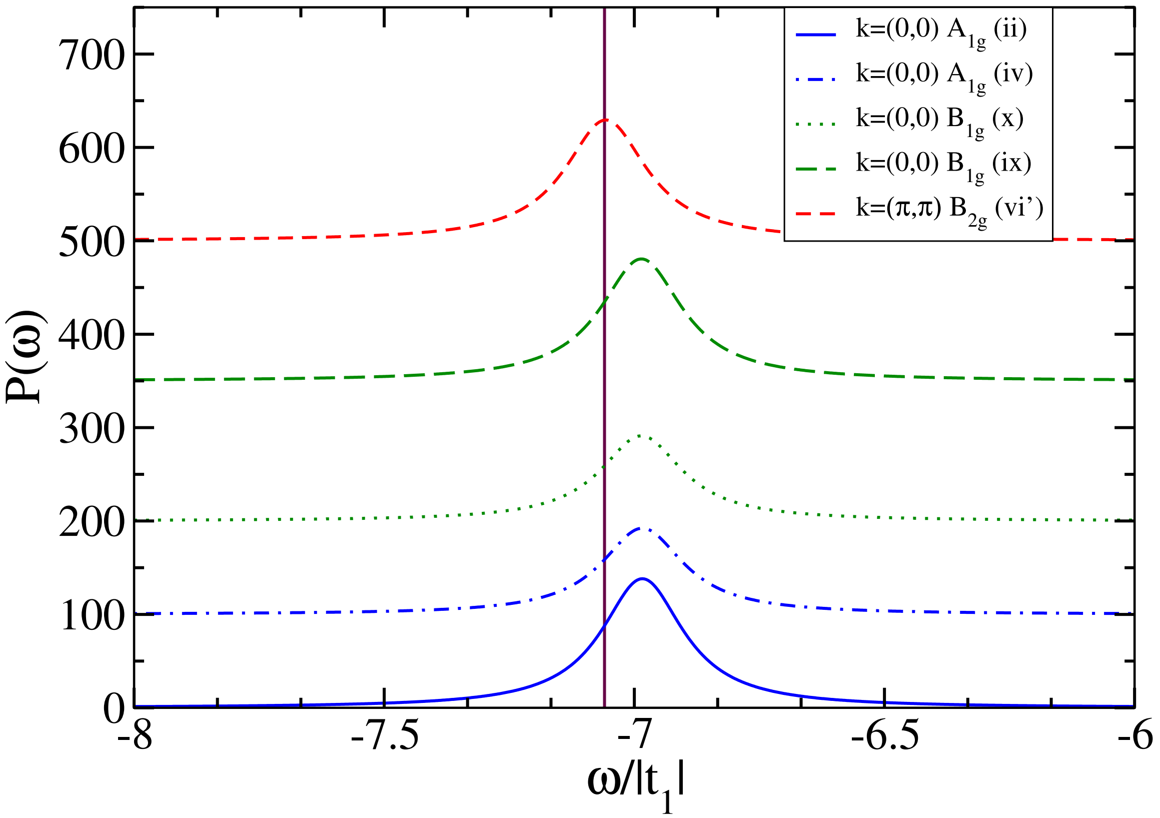

Figure 3.14: Dynamic pairing susceptibility for the pairing operators with total momentum $\mathbf{k} = (\pi, \pi)$ (operators with B_{2g} symmetry) and with total momentum $\mathbf{k} = (0, 0)$ (operators with B_{1g} and A_{1g} symmetry) (see text), at $U = 3.0\ |t_1|$, $J_\mathrm{H}/U = 0.2$, and $J_\mathrm{NN}/U = 0.10$. The vertical line indicates $E_{GS}(14) - E_{GS}(16)$ [Nicholson et al. (2012)].

Chapter 4

Two Orbital S-Model

4.1 Introduction

Among the several aspects of the study of the iron-based superconductors that are still controversial and unsettled, the following two questions have attracted considerable attention: *(i)* Does the magnetic order observed in the parent compounds [de la Cruz et al. (2008)] arise from the nesting properties of the non-interacting (or high temperature) Fermi surface [Mazin et al. (2008); Kuroki et al. (2008)] or should a better description be based on the super-exchange Heisenberg interactions between localized magnetic moments [Si and Abrahams (2008)]? *(ii)* What is the pairing mechanism, to what extent is the pairing symmetry determined by nesting and, what is the actual symmetry and momentum dependence of the pairing operator? In particular, what is the role that the orbital degrees of freedom play in this context?

The origin of the magnetic state is being vigorously debated. One proposal, based on fermiology, is the excitonic mechanism in which electron-hole pairs are formed by one electron and one hole from different FS's nested with nesting vector **Q**. In this context most studies disregard the orbital structure of the bands [Mazin et al. (2008); Chubukov et al. (2008); Cvetkovic and Tesanovic (2009); Brydon and Timm (2009)] while others stress the role played by their orbital composition [Raghu et al.

(2008); Daghofer et al. (2008); Graser et al. (2009); Moreo et al. (2009b); Kemper et al. (2010); Yu et al. (2009); Luo et al. (2010); Daghofer et al. (2010)]. Another approach focuses on the order of the localized moments that develop in the presence of strong Coulomb interactions [Si and Abrahams (2008); Yildirim (2008); Uhrig et al. (2009); Krüger et al. (2009)] and relies on ab initio results [Nakamura et al. (2008); Anisimov et al. (2009)] that suggest that the pnictides are moderately, rather than weakly, correlated, conclusion supported by photoemission measurements indicating mass enhancements due to electron correlations as large as 2-3 [Luo et al. (2010)].

The pairing mechanism in the pnictides is also controversial. Most of the pairing operators that have been proposed in the literature either ignore the multi-orbital characteristics of the problem or consider Cooper pairs that are made out of electrons located at the same orbital. A majority of these previous studies have been performed in the weak coupling limit. The original proposal of the $s_{\pm}$ pairing state dealt with the overall symmetry of the pairing operator but without distinguishing among the spatial vs. orbital contributions to its particular form [Mazin et al. (2008); Kuroki et al. (2008)]. Other authors [Zhang et al. (2009)] have considered a spin-fluctuation-induced pairing interaction and also assumed that Cooper pairs are predominantly made of electrons in the same orbital. A Random-Phase Approximation (RPA) analysis [Graser et al. (2009)] concluded that the pairing is, again, intraorbital, both for the A_{1g} (s-wave) and B_{1g} (d-wave) symmetries. Among the authors that have used the conceptually different strong coupling approach, some have studied effective single orbital models [Si and Abrahams (2008)] while others incorporated two orbitals [Goswami, Pallab et al. (2010)], but still only considering intra-orbital pairing operators. The same model was also studied under a mean-field approximation [Seo et al. (2008)] with the assumption that exchange takes place between spins on the same orbitals and, again, only intraorbital pairs were proposed.

Among the early first studies of multi-band superconductors, [Suhl et al. (1959)] considered two tight-binding bands, hypothetically identified with s and d orbitals, and the effect of weak electron-phonon interactions. Under these assumptions, it was reasonable to expect that the Cooper pairs would be formed by electrons belonging to the same band. However, the actual orbital composition of the pairs was not addressed. The interacting portion of the Hamiltonian was written in the band representation and this model was proposed by analogy with models used in the BCS theory, assuming that emission and absorption of a phonon could occur in four ways. These four processes corresponded to pair scattering within each of the two FS's and pair hopping from one FS to the other. This last process would occur if the exchanged phonon has enough momentum to allow the Cooper pair to jump from a FS to the other, and it can occur even if the orbitals do not hybridize to form the bands [Hotta (2010)]. In this case, the expected pairing operator is the traditional on-site s-wave state of the BCS theory, with a momentum independent gap. In principle, independent gaps may arise on the different FS's [Suhl et al. (1959)] unless the orbitals are hybridized by the symmetries of the Hamiltonian, in which case the gaps will have to be related to each other and obey the symmetries of the system. [Moreo et al. (2009b)].

The previous discussion applies to superconductors driven by the electron-phonon interaction. However, it is believed that the most relevant interactions in the pnictides are the Coulomb repulsion and Hund magnetic exchange. These interactions are more easily expressed in real space and in the orbital representation. In fact, the effective form of the Coulomb interaction in the band representation is more complicated than the expression provided by [Suhl et al. (1959)] for the electron-phonon interaction. In particular, it has been shown [Chubukov et al. (2008)] that a pair hopping term, such as the one introduced by Suhl *et al.* occurs only if the orbitals get hybridized to form the bands. If the orbitals are *not* hybridized this type of term is not present in the effective interaction Hamiltonian. In addition, when the bands are made of hybridized orbitals, as it is the case for the iron pnictides, [Boeri et al. (2008)] the actual orbital structure of the pairs needs to be considered since due to the Coulomb repulsion on-site pairing is not expected to occur, and the overall symmetry properties of the pairing operators may be a function of their spatial and orbital components, see Eqn. 2.30.

To understand the role that the orbitals play in the case of electrons with strongly hybridized bands that are interacting via the Coulomb repulsion, as believed to occur in the case of the pnictides in the context of the magnetic scenario for superconductivity, in this chapter Lanczos numerical, Hartree mean-field, and RPA studies of two different two-orbital models will be presented and discussed, both displaying identical Fermi surfaces. One of them is the well-known and widely used two-orbital model for the pnictides, introduced in Section 2.2.4, based on the two strongly hybridized degenerate d_{xz} and d_{yz} orbitals of iron, while the second is a two-band "toy- model" (dubbed the *s*-model) whose bands arise from two non-hybridized, non-degenerate, *s*-like orbitals that is introduced here for the first time. The latter model has a FS qualitatively similar to that of the pnictides. In both cases a hole (electron) FS is located at the Γ/M (X/Y) points of the Brillouin zone (BZ). The hole and electron FS's are connected by nesting vectors $(\pi, 0)$ and $(0, \pi)$. The role that the nesting and the orbitals play in the magnetic and pairing properties of these models will be here investigated and discussed, both in the weak and strong coupling regimes.

Besides its conceptual relevance, the results presented here should also be framed in the context of recent bulk-sensitive laser angle-resolved photoemission (ARPES) experiments [Shimojima et al. (2010)] on $BaFe_2(As_{0.65}P_{0.35})_2$ and $Ba_{0.6}K_{0.4}Fe_2As_2$. The main conclusion of Ref. [Shimojima et al. (2010)] is the existence of orbital independent superconducting gaps that are not expected from spin fluctuations and nesting mechanisms, but are claimed to be better explained by magnetism-induced interorbital pairing and/or orbital fluctuations. This is argued based on the observation that the $3z^2 - r^2$ orbital that forms one of the hole pockets at the BZ center, but that does not have a nested partner with the same orbital at the electron pockets, nevertheless appears to develop a superconducting gap. Another interesting experimental result that challenges the role of nesting in the physics of the pnictides is a careful measurement of the de Haas-van Alphen (dHvA) effect in $BaFe_2P_2$, the end member of the series $BaFe_2(As_{1-x}P_x)_2$, indicating that this non-magnetic and non-superconducting compound displays the best nesting of all the compounds in the series [Arnold et al. (2011)]

This chapter is organized as follows. In Section 4.2 the models are introduced. The magnetic properties are presented in Section 4.3 while the pairing properties are the subject of Section 4.4. Section 4.5 is devoted to the conclusions.

4.2 Models

4.2.1 *d*-model

The reference model that will be considered here is the widely-used two-orbital model, introduced in Section 2.2.4, based on the d_{xz} (x) and d_{yz} (y) Fe orbitals of the pnictides An important characteristic of the two degenerate *d*-orbitals in this model is that around the hole pockets a spinor describing the mixture of orbitals rotates twice on encircling these FS's. The inversion and time reversal symmetry of the twice degenerate d bands ensures that at each $\mathbf{k}$ point it is possible to choose real spinor wavefunctions that are confined to a plane. The spinor has vorticity ± 2 around the hole pockets while there is no vorticity around the electron pockets [Ran et al. (2009)]. As pointed out in [Ran et al. (2009)], this topological characterization of the hole and electron pockets is also a characteristic of all the more realistic models for the pnictides that include additional orbitals.

4.2.2 *s*-model

Let us introduce now a two-orbital model with two non-degenerate non-hybridized s-like bands, called s_1 and s_2, with dispersion relations given by:

$$\xi_{s_1}(\mathbf{k}) = 2t_1(\cos k_x + \cos k_y) + 4t_2 \cos k_x \cos k_y - \mu, \tag{4.1}$$

and

$$\xi_{s_2}(\mathbf{k}) = 2t_3(\cos k_x + \cos k_y) + 4t_4 \cos k_x \cos k_y - \mu + \Delta, \tag{4.2}$$

where μ is the chemical potential and Δ is the energy difference between the two bands. The dispersions can also be written in the basis (s_1, s_2), i.e., $(1, 2)$, using the τ_i matrices as in Eqn. 2.26:

$$\begin{aligned}\xi_S(\mathbf{k}) =&[(t_1 + t_3)(\cos k_x + \cos k_y) + 2(t_2 + t_4) \cos k_x \cos k_y - \mu + \frac{\Delta}{2}]\tau_0 \\ &+ [(t_1 - t_3)(\cos k_x + \cos k_y) + 2(t_2 - t_4) \cos k_x \cos k_y - \frac{\Delta}{2}]\tau_3.\end{aligned} \tag{4.3}$$

It is clear that here both τ_0 and τ_3 transform like A_{1g} and for this reason this model will be called the *s*-model. In Fig. 4.1, the band dispersion (panel (a)) and the FS (panel (b), red circles) are shown for the parameter values $t_1 = -0.05$, $t_2 = 0.7$, $t_3 = -0.1$, $t_4 = 0.3$, $\Delta = 2.8$ and $\mu = 1.95$. The FS of the *d*-model is also shown (continuous black line) for comparison. They are obviously very similar, and precisely the goal of this effort is to investigate what kind of magnetic and pairing properties emerge from these two models that have nearly equal Fermi surfaces.

The hole pockets at the Γ and M points nest into the electron pockets at X and Y, with nesting vectors $(0, \pi)$ and $(\pi, 0)$. The system is half-filled but the individual bands/orbitals are not. Note that this is the case with the orbitals in the multi-orbital systems proposed for the pnictides, where nesting occurs between electron and hole pockets at the FS but none of the orbitals is exactly half-filled [Graser et al. (2009); Kuroki et al. (2008)].

4.2.3 Coulomb Interaction

The Coulomb interaction term in both Hamiltonians is the usual one, first introduced in Section 2.3, with an on-site intraorbital (interorbital) Coulomb repulsion U (U'),

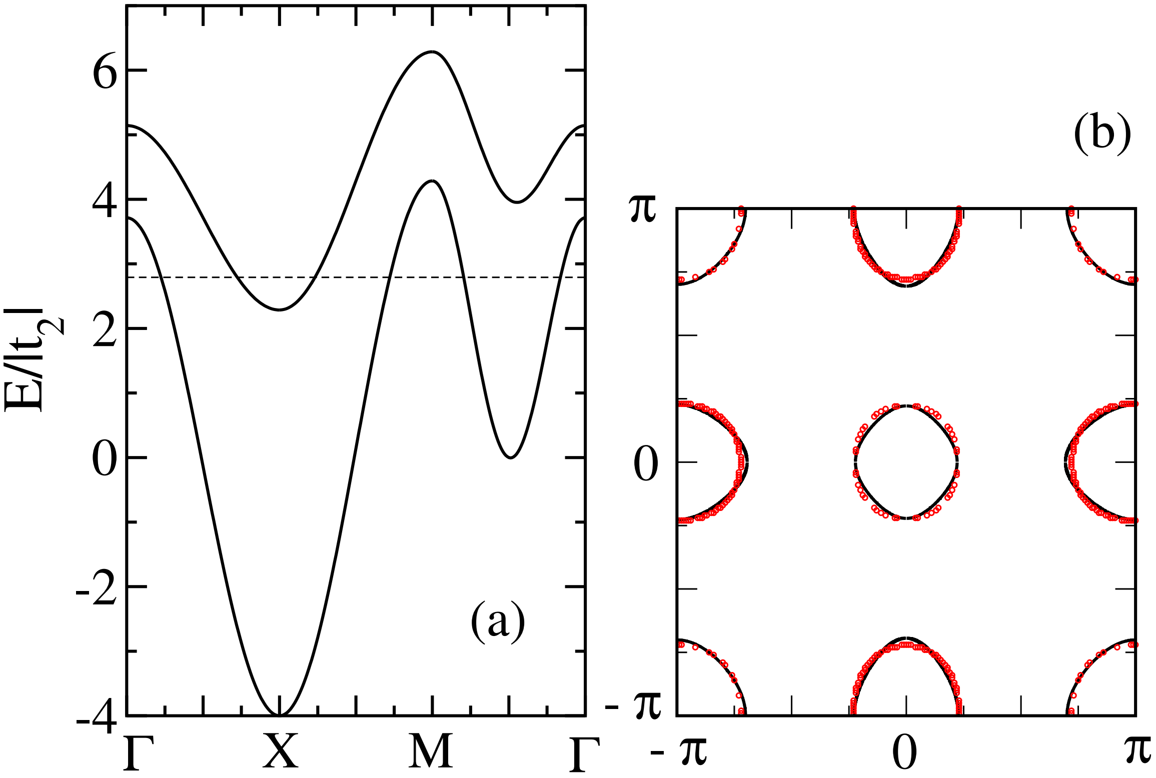

Figure 4.1: (a) Band dispersion and (b) Fermi surface of the half-filled two-orbital s-model given by Eqn. (4.3) (red circles). The continuous line is the FS for the two-orbital d-model [Nicholson et al. (2011b)].

and a Hund coupling J satisfying the relation $U'{=}U-2J$ for simplicity, and a pair-hopping term with coupling $J'{=}J$ [Oles (1983)]. The full interaction term is given by

$$\begin{aligned} H_{int} = U\sum_{\mathbf{i},a} n_{\mathbf{i},a,\uparrow}n_{\mathbf{i},a,\downarrow} + \frac{(U'-J/2)}{2}\sum_{\mathbf{i},a} n_{\mathbf{i},a}n_{\mathbf{i},-a} \\ -J\sum_{\mathbf{i},a}\mathbf{S}_{\mathbf{i},\mathbf{a}}\cdot\mathbf{S}_{\mathbf{i},-\mathbf{a}} + \frac{J}{2}\sum_{\mathbf{i},a}(d^{\dagger}_{\mathbf{i},a,\uparrow}d^{\dagger}_{\mathbf{i},a,\downarrow}d_{\mathbf{i},-a,\downarrow}d_{\mathbf{i},-a,\uparrow} + h.c.), \end{aligned} \tag{4.4}$$

where $d^{\dagger}_{\mathbf{i},a,\sigma}$ creates an electron with spin σ at site $\mathbf{i}$ and orbital $a = x, y$ or 1, 2. $\mathbf{S}_{\mathbf{i},a}$ ($n_{\mathbf{i},a}$) is the spin (electronic density) of the orbital a at site $\mathbf{i}$.

4.3 Magnetic Properties

For a single-orbital model, the magnetic structure factor is easily defined as

$$S(\mathbf{k}) = \sum_{\mathbf{r}} e^{i\mathbf{k}.\mathbf{r}}\omega(\mathbf{r}), \tag{4.5}$$

with

$$\omega(\mathbf{r}) = \frac{1}{N}\sum_{\mathbf{i}} m(\mathbf{i})m(\mathbf{i}+\mathbf{r}), \tag{4.6}$$

where N is the number of sites of the lattice and

$$m(\mathbf{i}) = n_{\mathbf{i},\uparrow} - n_{\mathbf{i},\downarrow} = d^{\dagger}_{\mathbf{i},\uparrow}d_{\mathbf{i},\uparrow} - d^{\dagger}_{\mathbf{i},\downarrow}d_{\mathbf{i},\downarrow}, \tag{4.7}$$

where $m(\mathbf{i})$ denotes the net magnetization at site $\mathbf{i}$.

In a multi-orbital system the net magnetization at site $\mathbf{i}$ is obtained in terms of the magnetization of each orbital a, and it is given by

$$m(\mathbf{i}) = \sum_{a} n_{\mathbf{i},a,\uparrow} - n_{\mathbf{i},a,\downarrow} = \sum_{a}(d^{\dagger}_{\mathbf{i},a,\uparrow}d_{\mathbf{i},a,\uparrow} - d^{\dagger}_{\mathbf{i},a,\downarrow}d_{\mathbf{i},a,\downarrow}). \tag{4.8}$$

While Eqn. 4.8 characterizes the magnetization that is measured in experiments such as neutron scattering, it is natural to define generalized magnetic moments $m_{ab}(\mathbf{i})$ [Ran et al. (2009)] given by

$$m_{ab}(\mathbf{i}) = d^{\dagger}_{\mathbf{i},a,\uparrow} d_{\mathbf{i},b,\uparrow} - d^{\dagger}_{\mathbf{i},a,\downarrow} d_{\mathbf{i},b,\downarrow}. \tag{4.9}$$

With this definition, a generalized form of the magnetic correlation functions will depend on 4 orbital indices:

$$\omega_{abcd}(\mathbf{r}) = \frac{1}{N} \sum_{\mathbf{i}} m_{ab}(\mathbf{i}) m_{cd}(\mathbf{i}+\mathbf{r}). \tag{4.10}$$

Thus, it is possible to define orbital dependent magnetic structure factors given by:

$$S_{abcd}(\mathbf{k}) = \sum_{\mathbf{r}} e^{i\mathbf{k}.\mathbf{r}} \omega_{abcd}(\mathbf{r}). \tag{4.11}$$

These orbital-dependent operators may arise from processes as those depicted in panel (a) of Fig. 4.2, where having different orbitals at the two vertices is possible if the orbitals strongly hybridize to form a band [Kemper et al. (2010)].

The total orbital magnetic structure factor can then be defined as:

$$S_{TO}(\mathbf{k}) = \sum_{a,b,c,d} S_{abcd}(\mathbf{k}). \tag{4.12}$$

Note that there are M^4 orbital dependent components of the generalized magnetic structure factor, where M is the number of active orbitals in the system. The magnetization that is measured in neutron scattering experiments is given by Eqn. 4.8, which in terms of the components of the tensor m_{ab} becomes

$$m(\mathbf{i}) = \sum_{a} n_{\mathbf{i},a,\uparrow} - n_{\mathbf{i},a,\downarrow} = \sum_{a} m_{aa}(\mathbf{i}) = tr[m_{ab}(\mathbf{i})]. \tag{4.13}$$

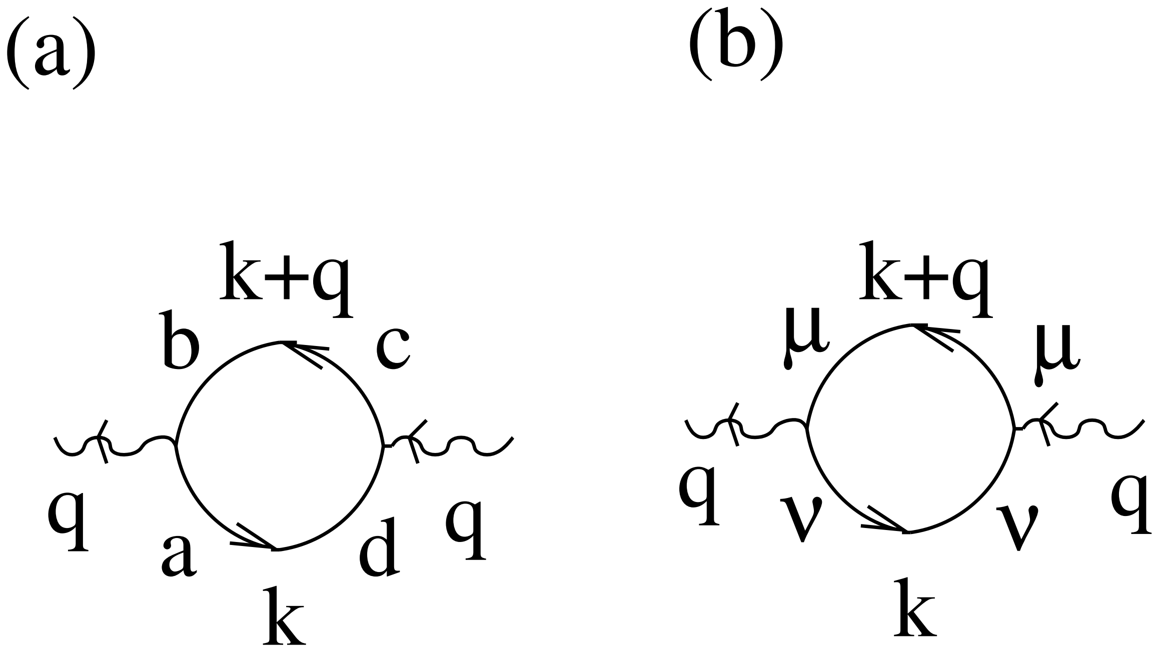

Figure 4.2: (a) Electronic process that gives rise to the orbital components of the structure factor. (b) Same as (a) but in the band representation [Nicholson et al. (2011b)].

Since $m(\mathbf{i})$ is a trace its value is independent of the basis chosen to define the orbitals and it allows to calculate the experimentally measured local magnetization.

Notice that $m(\mathbf{i})$ is the operator that has to be considered in order to construct the so-called homogeneous or diagonal structure factor defined in terms of the diagonal (intra-orbital) magnetic moments $m_{aa}(\mathbf{i})$ and given by [Graser et al. (2009); Moreo et al. (2009b)]

$$S_{MO}(\mathbf{k}) = \frac{1}{N}\sum_{a,b,\mathbf{r},\mathbf{i}} e^{i\mathbf{k}.\mathbf{r}} m_{aa}(\mathbf{i}) m_{bb}(\mathbf{i}+\mathbf{r}) = \sum_{a,b} S_{aabb}(\mathbf{k}). \tag{4.14}$$

S_{MO} is the physical magnetic structure factor that has to be calculated in the context of multi-orbital systems to compare with neutron scattering results [Daghofer et al. (2008); Moreo et al. (2009b)]. Several authors have pointed out the existence of the generalized components of the magnetic susceptibility both in the orbital representation [Graser et al. (2009); Brydon et al. (2011)] and in the band representation [Brydon and Timm (2009)]. It has also been pointed out that an orbital-transverse density-wave (OTDW) ordered state characterized by the non-homogeneous components of the magnetization tensor may develop in multi-orbital systems [Yao, Zi-Jian et al. (2011)], an issue that will be further explored and discussed in the present work.

4.3.1 Non-interacting case

In order to understand the relationship between S_{TO}, S_{MO}, and the properties of the FS of the system, it is illuminating to consider the non-interacting case which can be easily studied in momentum space. Via a Fourier transform of $d^{\dagger}_{\mathbf{i},a,\sigma}$ and $d_{\mathbf{i},a,\sigma}$, S_{abcd} in Eqn. 4.11 can be written as

$$S_{abcd}(\mathbf{k}) = \sum_{\mathbf{p},\mathbf{q},\sigma,\sigma'} (-1)^{\sigma+\sigma'} d^{\dagger}_{\mathbf{q},a,\sigma} d_{\mathbf{q+k},b,\sigma} d^{\dagger}_{\mathbf{p},c,\sigma'} d_{\mathbf{p-k},d,\sigma'}. \tag{4.15}$$

In momentum space it is natural to use the band representation in which

$$S_{abcd}(\mathbf{k}) = \sum_{\mathbf{p},\mathbf{q},\sigma,\sigma',\mu,\mu',\nu,\nu'} (-1)^{\sigma+\sigma'} <\mu|a>_{\mathbf{q}} <b|\mu'>_{\mathbf{q+k}} <\nu|c>_{\mathbf{p}} <d|\nu'>_{\mathbf{p-k}} \\ d^{\dagger}_{\mathbf{q},\mu,\sigma} d_{\mathbf{q+k},\mu',\sigma} d^{\dagger}_{\mathbf{p},\nu,\sigma'} d_{\mathbf{p-k},\nu',\sigma'}, \tag{4.16}$$

where $d^{\dagger}_{\mathbf{p},\nu,\sigma}$ creates an electron with momentum $\mathbf{p}$ and z-spin component σ at band ν, while $<\nu|a>_{\mathbf{p}}$ is the matrix element for the transformation from orbital to band representation.

In the band representation, the electronic processes that contribute to the magnetic correlations are shown in panel (b) of Fig. 4.2. Since the electronic band cannot change as the electron created at the right vertex is destroyed at the left vertex, in the band representation the band-dependent components of the structure factor are given by

$$S_{\mu\nu\nu\mu}(\mathbf{k}) = \sum_{\mathbf{p},\mathbf{q},\sigma} d^{\dagger}_{\mathbf{q},\mu,\sigma} d_{\mathbf{q}+\mathbf{k},\nu,\sigma} d^{\dagger}_{\mathbf{p},\nu,\sigma} d_{\mathbf{p}-\mathbf{k},\mu,\sigma}, \tag{4.17}$$

where the Greek indices label the bands. A total structure factor can be defined in terms of $S_{\mu\nu\nu\mu}$ as

$$S_{TB}(\mathbf{k}) = \sum_{\mu,\nu} S_{\mu\nu\nu\mu}(\mathbf{k}). \tag{4.18}$$

Also the homogeneous or diagonal magnetic structure factor S_{MB}, analogous of S_{MO}, can be defined as

$$S_{MB}(\mathbf{k}) = \sum_{\mu} S_{\mu\mu\mu\mu}(\mathbf{k}), \tag{4.19}$$

since in the band representation $S_{\mu\mu\nu\nu} = 0$, if $\mu \neq \nu$. Note that the band representation is the natural starting point in approaches based on fermiology [Mazin et al. (2008); Chubukov et al. (2008)].

In the noninteracting case being considered in this section, it is easy to show that

$$S_{\mu\nu\nu\mu}(\mathbf{k}) = 2\sum_{\mathbf{q}} f_{\mu}(\mathbf{q})[1 - f_{\nu}(\mathbf{q}+\mathbf{k})], \tag{4.20}$$

where $f_{\mu}(\mathbf{q})$ is the Fermi function for the band μ. The components of the structure factor in the orbital representation are given by

$$S_{abcd}(\mathbf{k}) = 2\sum_{\mathbf{q},\mu,\nu} <\mu|a>_{\mathbf{q}} <b|\nu>_{\mathbf{q}+\mathbf{k}} <\nu|c>_{\mathbf{q}+\mathbf{k}} <d|\mu>_{\mathbf{q}} f_{\mu}(\mathbf{q})[1 - f_{\nu}(\mathbf{q}+\mathbf{k})]. \tag{4.21}$$

From the expressions in Eqns. 4.20 and 4.21 it can be shown that $S_{TO} = S_{TB}$ and $S_{MO} = S_{MB}$ only if the orbitals do not hybridize to form the bands, i.e., the matrix elements are the elements of the identity matrix. In case of a nonzero hybridization, then the structure factors in the band and orbital representations are different.

4.3.2 d-model

Numerical Lanczos calculations for the homogeneous (or diagonal) magnetic structure factor S_{MO} have been shown in section 2.4 for the two-orbital d-model indicating a tendency towards magnetic colinear order for the undoped case, characterized by peaks at $\mathbf{k} = (\pi, 0)$ and $(0, \pi)$ in S_{MO}. This tendency is already apparent even in the non-interacting case as illustrated in panel (a) of Fig. 4.3 where S_{MO} calculated in a 16×16 cluster is shown with open circles, along the directions $(0,0) - (\pi, 0) - (\pi, \pi) - (0,0)$ in the unfolded BZ. The broad peak at $\mathbf{k} = (\pi, 0)$ is clear and it can be compared with the curve denoted by the star symbols in panel (b) of the same figure where results for the $\sqrt{8} \times \sqrt{8}$ cluster that can be studied numerically exactly (with the Lanczos algorithm and for any value of the Hubbard couplings) are presented. This same behavior is also apparent in the total orbital structure factor $S_{TO}(\mathbf{k})$ indicated by the diamonds in Fig. 4.3(a).

On the other hand, a calculation of the magnetic structure factor using the band representation, i.e. $S_{MB}(\mathbf{k})$ indicated by the squares in panel (a) of Fig. 4.3, shows a rather different behavior: instead of a clear peak at $(\pi, 0)$ there is a featureless plateau around $(\pi, 0)$ that extends to $(\pi/2, \pi/2)$. This example demonstrates the importance of the matrix elements in Eqn. 4.21 which differentiate between S_{MO} and S_{MB}. In the non-interacting case, both functions can be expressed in terms of the Fermi functions as in Eqns. 4.20 and 4.21 allowing us to conclude that the peak at $(\pi, 0)$ arises from the matrix elements rather than from purely nesting effects of the Fermi surfaces. Ignoring the matrix elements, it is interesting to note that a feature at $(\pi, 0)$ can also develop if all the components of the structure factor in the band representation are considered and $S_{TB}(\mathbf{k})$ is calculated, as shown by the curve indicated with triangles in Fig. 4.3(a).

The contribution of the band- and orbital-resolved components of the structure factor in the non-interacting case are presented in panel (a) of Fig. 4.4. The components of the structure factor that contribute to S_{MO} are S_{aabb} with a (b) taking

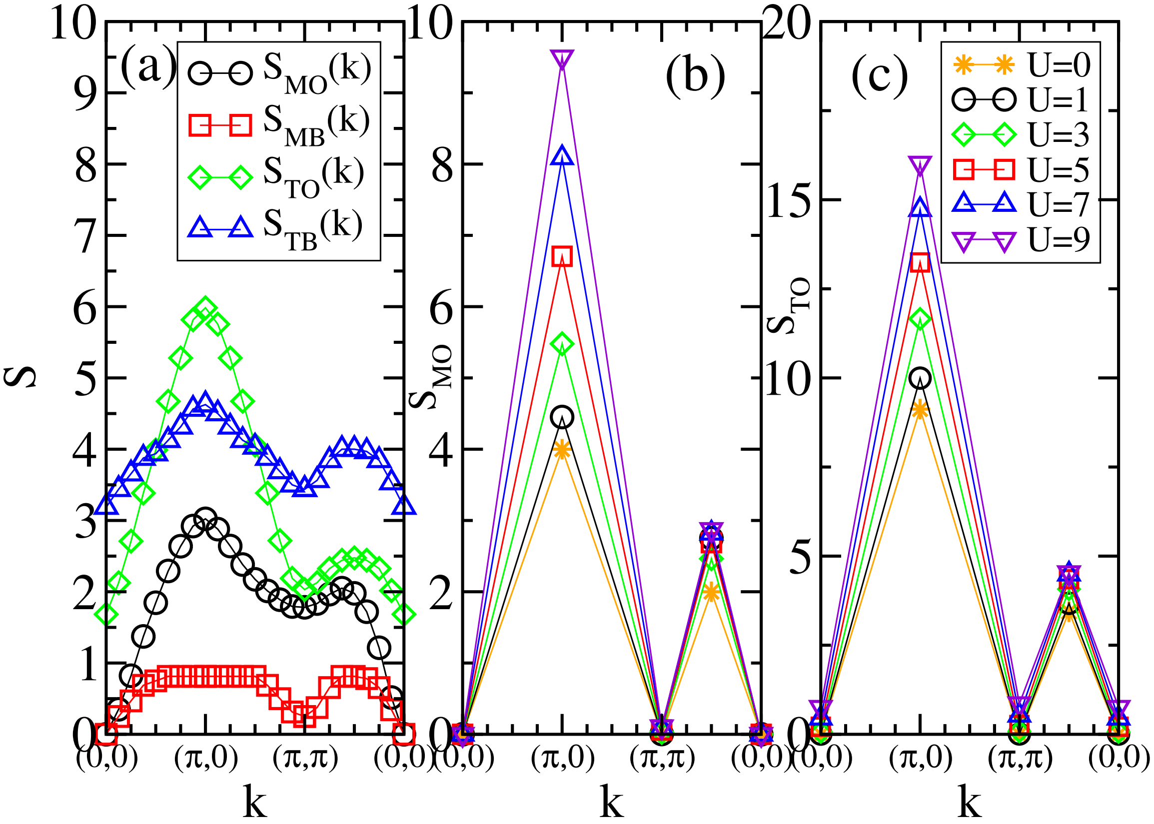

Figure 4.3: (a) Magnetic structure factors, total and homogeneous as indicated, for the non-interacting two-orbital d-model on a 16×16 lattice. (b) Homogeneous orbital magnetic structure factor $S_{MO}(\mathbf{k})$ for the interacting case with $J/U = 0.25$ and at the indicated values of U. The results were obtained numerically using an 8-sites cluster and the Lanczos method. (c) Total orbital magnetic structure factor $S_{TO}(\mathbf{k})$ for the interacting case, for the same parameters and technique as used in (b) [Nicholson et al. (2011b)].

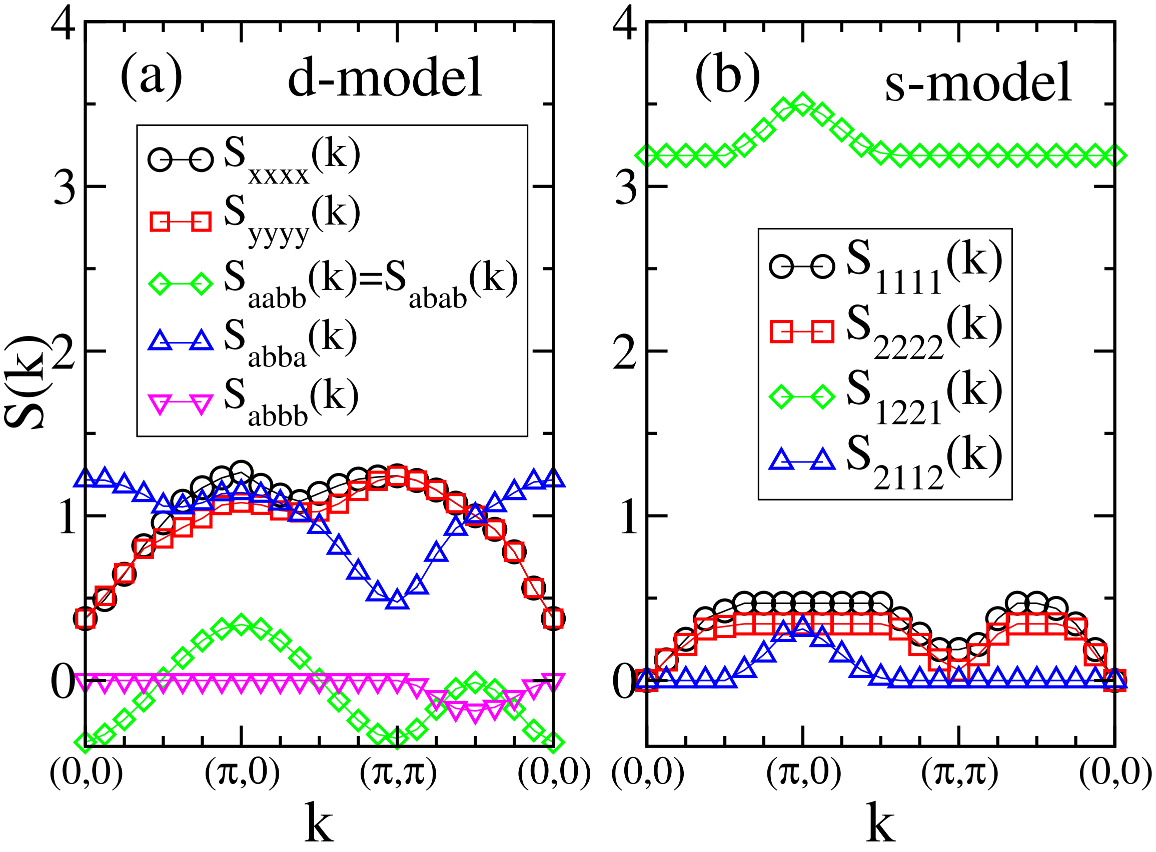

Figure 4.4: (a) Orbital-resolved components of the magnetic structure factor for the non-interacting two-orbital d-model on a 16 × 16 lattice. (b) Band/orbital resolved components of the magnetic structure factor for the non-interacting two-orbital s-model also on a 16 × 16 lattice. The index 1 (2) labels the lower (upper) band [Nicholson et al. (2011b)].

the values x (y) and y (x) indicated by the diamonds in the figure, and S_{aaaa} (indicated by the circles and squares). It is clear from the figure that the peak at $(\pi, 0)$ in S_{MO} at the non-interacting level is mostly due to the S_{aabb} that arise from the nesting of the two bands that contain the same orbital flavors due to hybridization, while the components of the form S_{aaaa} show features also at (π, π) since this wave vector also nests the hole (electron) FS's at Γ and M (X and Y). It can be seen that the non-homogeneous components of the form S_{abab} (diamonds) behave as S_{aabb} in the non-interacting case and contribute to form the peak at $(\pi, 0)$ in the total structure factor S_{TO} [triangles in Fig. 4.3(a)]. For completeness in Fig. 4.4(a) orbital resolved structure factors of the form S_{abba} (up triangles) and S_{abbb} (down triangles) are also shown; S_{abba} increase the value of S_{TO} at $(\pi, 0)$ while S_{abbb} provide a small negative contribution to S_{TO} along the diagonal direction of the BZ. Similar results were obtained for all the correlations in which three of the four indices are the same.

In non-interacting single-orbital systems, as studied for the cuprates, the spin and charge susceptibilities have the same form for all values of non-zero momenta, and any features in these functions arise from the nesting properties of the Fermi surface. Naively, the same is expected in the case of multi-orbital models but, as it will be discussed below, the hybridization of the orbitals plays a crucial role. In the d-model, the peaks in S_{MO} appear to be associated with the nesting of the hole- and electron-like Fermi surfaces. In the weak coupling picture, it is expected that magnetic order with $\mathbf{Q}$ equal to the nesting moments stabilizes when repulsive Coulomb interactions are added. Our Lanczos calculations for S_{MO} and S_{TO}, in panels (b) and (c) of Fig. 4.3, show that this is indeed the case.

The Lanczos calculated orbital magnetic structure factor $S_{MO}(\mathbf{k})$, using a $\sqrt{8} \times \sqrt{8}$ sites cluster, is shown in Fig. 4.3(b) for different values of U and at $J/U = 0.25$. This structure factor has a peak at $\mathbf{k} = (\pi, 0)$ (and $(0, \pi)$ as well, not shown) that becomes sharper as U increases, indicating a tendency towards robust magnetic order. Mean-field calculations based on these results, but extended to much larger systems, indicate that actual magnetic order develops at a finite value of U [Moreo et al. (2009b); Yu et al. (2009); Luo et al. (2010)].

The Lanczos-evaluated behavior of the $S_{MO}(\mathbf{k})$ peak at $\mathbf{k} = (\pi, 0)$, as a function of U, is shown in Fig. 4.5(a), for two different values of J/U (0.05 and 0.25). The tendency towards a robust magnetic state with increasing U and J/U is again clear.

As previously stated, S_{MO} is the magnetic structure factor calculated in the literature for comparison with experiments, but for completeness and for the sake of comparison with the s-model results, in panel (c) of Fig. 4.3, the Lanczos calculated values for the total generalized magnetic moment S_{TO} for the d-model as a function of U, for the case $J/U = 0.25$ are presented. It is clear that for the d-model S_{TO} mimics the behavior of S_{MO}. An important question to ask is what are the components of the orbital-resolved magnetic structure factor that drive the development of a peak at $\mathbf{Q} = (\pi, 0)$ (and $(0, \pi)$) when the Coulomb interactions are active. In Fig. 4.6 partial sums over selected components of the structure factor are shown with summations performed over repeated indices. In panel (a) of Fig. 4.6 it can be clearly observed that S_{aabb}, whose sum over a and b are indicated by the plus signs and the continuous lines in different shades for the different values of the interaction, are the components that drive that magnetic behavior. In fact, these are the homogeneous components that contribute to the physical magnetic structure factor S_{MO}. It is interesting to note that while $\sum_{a,b} S_{aabb}$ is equal to $\sum_{a,b} S_{abab}$ in the non-interacting system (panel (a) of Fig. 4.4) the partial sum of the non-homogeneous component $\sum_{a,b} S_{abab}$ [x symbols and dotted lines in Fig. 4.6(a)] does not increase with U at $\mathbf{Q}$ while the partial sum $\sum_{a,b} S_{aabb}$ clearly does.

4.3.3 s-model

Let us now carry out a similar analysis but for the two-orbital s-model defined by Eqn. 4.3. Since in this model each band is defined by a single orbital, then it is clear that $S_{MO} = S_{MB}$ and $S_{TO} = S_{TB}$.Note that studies based on fermiology

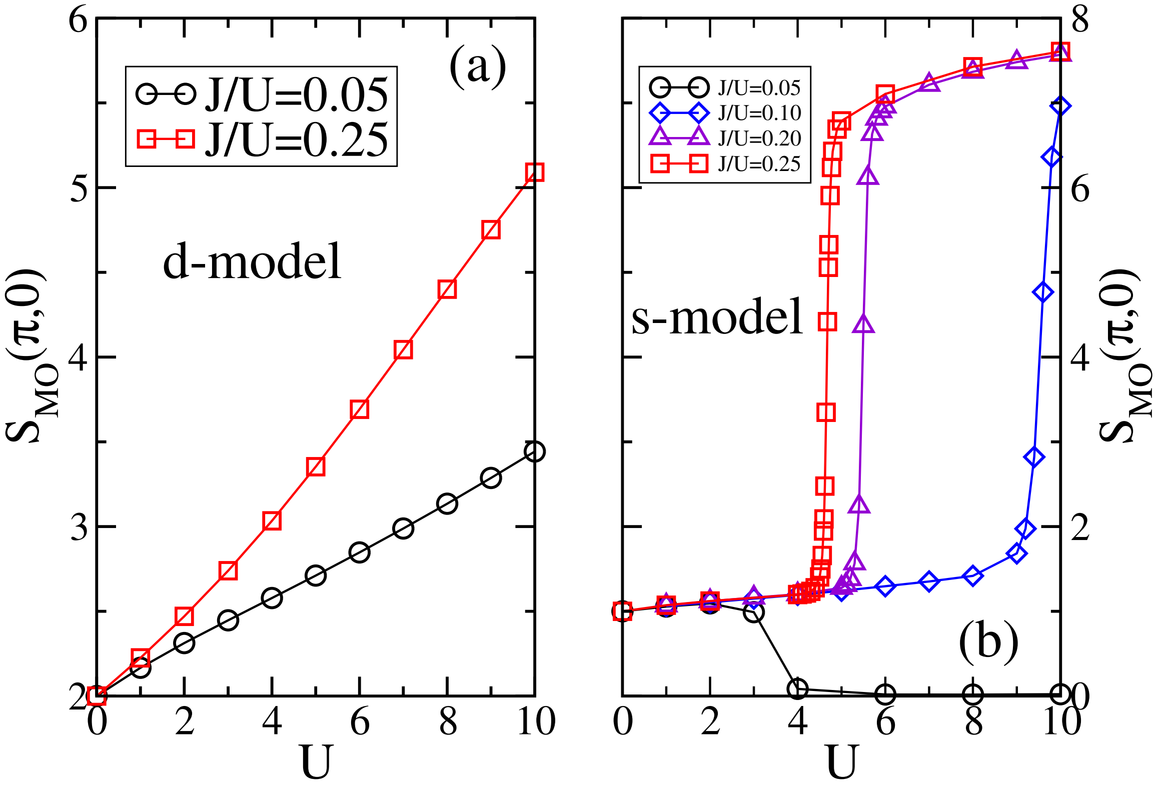

Figure 4.5: Orbital magnetic structure factor at wave vector $(\pi, 0)$ calculated numerically (Lanczos). (a) Results for the two-orbital *d*-model, as a function of the Coulomb repulsion U and for the values of J/U indicated. (b) Same as (a) but for the *s*-model [Nicholson et al. (2011b)].

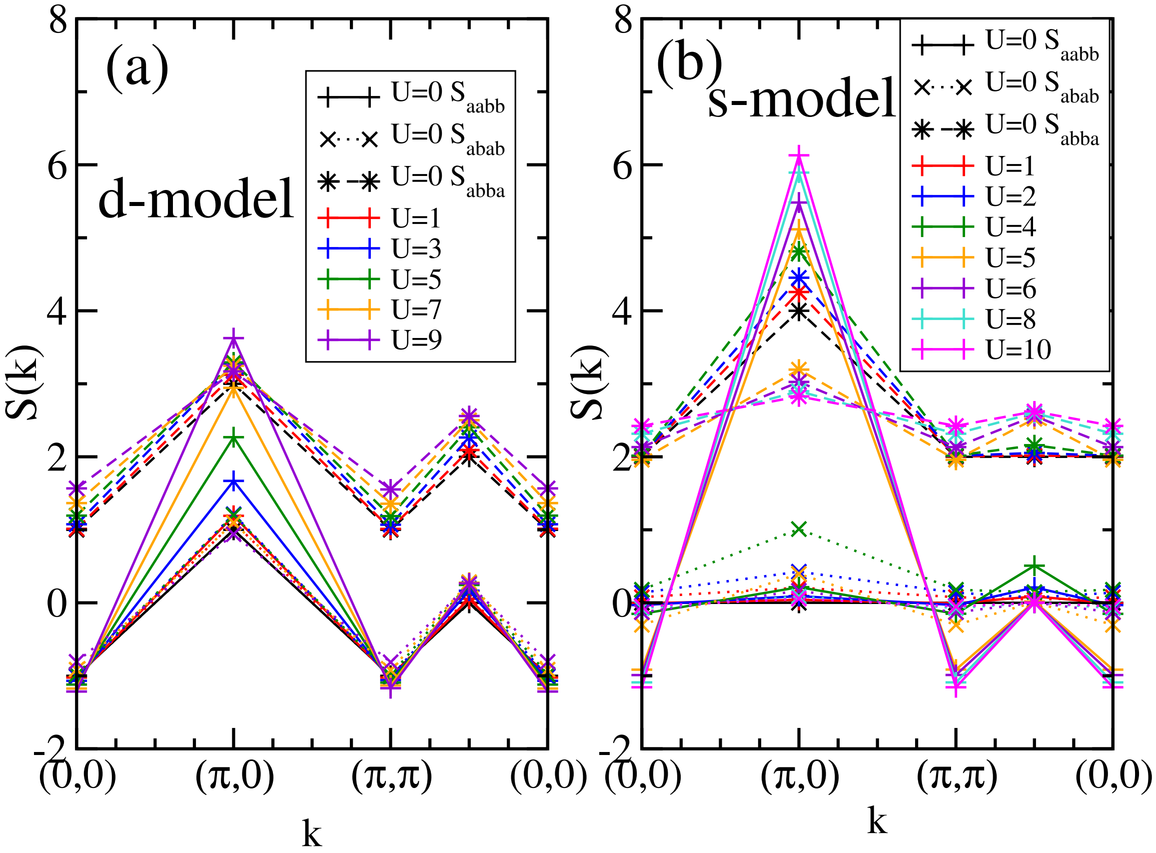

Figure 4.6: Orbital-resolved components of the total structure factor (sums over repeated indices are implied): S_{aabb} (plus, full line), S_{abab} (x, dotted line) and S_{abba} (star, dashed line), for the values of U indicated, obtained numerically (Lanczos) at $J/U = 0.25$ using an 8-sites cluster for (a) the d-model and (b) the s-model [Nicholson et al. (2011b)].

assume that if hole and electron FS's are nested via a momentum vector $\mathbf{Q}$, then spin density wave order will arise from a logarithmic instability that develops in the spin response at $\mathbf{Q}$ and is stabilized by the Coulomb interaction [Mazin et al. (2008); Chubukov et al. (2008)]. In this scenario the spin-density wave originates from the formation of particle-hole pairs, excitons, belonging to the electron and hole FS's (excitonic mechanism) [Chubukov et al. (2008)]. Our goal is to investigate whether this mechanism is valid for the s-model.

The magnetic structure factor S_{MO} in the non-interacting limit, denoted by the squares in panel (a) of Fig. 4.7, does not show the features expected from the nesting of the two Fermi surfaces at momentum $\mathbf{Q}$. The structure factor is actually rather flat on all the BZ, vanishing at $\mathbf{k} = (0, 0)$ and (π, π). These results are not what it would have been expected from the nesting properties.

Note that the results for S_{MO} in the non-interacting s-model [squares in Fig. 4.7(a)] are actually identical to the results for the homogeneous structure factor in the d-model in the band representation S_{MB} [indicated by squares in Fig. 4.3(a)], since both systems do have the same FS. However, note how different are the results for the d-model in the orbital representation [indicated by circles in Fig. 4.3(a)]. This is due to the effect of the matrix elements that result from the hybridization of the orbitals, which play a crucial role in the magnetic properties of the system. This effect can be more clearly appreciated when the interactions are added. The behavior of the peak in $S_{MO}(\mathbf{k})$ at $\mathbf{k} = (\pi, 0)$ was calculated with the Lanczos method applied to the s-model, by varying U and at different values of J/U using an $N = 8$ sites tilted cluster. In Fig. 4.5(b) it can be observed that for values of $J < 0.1U$ the peak in S_{MO} eventually vanishes. On the other hand, for $J \geq 0.1U$ a rapid increase in the peak's magnitude suddenly occurs at a value of U that decreases as J/U increases. The increase of the peak at $(\pi, 0)$ with increasing U is contrasted with the behavior of the feature at $(\pi/2, \pi/2)$ displayed in Fig. 4.7(b). Examination of the numerical (Lanczos) ground state indicates that at this point the Hubbard interaction is strong enough to hybridize the two bands and develop magnetic colinear order.

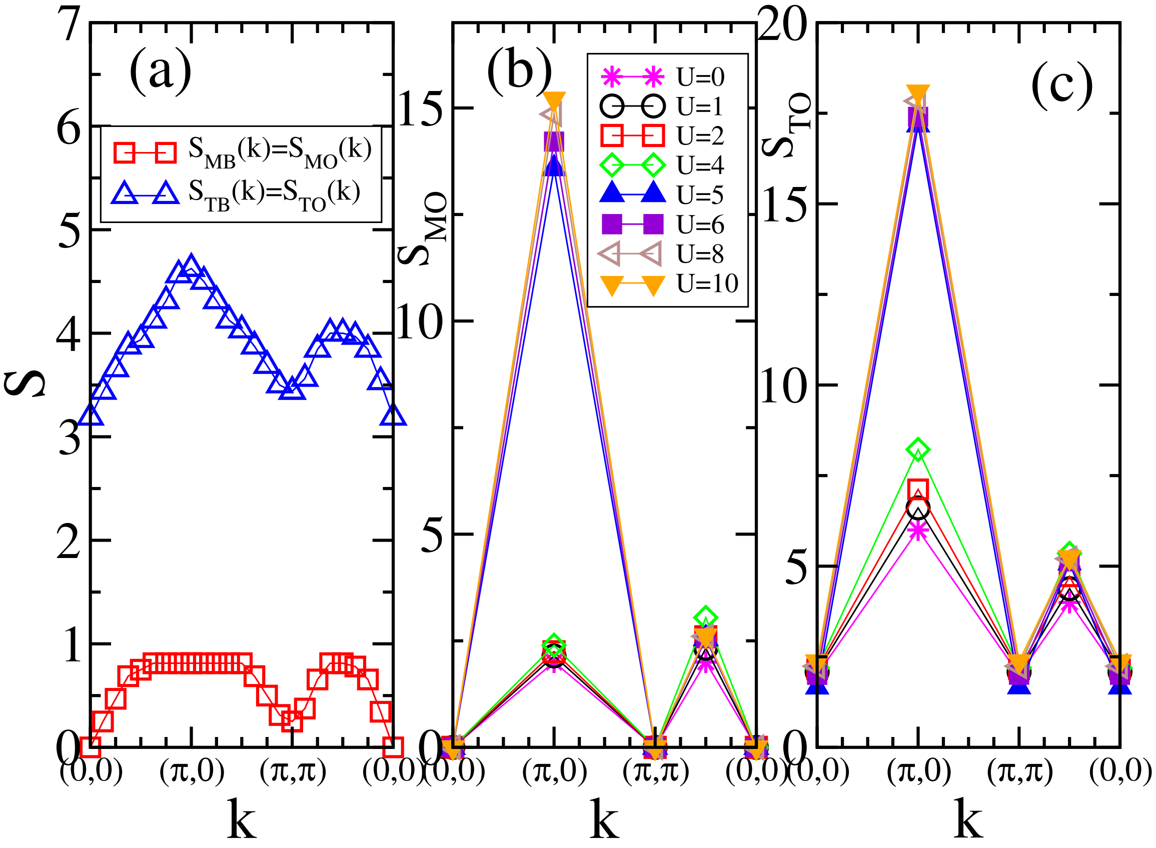

Figure 4.7: (a) Magnetic structure factors (total and homogeneous) as indicated for the non-interacting two-orbital *s*-model using a 16×16 lattice. (b) Homogeneous orbital/band magnetic structure factor $S_{MO}(\mathbf{k})$ for the interacting case with $J/U = 0.25$, at the indicated values of U. The results were obtained numerically via the Lanczos method using an 8-sites cluster. (c) Total orbital/band magnetic structure factor $S_{TO}(\mathbf{k})$ for the interacting case with the same parameters as in (b).

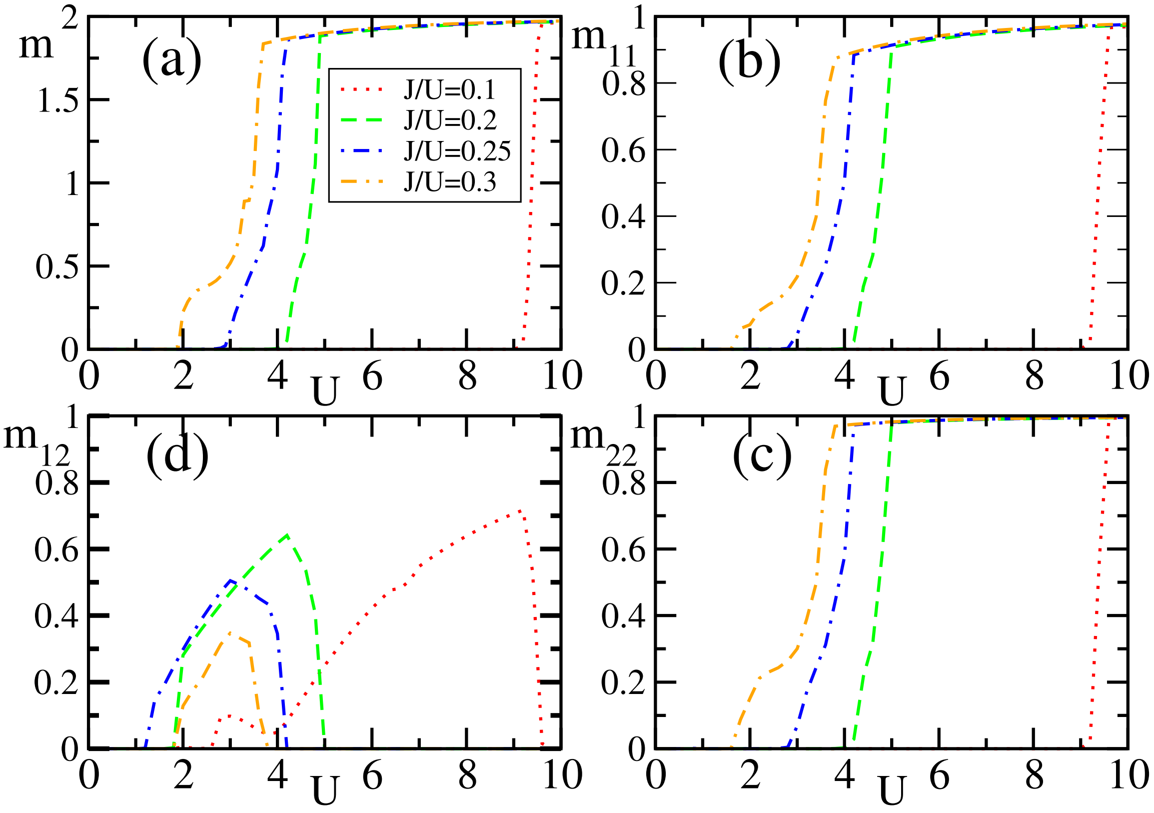

Figure 4.8: Mean-field calculated orbital/band resolved magnetic order parameters for the s-model, as a function of U and for the indicated values of J/U. (a) Total homogeneous magnetic order parameter $m = m_{11} + m_{22}$; (b) m_{11}; (c) m_{22}; (d) $m_{12} = m_{21}$.

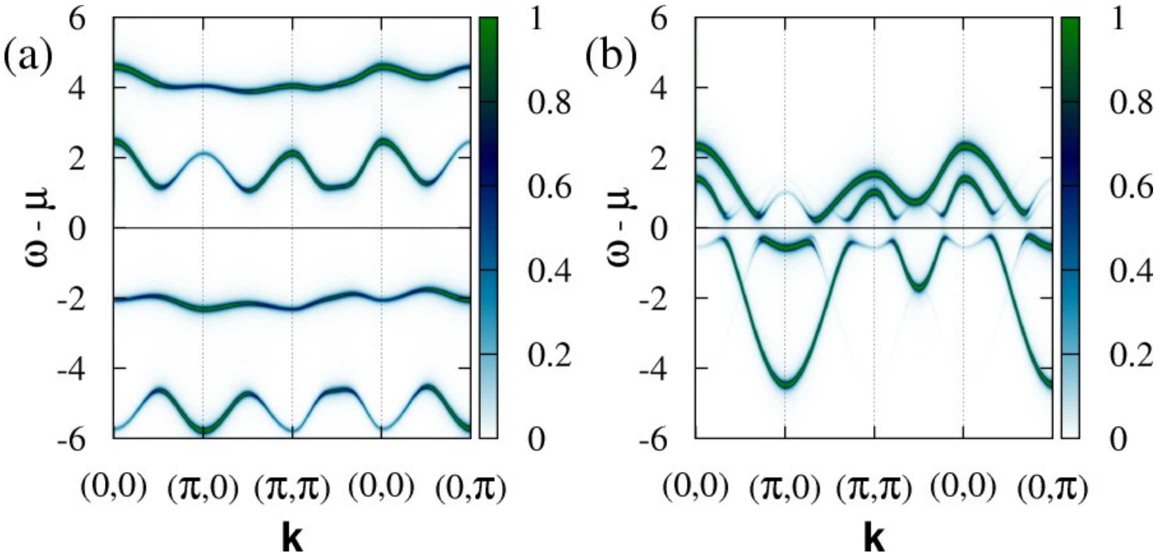

Figure 4.9: Intensity of the mean-field calculated spectral functions $A(\mathbf{k},\omega)$ as a function of $\omega - \mu$ and $\mathbf{k}$ for the s-model: (a) in the colinear magnetic phase for $U = 5$ and $J/U = 0.25$; (b) in the phase with orbital-transverse spin order for $U = 2.5$ and J/U=0.25 [Nicholson et al. (2011b)].

Based on the numerical results discussed above, a Hartree-Fock mean-field calculation was performed, following technical aspects already widely discussed in previous literature [Yu et al. (2009); Luo et al. (2010)]. By this procedure, it is clear that the total (homogeneous) magnetization m shown in panel (a) of Fig. 4.8 mimics the behavior of $S_{MO}(\pi, 0)$. Here, the transition to the magnetically ordered state is very rapid, resembling a first-order transition. The MF magnetic order develops only if $J \geq 0.1U$ which is in agreement with the Lanczos results shown in Fig. 4.5(b). The mean-field results also indicate that a full gap characterizes the magnetic state which is then an insulator as it can be seen from the MF calculated spectral functions $A(\mathbf{k}, \omega)$ displayed on panel (a) of Fig. 4.9. It is clear that the hybridization of the original bands/orbitals due to the Coulomb interaction is very strong and the band structure has been totally reconstructed. This behavior can be understood in the real-space representation. In order to develop magnetic colinear order in the half-filled system, it is necessary to have a net magnetic moment on each site. In the d-model, each orbital is half filled and thus contains a spin-1/2 that can easily be polarized by the interaction. In the *s*-model, on the other hand, the orbitals correspond to the bands, and one orbital is thus almost filled while the other is almost empty. Then, there are far fewer magnetic moments that can be polarized.

Thus, in the *s*-model the peak at $\mathbf{Q}$ in the magnetic structure factor does not develop from the nesting of the FS but from the Coulomb interaction, and it occurs fairly suddenly and at a robust value of $U \geq 4$ for the hopping parameters used here. Thus, while nesting appears to be a needed condition for the development of the peak in the magnetic structure factor, it is not a sufficient condition. The hybridization of the orbitals needs to be present such that the matrix elements allow the peak to emerge at sufficiently strong coupling. In fact, it is necessary that the bands that are connected by the nesting vector $\mathbf{Q}$ share the same orbital flavor. If this occurs via hybridization, magnetic order can develop at relatively weak coupling, but if this is not the case, the Coulomb interaction would induce magnetic order only in the strong coupling regime, as has been verified by studying the *s*-model. In this case, the magnetic transition is also a metal-insulator transition, as observed at least within the mean-field approximation. The *d*-orbital model, on the other hand, is known to display an intermediate metallic magnetic phase [Yu et al. (2009); Luo et al. (2010)]. Thus, the present results indicate that the *s* and *d* models develop similar magnetic behavior only in the strong coupling regime while in weak coupling, despite the nearly identical Fermi surfaces, both models have quite different ground states.

Orbital-transverse spin order

While the analysis of the results for the *s*-model presented above indicates that, despite the nesting of the electron and hole FS's, no magnetic order, as defined by the homogeneous operator, develops in weak coupling, it is instructive to analyze the behavior of the non-homogeneous components and the total magnetic structure factor S_{TO}. The non-interacting values of S_{TO} on a 16×16 lattice are indicated by the triangles in panel (a) of Fig. 4.7. There is a feature at $(\pi, 0)$ arising from the contribution of the inter-band components of the form $S_{abba} \equiv S_{\mu\nu\nu\mu}$, shown by the triangles and diamonds in panel (b) of Fig. 4.4. These are the components of S_{abcd} that contribute to the development of the maximum at $\mathbf{Q} = (\pi, 0)$ (and $(0, \pi)$) because the nesting at $\mathbf{Q}$ is between FS's defined by different bands. However, this type of terms are not part of the definition of the homogeneous structure factor S_{MB}. On the other hand, the components of the form S_{aaaa} indicated with circles and squares in Fig. 4.4(b), have a very flat shape in all the BZ and do not produce a sharp feature. Any other combination of orbital indices does not contribute to S_{TO} as shown in Eqn. 4.20.

The effect of the Coulomb interactions on the feature at $(\pi, 0)$ in S_{TO} has been obtained with Lanczos calculations and it can be seen in panel (c) of Fig. 4.7. The peak slowly increases as U raises from 0 to 4. Notice that for the same range of values of U the peak in S_{MO} shown in panel (b) of the figure does not change. The obvious question is whether this behavior indicates a novel kind of order in multi-orbital systems. The answer is provided via our MF approach that allows us to evaluate the components of the magnetization m_{ab}. The homogeneous magnetization m displayed in panel (a) of Fig. 4.8 is obtained as the sum of the intraorbital magnetizations m_{11} and m_{22} shown in panels (b) and (c) of the figure. Interestingly, the non-diagonal components $m_{12} = m_{21}$ develop finite values while the diagonal components are zero for values of $J/U > 0.1$ as shown in panel (d) of the figure. At the MF level the real space configuration associated to this finite order parameter can be studied. In the real space configuration the orbital spins are disordered, which is expected by the lack of features in $S_{MO}(\mathbf{k})$, but there are ordered generalized spins $\mathbf{G}_{ab}(\mathbf{i})$ defined as

$$\mathbf{G}_{ab}(\mathbf{i}) = d^{\dagger}_{\mathbf{i},a,\alpha} \vec{\sigma}_{\alpha,\beta} d_{\mathbf{i},b,\beta}, \tag{4.22}$$

where $\vec{\sigma}$ are the Pauli matrices and the orbital indices $a \neq b$. In Fig. 4.10 two configurations of $\mathbf{G}_{12}(\mathbf{i})$ that provide the MF ground state associated with the peak in S_{TO} at $(\pi, 0)$ (and $(0, \pi)$) when m_{12} is finite are shown. Panel (a) shows a flux configuration that generates peaks at $(\pi, 0)$ and $(0, \pi)$ in S_{TO} and panel (b) shows a colinear configuration that produces a peak at $(0, \pi)$. The peak at $(\pi, 0)$ is generated by a companion configuration rotated by $\pi/2$. Flux and colinear configurations have energies very close to each other and the actual ground state depends on the parameters [Eremin and Chubukov (2010)].

The new phase hinted at by the Lanczos calculations and stabilized in the MF calculations is insulating. The MF calculated spectral functions are shown in panel (b) of Fig. 4.9. A full gap has developed at the FS indicating that this order, if realized, would be observed with ARPES measurements. On the other hand, neutron scattering experiments would not detect it. This can be seen by performing a rotation in orbital space given by [Yao, Zi-Jian et al. (2011)]

$$d^{\dagger}_{\mathbf{i},\pm,\sigma} = \frac{1}{\sqrt{2}}(d^{\dagger}_{\mathbf{i},1,\sigma} \pm d^{\dagger}_{\mathbf{i},2,\sigma}). \tag{4.23}$$

In this new basis the schematic representations of the spins are shown in Fig. 4.11. It is clear that while the homogeneous spins in the orbitals + (black dots) and - (white dots) are ordered, the net spin at each site is 0 and thus, neutron scattering experiments will not detect the order because there is no finite local magnetization. These phases appear to be a realization of the orbital-transverse density-wave (OTDW) order proposed in [Yao, Zi-Jian et al. (2011).

Summarizing, a careful analysis of the small-cluster ground states obtained via Lanczos techniques, and with mean-field approximations in larger clusters, highlights the important role that the orbital composition plays in the development of magnetic order.

For the s-model, it is illuminating to consider the behavior of the total magnetic structure factor S_{TO}, see panel (c) of Fig. 4.7, calculated numerically as the interactions are increased. There is a weak increase of S_{TO} at $\mathbf{Q}$ before the sudden jump at $U = 4$. The behavior of the resolved components displayed in panel (b)

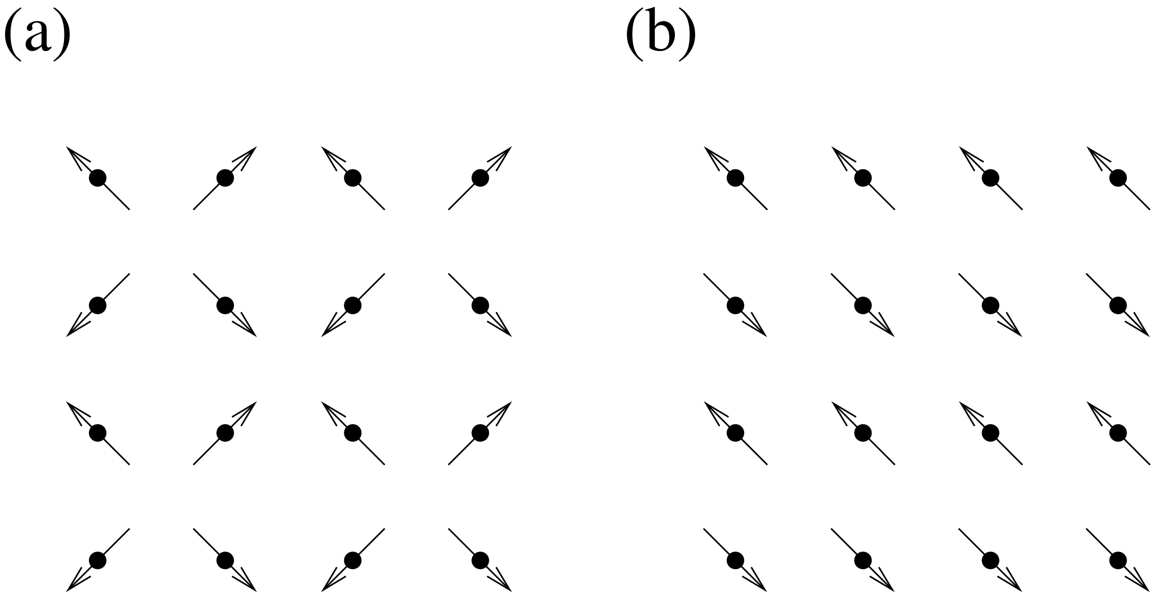

Figure 4.10: Schematic representation of the real space mean-field calculated ground states for the s-model when m_{12} is non-zero. (a) Flux phase; (b) Colinear phase. The dots indicate the sites and the arrows represent the MF value of the generalized spin $\mathbf{G}_{12}(\mathbf{i})$ defined in the text [Nicholson et al. (2011b)].

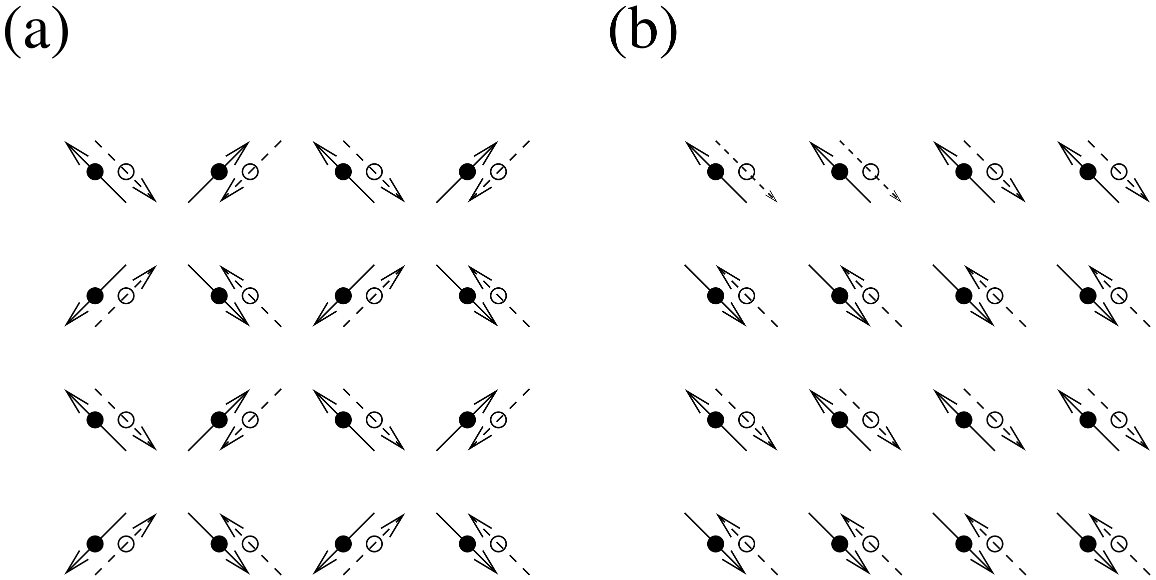

Figure 4.11: Schematic representation of the real space mean-field calculated ground states for the s-model when m_{12} is non-zero: (a) Flux phase; (b) Magnetic colinear phase. The black and white dots represent the orbitals + and - at each site and the continuous and dashed arrows represent the MF value of the spin at each orbital [Nicholson et al. (2011b)].

of Fig. 4.6 shows that for $0 \leq U \leq 4$ the partial sum over a and b of the non-homogeneous components S_{abab} (x symbols and dotted line) and S_{abba} (star symbols and dashed lines) increases in value at $(\pi, 0)$ indicating the stabilization of the orbital-transverse spin phase. For $U > 4$ a sudden increase of the sum of the homogeneous components S_{aabb} (plus symbols and continuous line) develops, the non-homogeneous components start to decrease and homogeneous magnetic order is established.

4.3.4 Weak Coupling: RPA Analysis

Additional insight into the weak coupling behavior of the d- and s-models can be obtained via the diagrammatic RPA method. Using this technique, the magnetic susceptibility $\chi_{abcd}(\mathbf{k}, i\omega)$ was calculated, [Graser et al. (2009); Kemper et al. (2010)] and the static structure factor was obtained by integrating the results over ω [Kariyado and Ogata (2009)]. In panel (a) of Fig. 4.12, the RPA-calculated diagonal or homogeneous structure factor for the d-model is presented. The non-interacting result (in agreement with the results indicated by the circles in panel (a) of Fig. 4.3) are denoted by the dashed line, while results at $U = 2.64$, the coupling strength where divergent behavior is about to occur for the case J/U=0.25, are indicated by the continuous line. In these results the peak at $(\pi, 0)$ is very prominent both with and without the Hubbard interaction on.

The same calculation performed for the s-model, presented in panel (b) of Fig. 4.12, gives rather different results. The flat behavior in the noninteracting case (dashed line), in agreement with the curve indicated by squares in Fig. 4.7(a), is replaced within RPA by a curve (continuous line) that develops weak features at incommensurate values of the momentum. Note that there were no precursors of these features in the non-interacting limit. Eventually the peak the closest to the Γ point along the diagonal direction of the BZ, indicated with an arrow in the figure, was found to diverge when U becomes larger than 2.67 for $J/U = 0.25$. This appears to be an illustration of a case in which RPA calculations indicate magnetic behavior that is unrelated to nesting properties. The RPA results show that an excitonic weak-coupling picture in which magnetic order characterized by the nesting momentum $\mathbf{Q}$ is expected to occur can be misleading if the orbital composition of the bands is not incorporated into the discussion. In the excitonic picture, the expectation is that the Coulomb interaction will allow the formation of electron-hole pairs with the electron (hole) in the electron (hole) Fermi surface. Since S_{MO} incorporates intraorbital electron-hole pairs, an RPA response requires that the nesting vector connects parts of the electron and hole bands that contain the *same* orbital flavor. This is the case in the d-model where even in the weak coupling regime the $(\pi, 0)$ magnetic-colinear state with two electrons with parallel spins at every site of the lattice has the largest weight in the ground state according to our Lanczos numerical studies. Since both orbitals are degenerate, the energetic penalization for populating both orbitals is U' and there is a gain given by J if both spins are parallel. As discussed before, in the s-model, on the other hand, the orbitals are non-degenerate and, thus, in addition to U' there is an energy Δ of penalization when two electrons are located in different orbitals at the same site. This energy can be larger than the gain obtained from J by having parallel spins or than the U penalization that arises from introducing both electrons in the same orbital. Then, a magnetic colinear state can only develop when U is comparable to the splitting Δ. This regime, which develops in strong coupling according to our Lanczos and MF calculations, is not captured by the weak-coupling RPA method. However, it will be shown that RPA is effective at finding the orbital-transverse spin state presented in the previous section if the generalized structure factor S_{TO} is calculated.

The values of S_{TO} obtained with RPA are presented in panels (c) and (d) of Fig. 4.12 for the d and s models, respectively. Both develop a peak at the nesting wavevector. The generalized structure factor takes into account electron-hole pairs formed by an electron and a hole in different bands that are allowed to have different orbital flavors. This is the reason why a peak develops now in both cases. While in the case of the d-model the behavior of S_{TO} mimics S_{MO} and the divergence in both

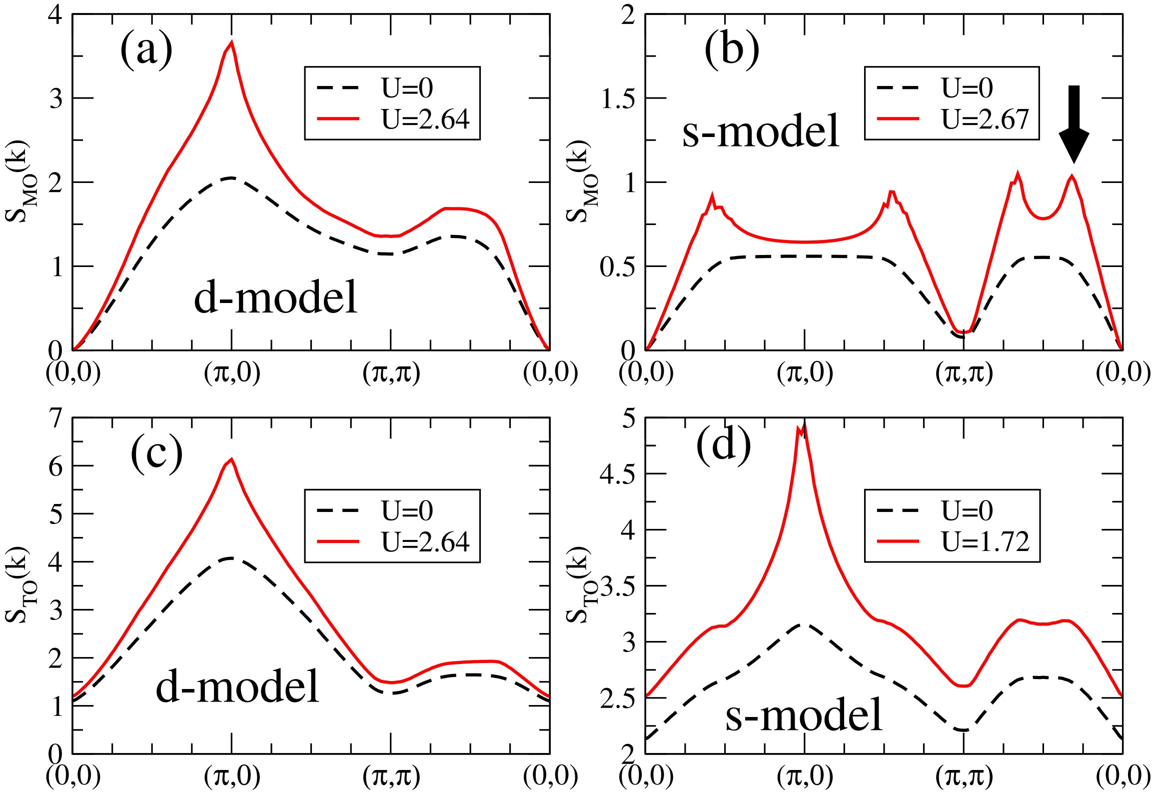

Figure 4.12: RPA calculated magnetic structure factors for $J/U = 0.25$, at the values of U indicated (full line). The non-interacting results are indicated with dashed lines. (a) Homogeneous magnetic structure factor in the *d*-model. (b) Same as (a), but for the *s*-model. The arrow indicates the peak that grows the most as the critical U is reached. (c) Generalized magnetic structure factor for the *d*-model. (d) Same as (c), but for the *s*-model [Nicholson et al. (2011b)].

occurs at the same value of U (slightly above 2.64 for $J/U = 0.25$) indicating that the colinear-magnetic order is the cause, in the s-model the peak in S_{TO} develops at a lower value of U ($U = 1.72$ for $J/U = 0.25$) and it results from the ordering revealed by the inhomogeneous components S_{1221} and S_{2112} of the structure factor, i.e., orbital-transverse spin order as discussed in the previous section. In this new light, the divergence in S_{MO} should be disregarded since it occurs for a much larger value of U than the divergence in S_{TO}. These results show that if all the elements of the susceptibility tensor are considered, RPA calculations are able to determine the development of new ordered phases that can develop in multi-orbital systems. Conversely, in multi-orbital systems in which orbital-transverse order develop, RPA calculations using only the homogeneous susceptibility may lead to unphysical results.

4.3.5 Strong Coupling Regime

In the regime where the coupling U is sufficiently strong such that even in the s-model it is energetically favorable to locate two electrons with parallel spins at the same site (and in different orbitals), both the s- and d-models can be mapped into effective $t - J - J'$ models and an insulating state with magnetic colinear order can occur. In this case the Hubbard repulsion has effectively hybridized both bands causing large distortions and actually opening a full gap [see Fig. 4.9(a)]. In this strong coupling regime both models appear to have similar properties, but an insulating magnetic behavior does not reproduce the experimental behavior observed in several of the undoped iron pnictides (such as the 1111 and 122 families). However, this regime could be applied to the chalcogenides: if U is sufficiently strong the magnetic behavior that develops in the strong coupling limit is more related to the hopping parameters and super-exchange than to the weak-coupling nesting properties of the Fermi surface. While the values of the hopping parameters in the Hamiltonian are crucial to achieve nesting in weak coupling [Brydon et al. (2011)], systems in which nesting is not perfect can develop colinear-like magnetic order if they map into a

$t-J-J'$ [Si and Abrahams (2008)] model in the strong coupling limit such as in the case of the three-orbital model for the pnictides [Daghofer et al. (2010)].

The results in this section indicate that in the case of the pnictides, even if the five d orbitals are considered, the xz and yz orbitals are the most likely to produce the strongest contribution to the metallic colinear magnetic order at weak or intermediate values of the Hubbard interaction because they are the major constituents of the FS's with better nesting and because they are degenerate and, thus, there is no energy Δ that needs to be overcome by the interaction. This is apparent already in the three-orbital model for the pnictides, where a mean-field calculation shows that magnetic order develops at a finite value of U (see panel (b) of Fig. 4.13) [Daghofer et al. (2010)]. In Fig. 4.13(a) it can be observed that the orbital with the best nesting associated with $\mathbf{Q}=(\pi,0)$ is the yz one, indicated by the continuous line. A mean-field calculation of the orbital resolved magnetization m_{aa} for a=xz, yz, and xy, shows that $m_{yz,yz}$ grows very rapidly at the lowest value of U. The magnetizations for the other orbitals develop as U hybridizes and distorts the original bands. Thus, in the intermediate U regime when magnetism develops, the xz and yz orbitals are the ones that would develop the stronger magnetization (albeit for different values of $\mathbf{Q}$) giving rise to a magnetic metallic phase. Thus, nesting seems to drive the magnetization of the xz/yz orbitals while the additional orbital hybridizations that develop due to the reconstruction of the FS then drives the smaller magnetization in the remaining orbitals.

4.4 Pairing Symmetries

Regarding the symmetry of the pairing operators corresponding to the models analyzed here, previous numerical calculations have indicated a competition between A_{1g}, B_{2g}, and E_g states in the d-model, see Chapters 2, and 3 or [Moreo et al. (2009b); Nicholson et al. (2011a)], as shown in panel (a) of Fig. 4.14. The E_g states correspond

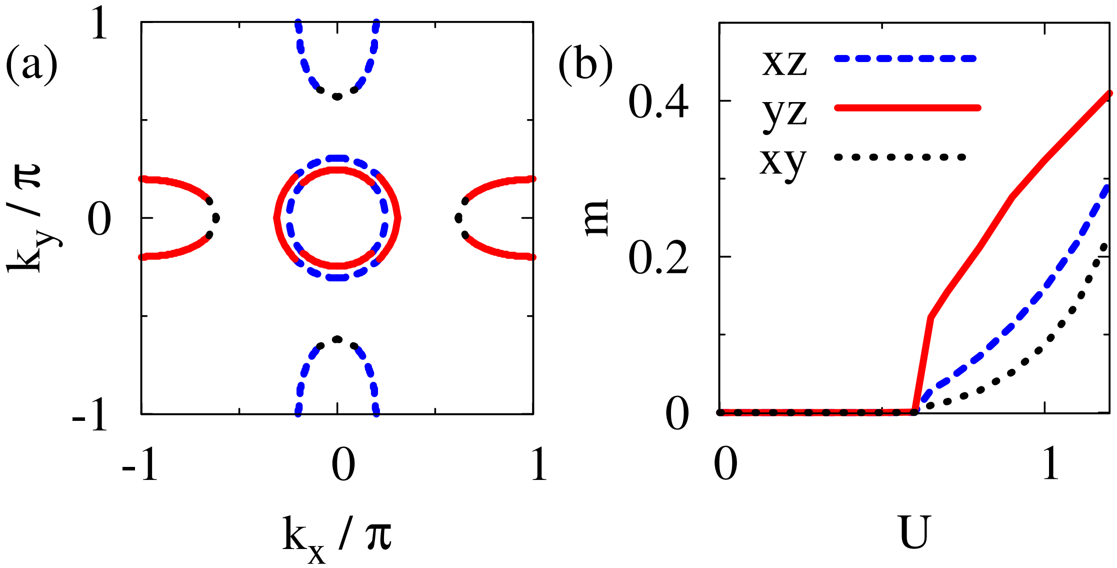

Figure 4.13: (a) Fermi surface with its orbital composition for the case of a three-orbital model for the pnictides. (b) Mean-field calculated orbital-resolved magnetization for the same three-orbital model. The figure was taken from [Daghofer et al. (2010)] for illustration.

to a p-wave spin-triplet state that becomes destabilized upon the addition of binding-enhancing Heisenberg terms [Nicholson et al. (2011a)]. The favored pairing operators with the symmetry A_{1g} are all trivial in their orbital composition, i.e. they are intraorbital with the form $D^\dagger\sigma_0 D$ where $D^\dagger = (d^\dagger_{\mathbf{k},x,\uparrow}, d^\dagger_{-\mathbf{k},y,\downarrow})$ in the (x, y) basis, and they remain intraorbital in the (X, Y) basis. However, the B_{2g} pairing operators have a non-trivial orbital composition given by $D^\dagger\sigma_1 D$ in the basis (x, y), indicating that the pairs are made of electrons in the two different orbitals. In the (X, Y) basis the B_{2g} pairing operator becomes $D'^\dagger\sigma_3 D'$ with $D'^\dagger = (d^\dagger_{\mathbf{k},X,\uparrow}, d^\dagger_{-\mathbf{k},Y,\downarrow})$. Thus, in the (X, Y) representation the B_{2g} pairs are intraorbital but there is an important sign difference between the pairs in the different orbitals which makes the orbital contribution intraorbital but non trivial. It is interesting to observe that the intraorbital B_{1g} state found with RPA calculations in the five-orbital model for the pnictides [Graser et al. (2009)] would become interorbital in the (X, Y) basis.

The results for the s-model regarding pairing properties are different from those in the d-model. Using the Lanczos method the relative symmetry was calculated between the undoped (number of electrons $N_e = 16$) and electron-doped ($N_e = 18$) states, as an indicator of the possible pairing symmetry in the bulk limit. The results are presented in panel (b) of Fig. 4.14, varying U and J/U. For small values of U and J/U the doped ground state has symmetry A_{1g} in agreement with the d-model, although in a different regime of couplings. Increasing U and J/U, the s-model ground state switches to the E_g symmetry, i.e. p-wave. This p-symmetry arises from the spatial location of the electrons since the orbital contribution is trivial. In the small cluster studied here the spin-triplet state with $\mathbf{k} = (0, 0)$ is almost degenerate with a spin-singlet state with $\mathbf{k} = (\pi, \pi)$. The possibility of having a spin-singlet p-wave state with wavevector $\mathbf{k} = (\pi, \pi)$ has been previously discussed long ago in the context of the single-orbital Hubbard model [Scalettar et al. (1991)]. In the present case, $\mathbf{k}$ is a pseudo-momentum and in the folded representation $\mathbf{k} = (\pi, \pi)$ actually maps into $(0, 0)$ so that the actual Cooper pair, if stabilized, has zero center-of-mass momentum, but the components of the pair belong to bonding and anti-bonding

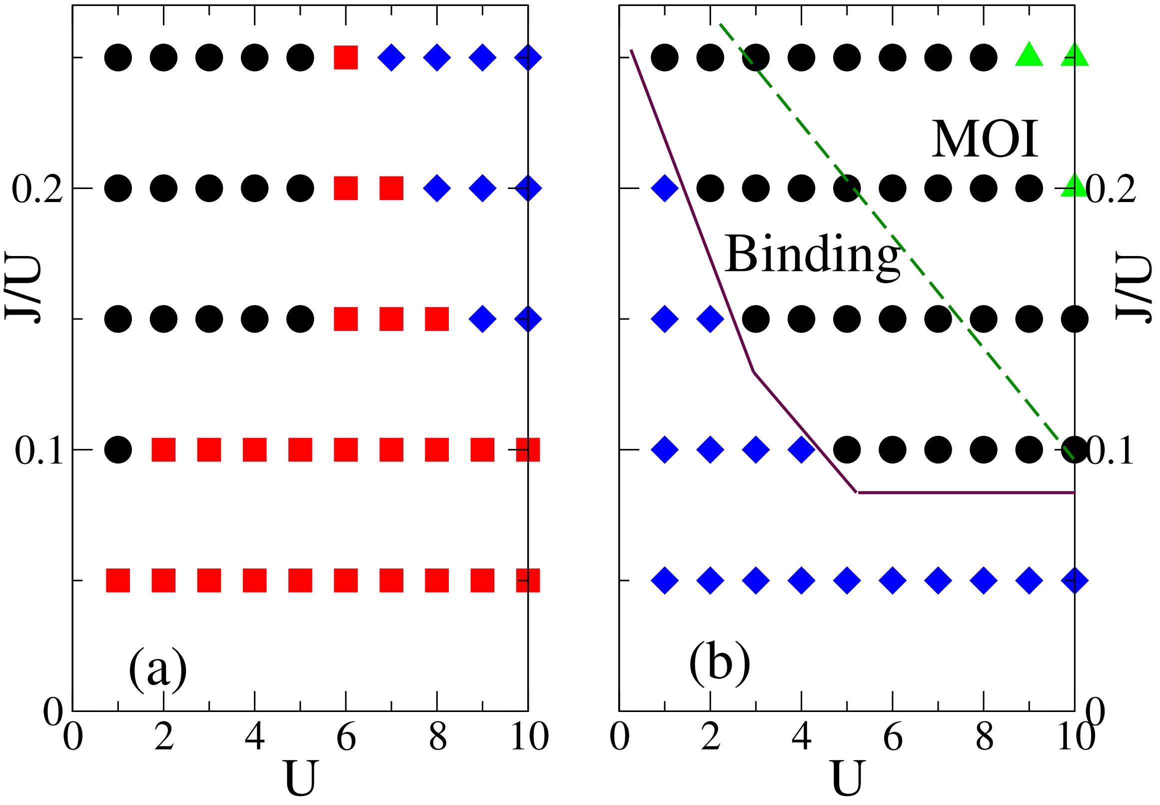

Figure 4.14: (a) Relative symmetry between the undoped and the electron-doped ground states for the case of the d-orbital model, varying J/U and U. The results were obtained numerically via the Lanczos method using a small cluster with $N = 8$ sites (and following steps already discussed in the previous Chapters 2 and 3) [Daghofer et al. (2008); Nicholson et al. (2011a)]. The circles indicate states with E_g symmetry, squares correspond to B_{2g}, and diamonds represent A_{1g} symmetric states. (b) Same as (a) but for the s-model with the triangles denoting B_{1g} symmetry. In the region above the continuous line the two added electrons form a bound state. The dashed line indicates the boundary for the stability of the magnetically ordered insulating (MOI) region in the undoped state [Nicholson et al. (2011b)].

bands that could become hybridized for the large values of the interactions needed to stabilized these states. As indicated in the figure, it was also found that the *p*-states show binding in the small system studied here. In addition a small region of bound states with B_{1g} symmetry is found at even larger couplings. While in the *d*-model our numerical results indicate that the orbital degree of freedom plays a crucial role in the symmetry of the pairing states, this is not the case in the *s*-model. This result seems to indicate that interorbital Cooper pairs are likely to be present in multi-orbital systems with strongly hybridized bands as is the case in the pnictides.

Understanding more deeply why the *s*-model develops its particular pairing properties is at this point unnecessary since the model simply provides an illustration of a system with a similar FS as the *d*-model, and the goal of this work was to show that the orbital composition of the bands plays a crucial role in determining the symmetry of the doped states. The examples that have been discussed here clearly show that models with the same Fermi surface and the same interactions can have very different pairing properties depending on the degree of hybridization of the orbitals. It also seems, according to the present results, that the relevance of the orbital degree of freedom in determining the pairing symmetry is influenced by the degree of hybridization among those orbitals.

4.5 Conclusions

Summarizing, numerical and analytical calculations have been performed in order to compare the properties of two band models with identical FS's and interactions, but differing in the degree of hybridization of the orbitals to form the bands. Despite the nesting properties of the FS's it was discovered that both models have similar magnetic (insulating) ground states in the strong coupling limit, but they are very different in weak and intermediate coupling. The *s*-model offers an example in which, despite the nesting of the FS and the presence of Coulomb interactions, magnetism does not develop in weak coupling. However, it was discovered that instead, as a result of the nesting in weak coupling, the Coulomb interaction stabilizes an orbital-transverse spin ordered state with no local magnetization. This state is insulating and is characterized by a gap that could be observed in ARPES experiments. However, due to the lack of local magnetization, neutron scattering experiments would not detect the development of "generalized spin order". In fact, standard RPA calculations in the s-model lead to incorrect results such as incommensurate magnetic order in the physical homogeneous channel. However, when the non-homogeneous components of the susceptibility are taken into account, RPA reveals the existence of the orbital-transverse spin phase for values of U lower than the ones needed to observe the unphysical magnetic state.

It is clear that the physical (homogeneous) magnetic structure factor depends strongly on the orbital flavor of the bands and for this quantity to develop a peak in weak coupling it is necessary that the portions of the FS connected by nesting have the same orbital flavor.

The possibility of "hidden" magnetic ordering in the pnictides has been proposed by several authors [Rodriguez and Rezayi (2009); Cricchio et al. (2010); Bascones et al. (2010)] as an explanation for the unexpectedly low value of the magnetization in several of these materials. The hidden order proposed by these authors was "diagonal", as the configurations presented in Fig. 4.11 after transforming our non-diagonal results into a rotated orbital basis. However, in multi-orbital systems with more than two orbitals, it may be necessary to consider the non-diagonal order as well. In theoretical and analytical calculations these non-diagonal hidden orders are revealed by considering all the components, homogeneous and inhomogeneous, of the magnetic susceptibility. On the experimental side, ARPES can detect gaps that are opened due to the "hidden" magnetic order but the traditionally used techniques to detect homogeneous magnetic order, such as neutron scattering, will fail due to the lack of a local magnetization.

Indications of quenching of the orbital degree of freedom in systems with non-hybridized orbitals were also found. The orbitals do not appear to play a role in determining the symmetry of the pairing states. This degree of freedom, though, is crucial in systems with hybridized orbitals. In the case of the pnictides in particular, this thesis shows the ground states with d symmetry found in the literature in models for the pnictides, such as the B_{1g}, can be made interorbital by changing the basis in which the degenerate xz and yz orbitals are defined.

The results provided by this work may explain why the end member of the series $BaFe_2(As_{1-x}P_x)_2$ is non-superconducting despite displaying the best nesting of all the compounds in the series [Arnold et al. (2011)]. If superconductivity necessitates magnetic fluctuations they may not be sufficiently strong in this compound if there is no good matching between the flavor of the orbitals in the nested bands.

Finally, our results confirm the perception expressed in the analysis of recent photoemission experiments [Shimojima et al. (2010)] that the weak coupling nesting mechanism would not be applicable if indeed a hole-pocket band dominated by the orbital $3z^2 - r^2$ (with no nesting partner in the electron-pocket band) does develop a robust superconducting gap. Confirming and then understanding the results of those recent photoemission experiments is indeed very important for the clarification of several intriguing issues in the challenging physics of the pnictides.

Chapter 5

Three Orbital Model

Even though numerical calculations on the two orbital model, as seen in Chapters 2, 3, and 4, indicate that the magnetic metallic regime, observed experimentally in undoped compounds [Dong et al. (2008); de la Cruz et al. (2008); Chen et al. (2008d); Krellner et al. (2008); Goldman et al. (2008)] is stabilized for intermediate values of Coulomb repulsion U several authors have claimed that using two orbitals may miss important features of the real system [Lebegue (2007); Xu et al. (2008); Cao et al. (2008); Zhang et al. (2009); Lee and Wen (2008)]. It has been argued that a minimal model for the pnictides should contain at least three orbitals for two main reasons *(i)* A relatively small portion of the electron-pocket FS of LaOFeAs is determined by a band of mostly d_{xy} character and *(ii)* the bands that produce the two hole pockets should be degenerate at the center of the Brillouin zone (BZ), which is not the case when only two orbitals are considered. The important question is how much these shortcomings of the two orbital model impact the most relevant properties of the pnictides. The aim of this paper is to construct a three-orbital model that addresses these concerns and compare its properties with the two-orbital case. This is important because in other areas of condensed matter physics, such as the manganites, a simple single-orbital model is often sufficient to capture qualitatively the phenomenon of colossal magnetoresistance [Dagotto et al. (2001)], while clearly a two-orbital model is still necessary to properly describe additional properties such as the magnetic and orbital order observed in these materials.

This Chapter is organized as follows. In Section 5.1 the three orbital model is introduced in both real space and momentum space representations, followed by a mean field studies of the model's magnetic properties in Section 5.2 and preferred pairing symmetries in Section 5.3.

5.1 The Model

Following the methods described for the two orbital model, in Section 2.2, a tight binding Hamiltonian can be derived in real space [Daghofer et al. (2010)]:

$$\begin{aligned}
H_{TB}^{xz,yz,xy} &= H_{TB}^{xz,yz} \\
&+ t_5 \sum_{\mathbf{i},\hat{\mu},\sigma} (d^\dagger_{\mathbf{i},xy,\sigma} d_{\mathbf{i}+\hat{\mu},xy,\sigma} + h.c) - t_6 \sum_{\mathbf{i},\hat{\mu},\hat{\nu},\sigma} (d^\dagger_{\mathbf{i},xy,\sigma} d_{\mathbf{i}+\hat{\mu}+\hat{\nu},xy,\sigma} + h.c) \\
&- t_7 \sum_{\mathbf{i},\sigma} (-1)^{|i|} (d^\dagger_{\mathbf{i},xz,\sigma} d_{\mathbf{i}+\hat{x},xy,\sigma} + h.c) - t_7 \sum_{\mathbf{i},\sigma} (-1)^{|i|} (d^\dagger_{\mathbf{i},xy,\sigma} d_{\mathbf{i}+\hat{x},xz,\sigma} + h.c) \\
&- t_7 \sum_{\mathbf{i},\sigma} (-1)^{|i|} (d^\dagger_{\mathbf{i},yz,\sigma} d_{\mathbf{i}+\hat{y},xy,\sigma} + h.c) - t_7 \sum_{\mathbf{i},\sigma} (-1)^{|i|} (d^\dagger_{\mathbf{i},xy,\sigma} d_{\mathbf{i}+\hat{y},yz,\sigma} + h.c) \\
&- t_8 \sum_{\mathbf{i},\sigma} (-1)^{|i|} (d^\dagger_{\mathbf{i},xz,\sigma} d_{\mathbf{i}+\hat{x}+\hat{y},xy,\sigma} + h.c) + t_8 \sum_{\mathbf{i},\sigma} (-1)^{|i|} (d^\dagger_{\mathbf{i},xy,\sigma} d_{\mathbf{i}+\hat{x}+\hat{y},xz,\sigma} + h.c) \\
&- t_8 \sum_{\mathbf{i},\sigma} (-1)^{|i|} (d^\dagger_{\mathbf{i},xz,\sigma} d_{\mathbf{i}+\hat{x}-\hat{y},xy,\sigma} + h.c) + t_8 \sum_{\mathbf{i},\sigma} (-1)^{|i|} (d^\dagger_{\mathbf{i},xy,\sigma} d_{\mathbf{i}+\hat{x}-\hat{y},xz,\sigma} + h.c) \\
&- t_8 \sum_{\mathbf{i},\sigma} (-1)^{|i|} (d^\dagger_{\mathbf{i},yz,\sigma} d_{\mathbf{i}+\hat{x}+\hat{y},xy,\sigma} + h.c) + t_8 \sum_{\mathbf{i},\sigma} (-1)^{|i|} (d^\dagger_{\mathbf{i},xy,\sigma} d_{\mathbf{i}+\hat{x}+\hat{y},yz,\sigma} + h.c) \\
&- t_8 \sum_{\mathbf{i},\sigma} (-1)^{|i|} (d^\dagger_{\mathbf{i},yz,\sigma} d_{\mathbf{i}+\hat{x}-\hat{y},xy,\sigma} + h.c) + t_8 \sum_{\mathbf{i},\sigma} (-1)^{|i|} (d^\dagger_{\mathbf{i},xy,\sigma} d_{\mathbf{i}+\hat{x}-\hat{y},yz,\sigma} + h.c) \\
&+ \Delta_{xy} \sum_{\mathbf{i}} n_{\mathbf{i},xy} \qquad (5.1)
\end{aligned}$$

where $H_{TB}^{xz,yz}$ is given by Eqn. (2.20) and Δ_{xy} is the energy difference between Fe

Table 5.1: Hopping parameters used in the three orbital model [Daghofer et al. (2010)].

t_1	0.02
t_2	0.06
t_3	0.03
t_4	-0.01
t_5	0.2
t_6	0.3
t_7	-0.2
t_8	$-t_7/2$
Δ_{xy}	0.4

d_{xz}, d_{yz} and d_{xy} orbitals. The second line of Eqn. (5.1) gives NN intraorbital d_{xy}-d_{xy} hoppings with amplitude t_5, while the third line gives NNN hoppings with amplitude t_6. The fourth through the seventh lines give NN interorbital d_{xy}-d_{xz}/d_{yz} with hopping amplitude t_7. The last lines give NNN interorbital hoppings with hopping amplitude t_8. Note that the factors $(-1)^{|i|}$ arise from the alternating As above/below the Fe-As plane which adds a phase to the overlaps between the Fe d$_{xy}$ and As p orbitals. The hopping parameters t_i are determined, as in the two orbital model, by fitting the band dispersion to band structure calculations (Table 5.1).

The tight binding Hamiltonian in Eqn. (5.1) can be transformed to momentum space via the same Fourier transform shown in Eqn. 2.22. Again, it is important to remember that since the tight binding Hamiltonian was constructed in a unit cell with only one Fe atom per unit cell, the Fourier transformed Hamiltonian is defined in the extended or unfolded BZ (see Section 2.2). The real space tight binding Hamiltonian is invariant under translation in the $\hat{x}$ or $\hat{y}$ directions followed by a reflection about the x-y plane. When the eigenstates of the Hamiltonian are labeled in terms of the eigenvalues of these symmetry operations, then the momentum-space Hamiltonian can be expressed in terms of a pseudo-crystal momentum, **k**, that expands the unfolded BZ that corresponds to a single Fe atom per unit cell in real space. Folding the extended BZ gives the reduced BZ that corresponds to two Fe atoms per unit cell

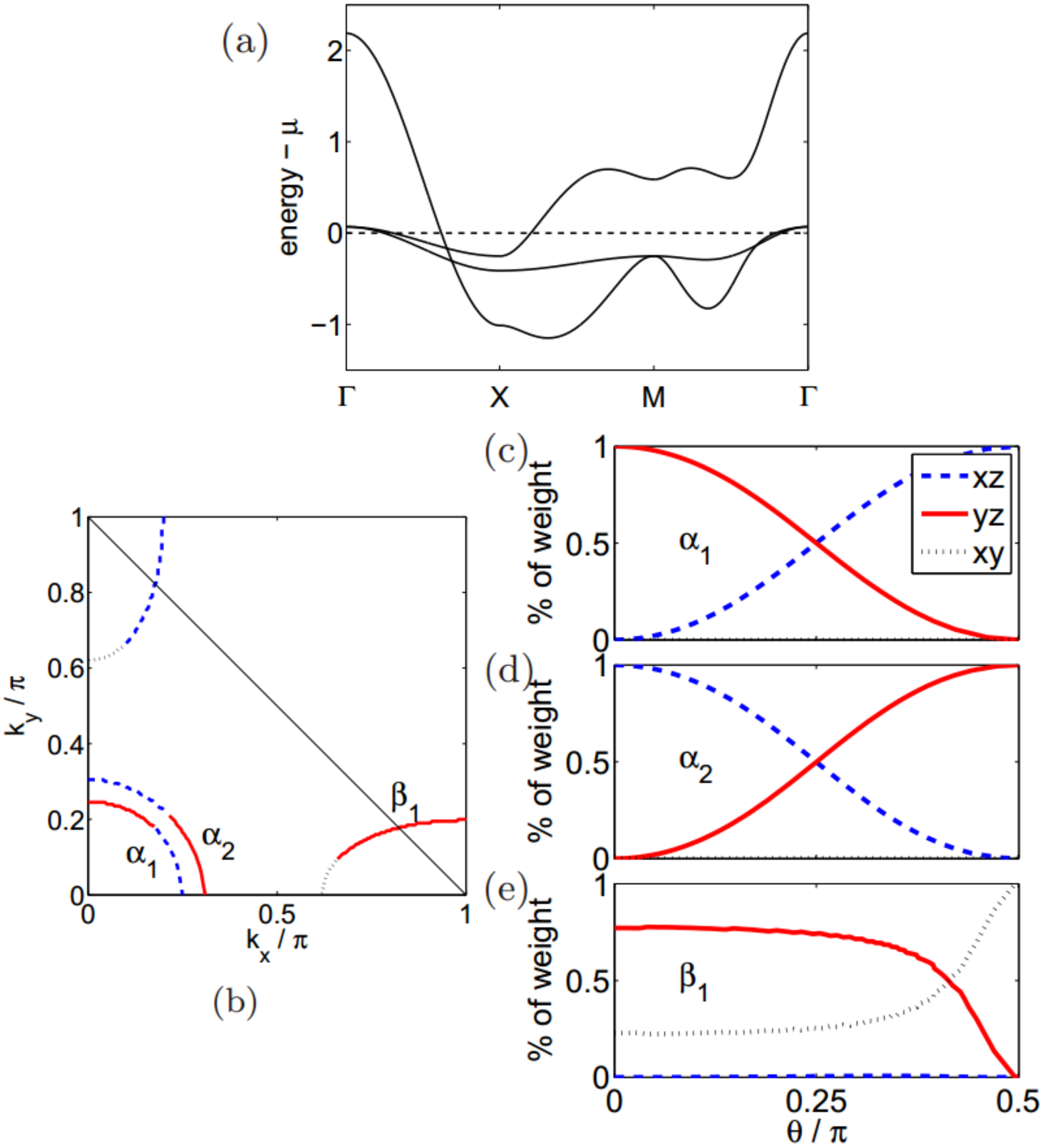

Figure 5.1: (a) Band structure and (b) Fermi surface of the tight-binding (i.e. non-interacting) three-orbital model, with parameters from Tab. 5.1 and in the unfolded BZ. The diagonal thin solid line in (b) indicates the boundary of the folded BZ. In panels (c-e), the orbital contributions to the two hole and one of the electron pockets are given. The winding angle θ is measured with respect to the k_y-axis. The second electron pocket is analogous to the one shown simply replacing xz by yz. In all panels, the dashed lines refer to the xz orbital, the solid to yz, and the dotted to xy [Daghofer et al. (2010)].

and thus the number of bands is doubled to six since now there are three orbitals for each of the two Fe ions per unit cell.

In momentum space, the tight binding Hamiltonian becomes:

$$H_{TB}(\mathbf{k}) = \sum_{\mathbf{k},\sigma,\mu,\nu} (T^{\mu,\nu}(\mathbf{k}) - \mu) d^{\dagger}_{\mathbf{k},\mu,\sigma} d_{\mathbf{k},\nu,\sigma} \tag{5.2}$$

with

$$T^{11} = 2t_2 cosk_x + 2t_1 cosk_y + 4t_3 cosk_x cosk_y \tag{5.3}$$

$$T^{22} = 2t_1 cosk_x + 2t_2 cosk_y + 4t_3 cosk_x cosk_y \tag{5.4}$$

$$T^{33} = 2t_5(cosk_x + cosk_y) + 4t_6 cosk_x cosk_y + \Delta_{xy} \tag{5.5}$$

$$T^{12} = T^{21} = 4t_4 sink_x sink_y \tag{5.6}$$

$$T^{13} = \bar{T}^{31} = 2it_7 sink_x + 4it_8 sink_x cosk_y \tag{5.7}$$

$$T^{23} = \bar{T}^{32} = 2it_7 sink_y + 4it_8 sink_y cosk_x \tag{5.8}$$

where the bar on the top of a matrix element denotes the complex conjugate and Δ_{xy} is the splitting of the d_{xy} orbital from the d_{xz}/d_{yz} orbitals. One important issue that needs to be addressed is the electronic filling in the three orbital model. In the two orbital model half filling is considered to be the correct electronic density, since the $x^2 - y^2$ and $3z^2 - r^2$ orbitals are assumed to be fully occupied with four of the six Fe valence electrons and the xy orbital is assumed to be empty, leaving two electrons for the xz and yz orbitals. Applying the crystal field splitting rationale to the three orbital model with xz, yz, and xy orbitals this argument leads to a filling of one third (two electrons in three orbitals) [Krüger et al. (2009)]. However, for such a filling the shape of the FS given by LDA cannot be reproduced. In fact, band-structure calculations suggest that the three orbital system should be *more* than half-filled and actually have a filling of roughly two thirds (four electrons in three orbitals) [Boeri et al. (2008); Haule et al. (2008)]. Our analysis shows that a FS with approximately a similar size for the hole and electron pockets can be obtained both at fillings around one and two thirds, but the two almost degenerate hole pockets around Γ demand a filling larger than half filling. Thus, the focus of our effort will be on two thirds filling, which can be obtained by using the chemical potential $\mu = 0.212$. Since the Hamiltonian for a one-iron unit cell has been considered, then k runs within the corresponding extended BZ $-\pi \leq k_x, k_y \leq \pi$.

The Coulombic interacting portion of the Hamiltonian, first introduced in Section 2.3, is given by:

$$\begin{aligned} H_{\text{int}} =& U \sum_{\mathbf{i},\alpha} n_{\mathbf{i},\alpha,\uparrow} n_{\mathbf{i},\alpha,\downarrow} + (U' - J/2) \sum_{\mathbf{i},\alpha<\beta} n_{\mathbf{i},\alpha} n_{\mathbf{i},\beta} \\ & - 2J \sum_{\mathbf{i},\alpha<\beta} \mathbf{S}_{\mathbf{i},\alpha} \cdot \mathbf{S}_{\mathbf{i},\beta} \quad + J \sum_{\mathbf{i},\alpha<\beta} (d^{\dagger}_{\mathbf{i},\alpha,\uparrow} d^{\dagger}_{\mathbf{i},\alpha,\downarrow} d_{\mathbf{i},\beta,\downarrow} d_{\mathbf{i},\beta,\uparrow} + h.c.), \end{aligned} \tag{5.9}$$

where $\alpha, \beta = xz, yz, xy$ denote the orbital, $\mathbf{S}_{\mathbf{i},\alpha}$ ($n_{\mathbf{i},\alpha}$) is the spin (electronic density) in orbital α at site $\mathbf{i}$, and the relation $U' = U - 2J$ between these Kanamori parameters has been used (for a discussion in the manganite context see [Dagotto et al. (2001)] and references therein).

5.2 Magnetic Properties of the Undoped State

A mean field study was performed on this model to explore the ground-state properties of the three orbital model. In this study three possible orbital-order patterns will be considered: (i) Ferro-orbital (FO) order which corresponds to the orbitals xz and yz having different electronic densities, (ii) alternating orbital (AO) order, and (iii) stripe orbital (SO) order. Combined with the magnetic spin order, these orbital orders lead to a large variety of possible combinations of polarized or alternating spin and orbital order. Here phases that can be expressed using (at most) two ordering vectors have been considered, i.e., $\mathbf{q}_1$ for magnetic order and $\mathbf{q}_2$ for orbital order. The expectation values for the mean-field proposed states can be expressed as [Daghofer et al. (2010)]:

$$\langle n_{\mathbf{r},xy,\sigma}\rangle = n_{xy} + \frac{\sigma}{2}\mathrm{e}^{i\mathbf{q}_1\cdot\mathbf{r}} m_{xy} \tag{5.10}$$

$$\langle n_{\mathbf{r},\alpha,\sigma}\rangle = n + \frac{\sigma}{2}\mathrm{e}^{i\mathbf{q}_1\cdot\mathbf{r}} m + \frac{\alpha}{2}\mathrm{e}^{i\mathbf{q}_2\cdot\mathbf{r}} p + \frac{\sigma\alpha}{2}\mathrm{e}^{i(\mathbf{q}_1+\mathbf{q}_2\cdot)\mathbf{r}} q\ , \tag{5.11}$$

where the first equation with the mean-field parameters n_{xy}, m_{xy} describes the xy orbital and the second equation with parameters n, m, p, and q applies to the xz/yz subsystem, with $\alpha = \pm 1$ indicating the xz/yz orbitals. These expectation values were applied to the same interacting Hamiltonian which was used in the two orbital model, Eqn. (2.24).

Around $J/U{=}\frac{1}{4}$ the realistic AF order is found with ordering momentum $\mathbf{q}_1{=}(\pi{,}0)$ for all values of U>U$_{c_1}$, where U$_{c_1}$ ≈0.6. Figure 5.2 (a) shows how the staggered magnetization with ordering momentum (π,0) increases with Coulomb repulsion U. As previously found for two and four orbital models [Yu et al. (2009)]. intermediate U leads to an anti-ferromagnetic metal. The system remains non-magnetic for small U up to U$_{c_1}$. For U>U$_{c_1}$, the spin (π,0) ordered magnetic moment starts to grow, see Fig. 5.2 (a), but the band structure remains metallic.

The Fermi surface for U=0.7, where the Coulomb repulsion is just barely strong enough to induce (π,0) antiferromagnetism, is shown in Figs. 5.3 (a) and (b). More specifically, Fig. 5.3 (a) shows the Fermi surface in the extended BZ for spin stripes running along the y direction, i.e. for the ordering vector (π,0). While the electron pocket at (0,π) is hardly affected, the pocket at (π,0) has almost disappeared. Of the two hole pockets, the inner one has also disappeared for momenta (0,k$_y$), because a gap has developed at the chemical potential μ. For momenta (k$_x$,0), in contrast, the gap in the *outer* pocket lies below μ, and the band consequently forms a very small electron pocket. This result is in qualitative agreement with the unconventional electronic reconstruction observed with ARPES in (Ba,Sr)Fe$_2$As$_2$ [Yi et al. (2009)]. Figure 5.3 (b) shows the superposition of the Fermi surfaces obtained for the two equivalent ordering vectors (π,0) and (0,π) in the reduced BZ corresponding to the two-Fe unit cell. If U is increased to U=0.9, the gap in the outer hold pocket along (k_x,0) increases and pushes the outer band above the chemical potential; the small electron pockets seen for U=0.7 in Fig. 5.3 (a) consequently disappear, and only one hole pocket remains around Γ, see Fig. 5.3 (c). The (0,π) electron pocket remains unaffected, but at (π,0), a hole-like shadow pocket with very low spectral weight has replaced the original electron pocket. The band that formed the vanished electron pocket at U=0 has been deformed strongly enough to create a small *hole*like pocket at $\approx$=(π/2,0). As it can be seen in Fig. 5.3 (d), this hole pocket touches the (π,0) electron pocket once the results for ordering vectors (π,0) and (0,π) are combined. As U continues to increase within the magnetic metallic phase no further qualitative changes are observed as can be seen in Figs. 5.3 (e) and (f).

The average electronic occupation numbers for the three orbitals, shown in Fig. 5.2 (b), are not significantly affected by the onset of antiferromagnetism. The small difference in the electronic population observed is driven by the different orbital magnetizations [see Fig. 5.2 (a)] and is due to the orbital anisotropy relative to the direction of the magnetic (π,0) colinear order. Note that the difference between m_{xz} and m_{yz} in Fig. 5.2 (a) is larger than the difference between n_{xz} and n_{yz} in Fig. 5.2 (b) indicating that q is more important than p.

When a second critical coupling U_{c_2} $\approx$1.23 is reached, the system develops orbital order with an ordering momentum (π,π), different from the magnetic ordering vector (π,0). The system remains a metal through this second transition as well. If U is further increased, a metal-insulator transition finally occurs at a third critical U_{c_3} $\approx$1.43. At this point the orbital order changes: as can be concluded from the orbital densities shown in Fig. 5.2 (b), the system develops ferro-orbital order. The spin (π,0) persists.

Summarizing, our mean field calculations indicate the existence of four distinct phases that are stabilized with growing Coulomb repulsion U: (i) a disordered, paramagnetic phase for $U<U_{c_1}$, (ii) a metallic phase with (π,0) or (0,π) magnetic order for $U_{c_1} <U<U_{c_2}$, (iii) a metallic magnetic phase for $U_{c_2} <U<U_{c_3}$ with alternating

Table 5.2: Symmetry properties of the terms in the three orbital tight-binding Hamiltonian.

Term	IR
ϵ_k	A_{1g}
δ_k	B_{1g}
γ_k	B_{2g}
$(\alpha_k^{(1)}, \alpha_k^{(2)})$	E_g
h_k	A_{1g}

orbital order with ordering vector (π,π) and (iv) a ferro-orbitally ordered insulator with spin (π,0) magnetic order for U>U_{c_2}, where the yz [xz] orbital has larger electronic occupation for magnetic ordering vector (π,0) [(0,π)].

5.3 Pairing Operators in the Three Orbital Model

As with the two orbital model, spin-singlet pairing operators that are allowed by lattice and orbital symmetries in the three orbital model will be constructed and tabulated in this section. Since now there are three orbitals the 3x3 Gell-mann matrices will be used, λ_i, a generalization of the Pauli matrices (see Appendix A for a full list) as well as λ_0 the 3x3 identity matrix. In this representation our tight binding Hamiltonian becomes:

$$H_{TB}(\mathbf{k}) = \sum_{\mathbf{k},\sigma} \Psi^\dagger_{\mathbf{k},\sigma} \xi_k \Psi_{\mathbf{k},\sigma} \tag{5.12}$$

where $\Psi^\dagger_{\mathbf{k},\sigma} = [d^\dagger_{xz}(\mathbf{k}), d^\dagger_{yz}(\mathbf{k}), d^\dagger_{xy}(\mathbf{k})]$ and

$$\xi_k = \epsilon_k\lambda_0 + \delta_k\lambda_3 + \gamma_k\lambda_1 + \alpha_k^{(1)}\lambda_5 + \alpha_k^{(2)}\lambda_7 + h_k\lambda_8 \tag{5.13}$$

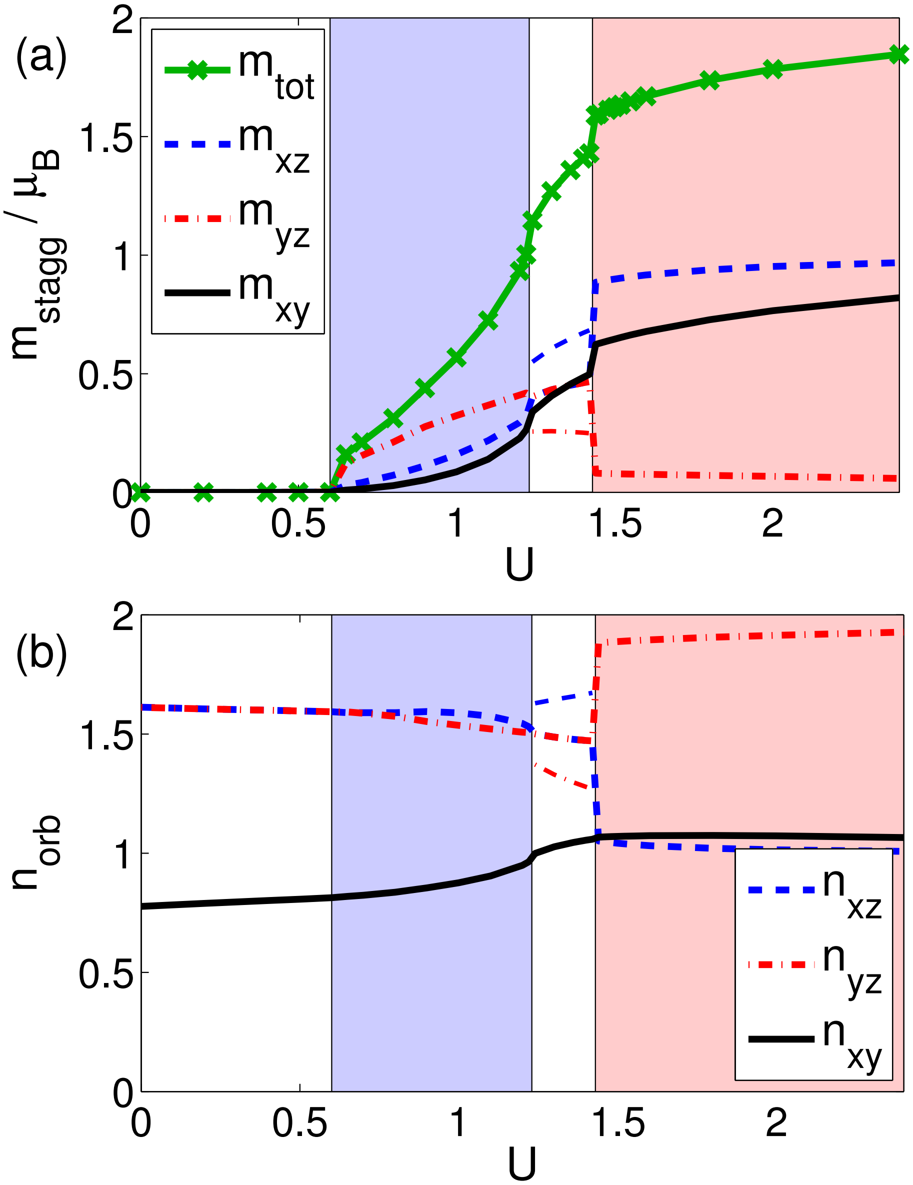

Figure 5.2: (a) Orbital magnetization and (b) occupation number as a function of the Coulomb repulsion strength U, obtained with a mean-field approximation. The colors indicate the different phases (for increasing U): uncorrelated metal, itinerant $(\pi, 0)$ antiferromagnet without orbital order, itinerant $(\pi, 0)$ antiferromagnet with alternating orbital order [small white window, spin-orbital order], and a ferro-orbitally-ordered $(\pi, 0)$ antiferromagnetic insulator [spin-orbital order]. Hopping parameters are from Tab. 5.1, and $J = U/4$. For the phase with alternating orbital order, the thin lines show (a) $m \pm q$ and (b) $2n \pm p$ [Daghofer et al. (2010)].

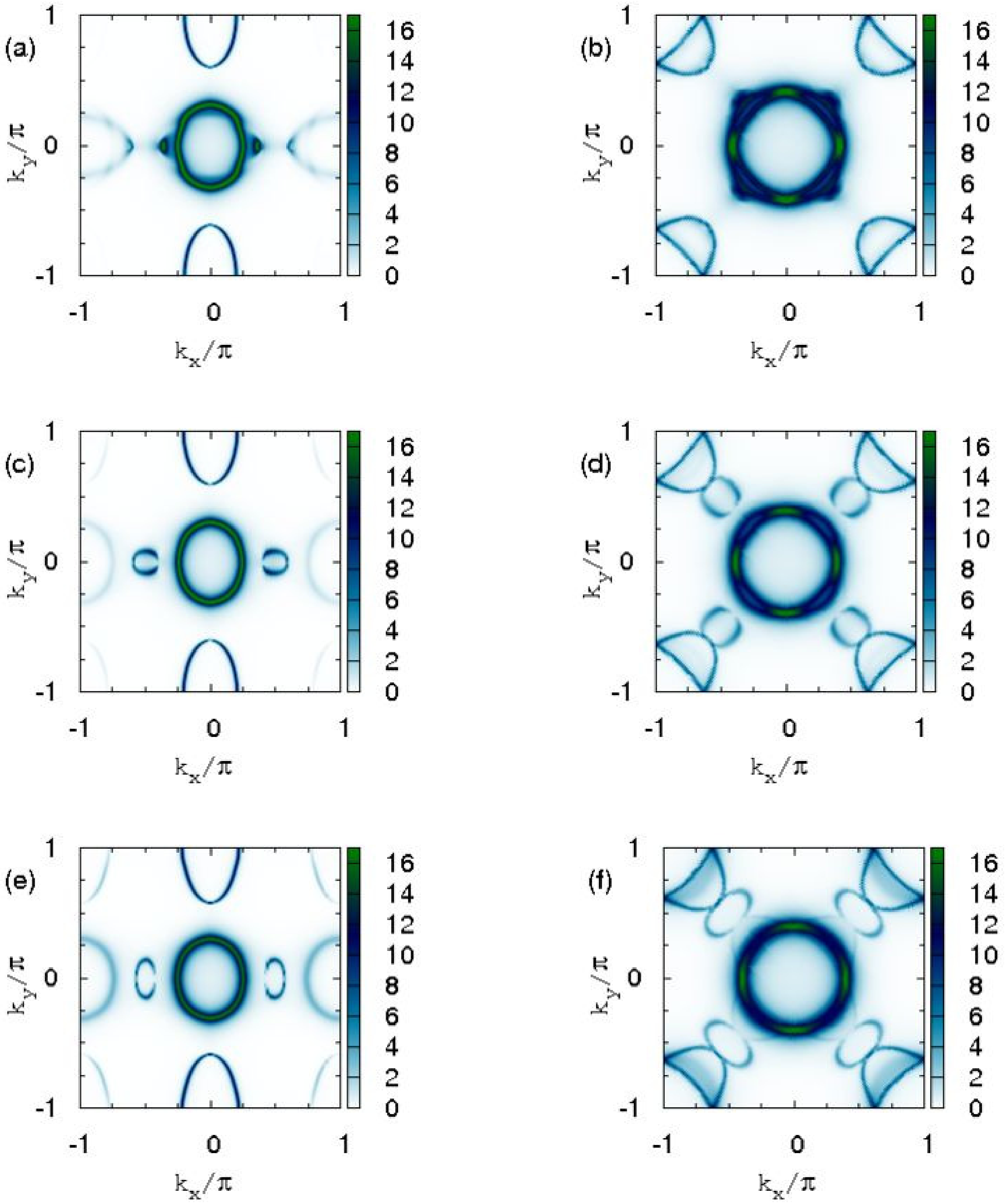

Figure 5.3: Fermi surface in the orbital-disordered spin-antiferromagnetic metallic phase with (a,b) $U = 0.7$, (c,d) $U = 0.9$, and (e,f) $U = 1.1$. (a,c,e) show the unfolded BZ containing one Fe, for the antiferromagnetic ordering vector $q = (\pi, 0)$. (b,d,f) depict the superposition of the FSs for $\mathbf{q} = (\pi, 0)$ and $\mathbf{q} = (0, \pi)$ in the (rotated) folded BZ corresponding to two Fe atoms. The ratio $J = U/4$ was used [Daghofer et al. (2010)].

with

$$
\begin{aligned}
\epsilon_k &= \frac{T^{11}+T^{22}}{2\sqrt{3}} - \frac{T^{33}}{\sqrt{3}} \\
&= \frac{2}{3}(t_1+t_2+t_5)(\cos k_x + \cos k_y) \\
&\quad + \frac{4}{3}(2t_3+t_6)\cos k_x \cos k_y - \mu + \frac{\Delta_{xy}}{3} \qquad (5.14) \\
\delta_k &= \frac{T^{11}-T^{22}}{2} \\
&= -(t_1-t_2)(\cos k_x - \cos k_y) \qquad (5.15) \\
\gamma_k &= T^{12} = 4t_4 \sin k_x \sin k_y \qquad (5.16) \\
\alpha_k^{(1)} &= \frac{T^{13}}{i} \\
&= -2t_7 \sin k_x - 4t_8 \sin k_x \cos k_y \qquad (5.17) \\
\alpha_k^{(2)} &= \frac{T^{23}}{i} \\
&= -2t_7 \sin k_y - 4t_8 \sin k_y \cos k_x \qquad (5.18) \\
h_k &= \frac{T^{11}+T^{22}}{2\sqrt{3}} - \frac{T^{33}}{\sqrt{3}} \\
&= \frac{1}{\sqrt{3}}(t_1+t_2-2t_5)(\cos k_x + \cos k_y) \\
&\quad + \frac{4}{\sqrt{3}}(t_3-t_6)\cos k_x \cos k_y - \frac{\Delta_{xy}}{\sqrt{3}} \qquad (5.19)
\end{aligned}
$$

Again each element in Eqns (5.14)-(5.19) transforms according to one irreducible representation of the D$_{4h}$ point group. The classification is given in Table 5.2. Since the Hamiltonian has to transform according to A$_{1g}$, the Gell-mann matrices in the orbital basis here transform as indicated in Table 5.3. The spin-singlet pairing operator in the three orbital model is similar to the two orbital operator:

$$\Delta^\dagger = f(\mathbf{k})(\lambda_i)_{\alpha,\beta}(d^\dagger_{\mathbf{k},\alpha,\uparrow}d^\dagger_{-\mathbf{k},\alpha,\downarrow} - d^\dagger_{\mathbf{k},\beta,\uparrow}d^\dagger_{-\mathbf{k},\alpha,\downarrow}) \qquad (5.20)$$

where a sum over repeated indices is implied; the operators $d^\dagger_{\mathbf{k},\alpha,\sigma}$ have been defined in the previous sections and $f(\mathbf{k})$ is the form factor that transforms according to one of the irreducible representations of the crystal's symmetry group. Although $f(\mathbf{k})$

Table 5.3: Symmetry properties of the Gell-mann matrices in the tight-binding Hamiltonian.

Matrix	IR
λ_0	A$_{1g}$
λ_1	B$_{2g}$
λ_2	A$_{2g}$
λ_3	B$_{1g}$
(λ_4, λ_6)	E$_g$
(λ_5, λ_7)	E$_g$
λ_8	A$_{1g}$

may, in general, have a very complicated form, a short pair-coherence length requires the two electrons that form the pair to be very close to each other. Consequently, for simplicity this work will focus on nearest and diagonal next-nearest neighbors, and form factors that are allowed in a lattice with D_{4h} symmetry.

5.3.1 Intraorbital Pairing

The previous section shows that the symmetry of the pairing operator will be exclusively determined by the symmetry of $f(\mathbf{k})$ *only* if λ_i transforms as A$_{1g}$. Table 5.3 indicates that this is the case for pairing operators which contain λ_0 and λ_8. These two matrices are diagonal, which means that such pairing operators define *intraorbital* pairings. For intraorbital pairing, with a symmetry fully determined by the spatial form factor, the basis functions are given by I: $f(\mathbf{k})\lambda_0$ or II: $f(\mathbf{k})\lambda_8$. In I, the superconducting order parameter (OP) will be the same for all three orbitals while II allows the OP for the d_{xz} and d_{yz} orbitals to be different from the d_{xy} orbital. Thus the addition of another orbital may lead to the possibility of different superconducting gaps.

For all other OPs, the symmetry is given by the product of the symmetry of the form factor with its orbital component given in Table 5.4. For example, for $\lambda_i = \lambda_3$ the pairing is still intraorbital, but since λ_3 transforms as B$_{1g}$ the symmetry of the OP

Table 5.4: Properties of pairing operators allowed by lattice and orbital symmetries. f indicates the symmetry of $f(\mathbf{k})$.

No.	IR	Basis	Gap
I	f	$f(\mathbf{k})\lambda_0$	Full or Nodal
II	f	$f(\mathbf{k})\lambda_8$	Full or Nodal
III	$f\mathrm{B}_{1g}$	$f(\mathbf{k})\lambda_3$	Nodal
IV	$f\mathrm{B}_{2g}$	$f(\mathbf{k})\lambda_1$	Nodal
V_a	A_{1g}	$\mathrm{sink}_x\lambda_4+\mathrm{sink}_y\lambda_6$	Nodal
V_b	A_{1g}	$\mathrm{sink}_x\mathrm{cosk}_y\lambda_4+\mathrm{cosk}_x\mathrm{sink}_y\lambda_6$	Nodal
V_c	B_{1g}	$\mathrm{sink}_x\lambda_4-\mathrm{sink}_y\lambda_6$	Nodal
V_d	B_{1g}	$\mathrm{sink}_x\mathrm{cosk}_y\lambda_4$-$\mathrm{cosk}_x\mathrm{sink}_y\lambda_6$	Nodal
V_e	A_{2g}	$\mathrm{sink}_x\lambda_6+\mathrm{sink}_y\lambda_4$	Nodal
V_f	A_{2g}	$\mathrm{cosk}_x\mathrm{sink}_y\lambda_4+\mathrm{sin}k_x\mathrm{cosk}_y\lambda_6$	Nodal
V_g	B_{2g}	$\mathrm{sink}_x\lambda_6-\mathrm{sink}_y\lambda_4$	Nodal
V_h	B_{2g}	$\mathrm{cosk}_x\mathrm{sink}_y\lambda_4$-$\mathrm{sin}k_x\mathrm{cosk}_y\lambda_6$	Nodal

will only be B_{1g} if and only if $f(\mathbf{k})$ transforms as A_{1g}. The OP with A_{1g} symmetry found in numerical calculations in the two orbital model is intraorbital.

5.3.2 Interorbital Pairing

The remaining six Gell-mann matrices lead to interorbital pairing. Motivated by the two orbital model results, suggesting a spin-singlet pairing operator with f($\mathbf{k}$)=$\cos k_x$+$\cos k_y$ for intermediate values of the Coulomb repulsion U, see basis IV given in Table 5.4. This operator mixes d_{xz} and d_{yz} orbitals via λ_1 but with no d_{xy} orbital weight. However, the addition of the xy orbital leads to the possibility of new interorbital pairing operators, i.e., pairing between electrons in the d_{xz}, d_{yz} orbitals with the d_{xy} orbital.

5.3.3 Band Representation

To obtain the gap structure for the pairing operators in Table 5.4 the Bogliubov-de Gennes (BdG) Hamiltonian is constructed and is given by [Daghofer et al. (2010)]:

$$H_{BdG} = \sum_{\mathbf{k}} \psi^{\dagger}_{\mathbf{k}} H^{MF}_{\mathbf{k}} \psi_{\mathbf{k}} \tag{5.21}$$

with the definitions:

$$\psi^{\dagger}_{\mathbf{k}} = (d^{\dagger}_{\mathbf{k},xz,\uparrow} d^{\dagger}_{\mathbf{k},yz,\uparrow} d^{\dagger}_{\mathbf{k},xy,\uparrow} d_{-\mathbf{k},xz,\downarrow} d_{-\mathbf{k},yz,\downarrow} d_{-\mathbf{k},xy,\downarrow}) \tag{5.22}$$

and

$$H^{MF}_{\mathbf{k}} = \begin{pmatrix} H_{TB}(\mathbf{k}) & P(\mathbf{k}) \\ P^{\dagger}(\mathbf{k}) & -H_{TB}(\mathbf{k}) \end{pmatrix} \tag{5.23}$$

where

$$P(\mathbf{k})_{\alpha,\beta} = V f(\mathbf{k})(\lambda_i)_{\alpha,\beta} \tag{5.24}$$

Pairing amplitude V is the magnitude of the OP given by the product of the pairing attraction V_0 and a mean-field parameter Δ that should be obtained from minimization of the total energy.

Up to this point, this work has used the orbital representation, since it is both easy to work with in obtaining the form of the Hamiltonian and the pairing operators allowed by the symmetry of the lattice and orbitals. However, experimentally observed superconducting gaps occur at the FS formed by the bands that result from the hybridization between orbitals. For this reason, it is convenient to express Eqn. (5.23) in the band representation. $H_{TB}(\mathbf{k})$ can be expressed in the band representation via the transformation $H_{band}(\mathbf{k}) = U^{\dagger}(\mathbf{k})H_{TB}(\mathbf{k})U(\mathbf{k})$, where $U(\mathbf{k})$ is the unitary change of basis matrix and $U^{\dagger}(\mathbf{k})$ is the transpose conjugate of $U(\mathbf{k})$. Since U is unitary, for each value of $\mathbf{k}$, $\sum_i (U_{\mathbf{i},j})^* U_{\mathbf{k},i} = \delta_{j,k}$. Then $H'_{MF} = G^{\dagger} H_{MF} G$, where G

is the 6×6 unitary matrix composed of two 3×3 blocks given by U. Then

$$H'^{MF}_{\mathbf{k}} = \begin{pmatrix} H_{Band}(\mathbf{k}) & P_B(\mathbf{k}) \\ P^{\dagger}_B(\mathbf{k}) & -H_{Band}(\mathbf{k}) \end{pmatrix} \tag{5.25}$$

with

$$P_B(\mathbf{k}) = U^{-1}(\mathbf{k})P(\mathbf{k})U(\mathbf{k}) \tag{5.26}$$

Consider the s± pairing operator, which corresponds to pairing operator I with f($\mathbf{k}$)=cosk$_x$cosk$_y$ in Table 5.4. In the orbital representation:

$$P(\mathbf{k})_{\alpha,\beta} = V(cosk_x cosk_y)\delta_{\alpha,\beta} \tag{5.27}$$

which is purely intraorbital with equal weight on each orbital. In the band representation our pairing matrix becomes:

$$\begin{aligned} P_B(\mathbf{k})_{\alpha,\beta} &= U^{-1}(\mathbf{k})V(cosk_x cosk_y)\delta_{\alpha,\beta}U(\mathbf{k}) \\ &= V(cosk_x cosk_y)\delta_{\alpha,\beta}U^{-1}(\mathbf{k})U(\mathbf{k}) \\ &= V(cosk_x cosk_y)\delta_{\alpha,\beta} \end{aligned} \tag{5.28}$$

Thus the s± OP is purely intra-band. Thinking about this further, it is clear that a pairing operator with only intra-band terms is a very special case. For a purely intra-band pairing interaction, the OP must have only intraorbital terms which treats each orbital equally. In Fig. 5.4 the spectral functions A($\mathbf{k}$,ω) are presented along high symmetry directions in the reduced Brillouin zone for V=0, i.e., without pairing, and with pairing for V=0.2. As the pairing interaction is turned on, a gap opens at the FS and the shadow Bogoliubov bands appear. As has been numerically verified, no nodes occur anywhere in the BZ. Note that the gap is momentum dependent because f($\mathbf{k}$)=cosk$_x$cosk$_y$. This pairing operator is in agreement with ARPES [Kondo et al. (2008); Ding et al. (2008); Nakayama et al. (2009); Wray et al. (2008); Kim et al. (2010)].

However, symmetry only requires the d_{xz} and d_{yz} orbital to have the same OP, while the d_{xy} can have a different one. There does not seem to be any reason to assume that electrons in the many bands that determine the FS should be affected by the same pairing interaction. In fact, in MgB_2 the electron-phonon interaction that provides the pairing is stronger in the σ bands than in the π bands, giving two different gaps. Combining pairing operators I and II with f(**k**)=cosk$_x$cosk$_y$ so that the orbital part of the basis is given by $A\lambda_0+B\lambda_8$, where A and B are constants, produces a pairing operator which has one weight for the d_{xz}/d_{yz} orbitals but another for the d_{xy} orbital, which will be referred to as s_{IB}. In the band representation this operator is inter-band, but still has A_{1g} symmetry. The spectral functions for the s_{IB} pairing operator are shown in Fig 5.5. For a robust range of values of A and B, a nodeless gap opens on all FSs for any finite value of V. The major different with the results for the s± state is that the inter-band pairing present in s_{IB} open gaps between the bands far away from the FS. Also larger gaps are opened at (0,π) and (π,0). The bottom panel on Fig 5.5 (b) shows the ratio R between the gap sizes of $s_\pm$ and s_{IB} pairing operators for V=0.05. The only appreciable difference can be seen on the electron pockets, since these are the only bands which cross the FS with d_{xy} orbital weight. The points with R=2 are points where the electron pockets are formed entirely by d_{xy} orbitals, in other points the bands are composed of hybridizations between d_{xy} with d_{xz}/d_{yz}.

Finally, another inter-band OP which will be considered is the numerically favored B_{2g} operator found in the two orbital model and its three orbital extension B_{2g}^{ext}. The B_{2g} pairing operator is created by combining IV with f(**k**)=cosk$_x$+cosk$_y$. Since this operator is interorbital, in the band representation it has both intra-band and inter-band components. This operator creates a full gap around the hole pockets, since these pockets are composed of d_{xz}/d_{yz} orbitals, and nodal gaps around the electron pockets, since this operator has no d_{xy} component, see Fig 5.6. The next pairing

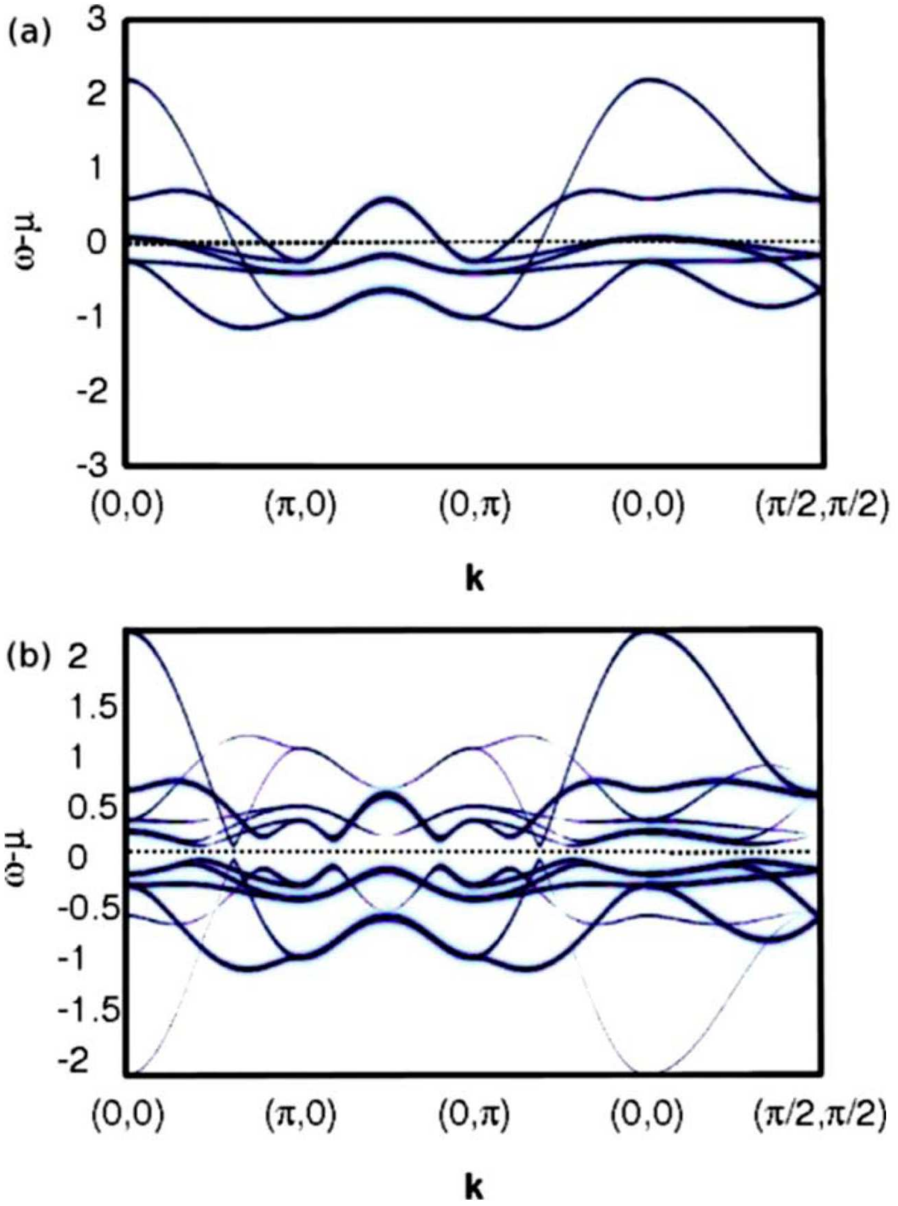

Figure 5.4: The intensity of the points represents the values of the spectral function A($\mathbf{k}$,ω) for the three orbital model with pairing interaction (a) V=0; (b) V=0.2 for the s± pairing operator given in the text [Daghofer et al. (2010)].

operator, the B_{2g}^{ext}, is created by combining the B_{2g} operator with V_g, i.e. next nearest-neighbor interorbital pairing. In this pairing between all three orbitals is allowed. This pairing operator lifts the nodes in the hole pockets but nodes on the electron pockets remain, see Fig 5.6. This is because one of the electron pockets is formed by a non-hybridized orbital d_{xy} along this direction, and the relevant pairing interaction is zero along the Γ-X/Y directions in momentum space.

5.4 Conclusions

In this Chapter, a simple three-orbital Hamiltonian has been constructed involving the $3d$ orbitals xz, yz, and xy. These orbitals have the largest weight at the FS of the pnictide LaOFeAs, according to LDA calculations. It was shown that it is possible to qualitatively reproduce the shape of the LDA-FS by fixing the electron filling to 4 electrons per Fe. Moreover, two features that have been criticized in the two-orbital model have now been corrected: both hole pockets now arise from bands degenerate at the Γ-point, and there is no pocket around M in the extended BZ. In addition, the xy character of a small piece of the electron pockets is now properly reproduced.

Numerical calculations using a small 2×2 lattice show a tendency to the development of magnetic $(\pi, 0)$-$(0, \pi)$ colinear order when Coulombic interactions are added, result consistent with experimental observations. A mean-field analysis confirms this tendency for physically relevant values of J/U. As in the case of the two-orbital model, an antiferromagnetic metallic phase occurs only at intermediate values of the Coulomb repulsion. At large U, the ground state is magnetic, but it is an insulator that is also orbitally ordered. Additionally, a metallic, magnetic and orbitally ordered phase is encountered just before the metal-insulator transition. In the most interesting regime with a spin-$(\pi, 0)$ antiferromagnetic metal without pronounced orbital order, the bands are similar to the uncorrelated ones, but their bandwidth is reduced with increasing U. The Fermi surface is also very similar to the uncorrelated one but, depending on U, this work finds small additional electron-like

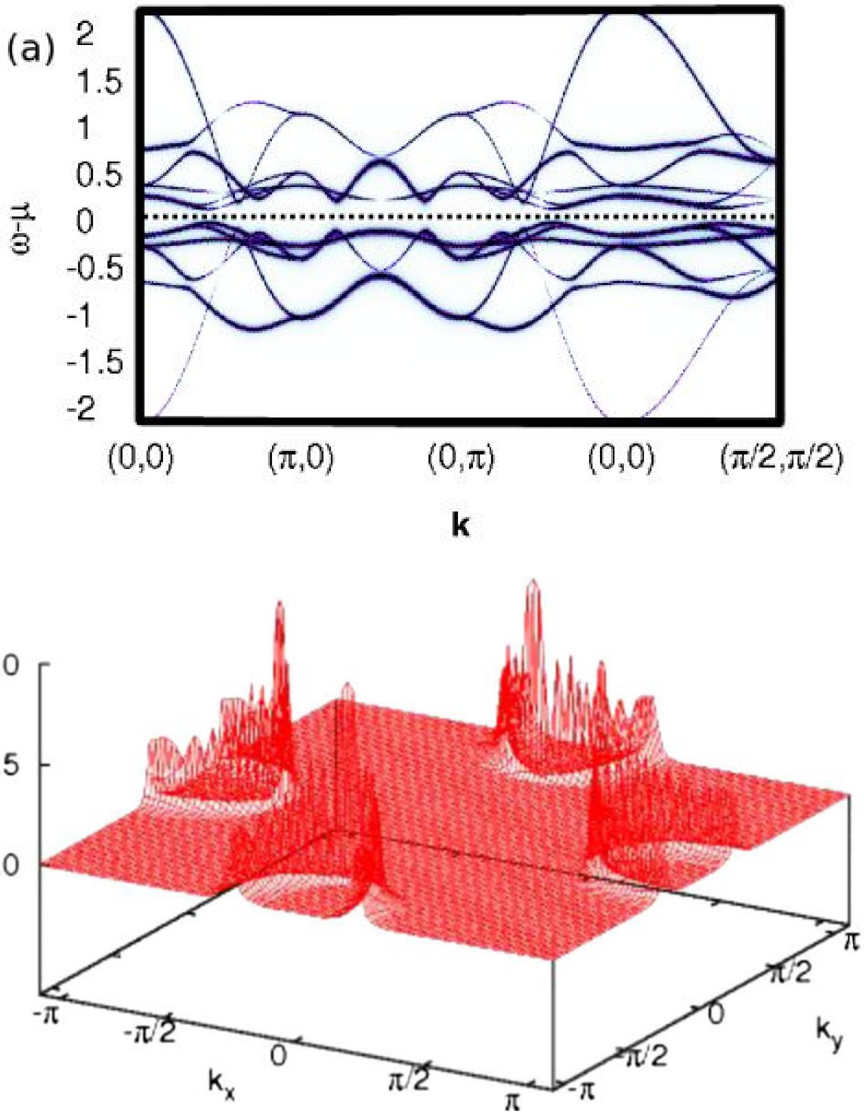

Figure 5.5: (a) The intensity of the points represents the values of the spectral function A($\mathbf{k}$,ω) for the three orbital model with pairing interaction V=0.2 for the s$_{IB}$ pairing operator. (b) Ratio R between the gaps for the pairing s$_{IB}$ and pairing s± for V=0.05 in the unfolded BZ [Daghofer et al. (2010)].

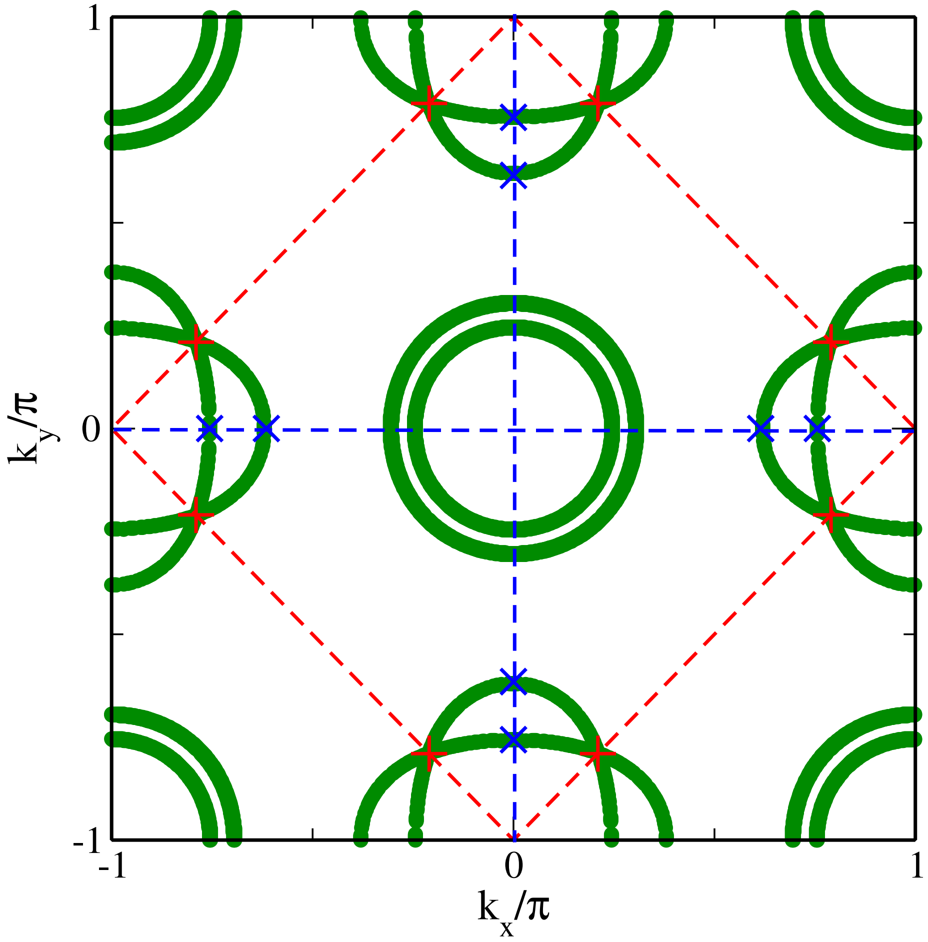

Figure 5.6: Location of nodes for the B_{2g} and B_{2g}^{ext} pairing operators. Red lines denote node lines for the form factor f($\mathbf{k}$)=$\cos k_x + \cos k_y$, while blue lines show where nodes develop due to the purely d_{xy} nature of the orbitals. The nodes exist for the two orbital B_{2g} operator since the orbital character of the electron pocket along the Γ-X/Y directions is purely d_{xy} which is not affected by this attraction. In the extension of the B_{2g} operator into three orbitals, the form factors pairing the d_{xy} orbital with the d_{xz}/d_{yz} orbitals is zero along the direction mentioned above.

pockets near the original hole pockets around Γ (small U) or hole-like pockets between the electron- and hole-pockets (at slightly larger U).

The possible pairing operators that are allowed by the symmetry of the lattice and the orbitals have been constructed for pairs made of electrons separated by a distance up to one diagonal lattice spacing. If on-site pairing is disregarded due to the large Coulomb repulsion, it was found that the only purely intra-band pairing operator that has a full gap on the FS is #I with $f(\mathbf{k}) = \cos k_x \cos k_y$ which corresponds to the $s\pm$ pairing operator with a momentum dependent OP that has opposite signs on the hole and electron FSs. This operator arises from a purely intra-band pairing attraction equal for each of the three bands. Note that the pairing operator #I is the *only* one that leads to purely intra-band pairing interactions. Since this pairing operator is proportional to the identity matrix λ_0 both in the orbital and the band representations, the ratio $|\Delta_i/\Delta_j|$ between the gaps in two different FSs can differ only by the ratios $|f(\mathbf{k}_i)/f(\mathbf{k}_j)|$; then, any experimental indication of a different kind of ratio would indicate some degree of inter-band pairing [Moreo et al. (2009a)]. Thus, order parameter ratios predicted by several authors [Parker et al. (2008); Bang and Choi (2008); Seo et al. (2008); Parish et al. (2008); Dolgov et al. (2009)] with calculations based on purely intra-band pairing (they allow inter-band hopping of intra-band pairs) are not allowed by the symmetry of the lattice and the orbitals. In this regard, our calculations seem to indicate that unrelated gaps in different FSs can occur only in systems in which at least one orbital (or a group of orbitals) is not strongly hybridized with the remaining ones.

Results show that all the other pairing operators, except for #I, lead to inter-band pairing attraction in the band representation. In addition, all the pairing operators with inter-band pairing studied here have nodal band structures at small V with the exception of pairing operator s_{IB}. In this case, the gap on the electron pockets is expected to have a stronger variation at different points in the BZ that the gap at the hole pockets. Thus, a strong indication that $s\pm$ is the appropriate pairing symmetry would be provided by experiments in the pnictides showing a nodeless gap in all FSs, relatively independent of momentum, and with similar values on all FSs.

Summarizing, the addition of a third orbital corrects the shortcomings pointed out in the two-orbital model: the two hole pockets now arise from bands degenerate at the Γ point while the electron pockets contain a small piece with xy character. However, the dependence of the magnetic phases with U for the undoped case appears to be similar for three and two orbitals except for a magnetic, orbital ordered, metallic phase that appears in the three-orbital case. In both models it is found that the only pairing operator allowed by symmetry with next or diagonal nearest-neighbor interactions which is purely intra-band and produces a nodeless gap is the $s\pm$ state. In addition, the only change observed in the interorbital B_{2g} pairing state, favored by numerical simulations in the two-orbital model, is that, at the mean-field level, the addition of the xy orbital renders the gap on the hole pockets nodeless for much smaller values of the pairing attraction.

Chapter 6

Conclusions

In this manuscript, the properties of the iron pnictides have been investigated using a variety of multi-orbital models. The first, as seen in Chapter 2, is a two orbital model, where only the Fe 3-d$_{xz}$ and 3-d$_{yz}$ orbitals were considered. In Section 2.2, a tight binding Hamiltonian was constructed via the Slater-Koster method and was fitted to band-structure calculations. On-site Coulomb interactions were included. The ground state of the model was found via exact diagonalization on a tilted 8-site cluster. Section 2.4 showed that, as a result of this effort, magnetic properties of the undoped parent compound are properly reproduced by this model. Also, following the behavior of the phase diagram in Fig. 1.2, simulated electron doping reduced colinear magnetic order. Ground state symmetries were obtained for a variety of values of the Hubbard repulsion U and Hund J. It was found that there exists triplet regions (low U large J), along with spin-singlet regions with A$_{1g}$(large U large J) and B_{2g} (low U low J) symmetry. Many spin singlet pairing operators, which obey lattice and orbital symmetry, were studied and it was found that two of these dominate. One is NN with interorbital pairing having B$_{2g}$ symmetry, the other has A$_{1g}$ symmetry and is in agreement with current theoretical expectations.

Chapter 3 introduced Heisenberg terms, in addition to the on-site Coulomb interactions, into the two orbital model in order to enhance colinear magnetic order found experimentally, as well as to increase carrier attraction in order to produce tighter pairs that can be accommodated in a small cluster. Both the electron (Section 3.3) and hole doped (Section 3.4) cases were studied to find preferred pairing symmetries. The electron doped investigation found that, upon the introduction of Heisenberg spin interactions, quasi-nodal A_{1g} bound states were stabilized for physical values of J_H/U in the intermediate/large U region. A competing B_{2g} state was also found and could be stable in physically relevant regimes of $U/|t_1|$. In the hole doped case, a ground state that has pseudocrystal momentum (π,π) was found, which corresponds to anti-bonding rather than bonding combinations of the Fe d_{xz}/d_{yz} orbitals in the two-Fe atom unit cell. This means that pairing operators that are favored would arise from hole carriers located at the hole pockets at Γ and at M in the unfolded Brillouin zone. Several low-lying states with different pairing symmetries (including A_{1g}, B_{1g} and B_{2g}) were found. For this reason, as in the electron doped model, the symmetry of the pairing operator appears to be strongly dependent on the values of the interaction parameters.

In order to investigate the role of nesting and orbital hybridization in the origin of magnetic order in the pnictides a phenomenological model with different orbital character but with similar nesting properties was developed to compare with the two orbital model composed of Fe d-orbitals, see Chapter 4. This phenomenological model, which consisted of non-hybridized s-like orbitals, does not exhibit the $(0,\pi)$-$(\pi,0)$ magnetic order in the weak coupling limit as found in the d-model, seen in Section 4.3.3. In this parameter regime a transverse spin ordered state with no local magnetization was found, see Section 4.3.3. This state is insulating and is characterized by a gap that could be observed in ARPES experiments. However, the ordered magnetic state cannot be detected with neutron scattering. In the strong coupling limit, both models favored a magnetic (insulating) ground state.

Finally, a three orbital model was developed, in Chapter 5, to take into account the Fe 3-d_{xy} orbital which is present at the Fermi energy as part of the electron pockets. Because the size of the Hilbert space was too large for numerical calculations, mean field techniques were used instead. In Section 5.2, the magnetic tendencies were investigated leading to the discovery of four distinct phases in the model. For low U, a disordered paramagnetic phase was found, followed by a metallic phase with (π,0)-(0,π) magnetic order. Increasing U leads to a metallic magnetic phase with alternating orbital order and finally a ferro-orbitally ordered insulator with spin (π,0) magnetic order was found for large U. Furthermore, many pairing operators were found that obey lattice and orbital symmetries, see Section 5.3. The gap structure of these operators were investigated in detail. Most of these operators did not open full gaps at the Fermi energy, meaning that nodes remained. One notable exception is the $s_{\pm}$ pairing state, which is purely intra-band. An operator with the same symmetry of the $s_{\pm}$ was constructed which has some inter-band components. A full gap was opened as well. Next, the B_{2g} pairing operator from the two orbital study was studied in detail along with an extension into three orbitals. In both of these states, nodes remain on the Fermi surface.

Experiments indicate that all five 3-d orbitals of the Fe ions should be included in realistic models for the pnictides, but the need for unbiased tools, such as numerical calculations to guide the approximate approaches to deal with these complex systems, must also be considered. The results presented in this thesis have been very useful in order to develop mean-field ansatz for models with two, three, four and five orbitals. These studies have been able not only to consider more Fe 3-d orbitals, but also more lattice sites. For example, two critical values of U were unveiled by these techniques indicating that a magnetic metallic state occurs only at intermediate values of U [Yu et al. (2009)]. Also a charge-striped state was found in a Hartree-Fock study of the doped two orbital model [Luo et al. (2011)]. In a mean-field study of three and five orbital models, see [Luo et al. (2010)], a physical parameter region was obtained by comparing model spin structure factor and band structure to neutron scattering and angle-resolved photoemission experiments. In addition, a cluster-perturbation study on three and four orbital models calculated the spectral density and found evidence of a proposed nematic phase in the pnictides [Daghofer et al. (2012)].

This thesis addresses the study of superconducting pairing tendencies as well as the magnetic properties of the iron based superconductors. These materials bring an important new challenge with respect to previous studies for the cuprates: for the pnictides and the chalcogenides a *mutli-orbital* approach is needed, considerably increasing the effort of computational studies. The study of multi-orbital Hamiltonians in this context, such as the Hubbard model, defines a grand challenge to theorists since there are few many-body tools available to gather reliable information about these complex systems. The fascinating area of research defined by pnictides and chalcogenides surely will receive the attention of both theorists and experimentalists for a long time, since developing a working theory for high critical temperature superconductors is among the most important conceptual topics of research in condensed matter physics at present.

Bibliography

Bibliography

Ahilan, K., Ning, F. L., Imai, T., Sefat, A. S., Jin, R., McGuire, M. A., Sales, B. C., and Mandrus, D. (2008). *Phys. Rev. B*, 78(10):100501. 3, 39

Aichhorn, M., Pourovskii, L., Vildosola, V., Ferrero, M., Parcollet, O., Miyake, T., Georges, A., and Biermann, S. (2009). *Phys. Rev. B*, 80:085101. 52

Anisimov, V. I., Korotin, D. M., Korotin, M. A., Kozhevnikov, A. V., Kune, J., Shorikov, A. O., Skornyakov, S. L., and Streltsov, S. V. (2009). *Journal of Physics: Condensed Matter*, 21(7):075602. 75

Arnold, B. J., Kasahara, S., Coldea, A. I., Terashima, T., Matsuda, Y., Shibauchi, T., and Carrington, A. (2011). *Phys. Rev. B*, 83:220504. 78, 111

Bang, Y. and Choi, H.-Y. (2008). *Phys. Rev. B*, 78:134523. 133

Bascones, E., Calderón, M. J., and Valenzuela, B. (2010). *Phys. Rev. Lett.*, 104:227201. 110

Boeri, L., Dolgov, O. V., and Golubov, A. A. (2008). *Phys. Rev. Lett.*, 101(2):026403. 2, 5, 17, 18, 76, 116

Brydon, P. M. R., Daghofer, M., and Timm, C. (2011). *Journal of Physics: Condensed Matter*, 23(24):246001. 83, 104

Brydon, P. M. R. and Timm, C. (2009). *Phys. Rev. B*, 79:180504. 74, 84

Cao, C., Hirschfeld, P. J., and Cheng, H.-P. (2008). *Phys. Rev. B*, 77(22):220506. 3, 112

Chen, G. F., Li, Z., Li, G., Zhou, J., Wu, D., Dong, J., Hu, W. Z., Zheng, P., Chen, Z. J., Yuan, H. Q., Singleton, J., Luo, J. L., and Wang, N. L. (2008a). *Phys. Rev. Lett.*, 101(5):057007. 1

Chen, G. F., Li, Z., Wu, D., Li, G., Hu, W. Z., Dong, J., Zheng, P., Luo, J. L., and Wang, N. L. (2008b). *Phys. Rev. Lett.*, 100(24):247002. 1

Chen, X. H., Wu, T., Wu, G., Liu, R. H., Chen, H., and Fang, D. F. (2008c). *Nature*, 453(7196):761–762. 1

Chen, Y., Lynn, J. W., Li, J., Li, G., Chen, G. F., Luo, J. L., Wang, N. L., Dai, P., de la Cruz, C., and Mook, H. A. (2008d). *Phys. Rev. B*, 78(6):064515. 2, 4, 112

Christianson, A. D., Lumsden, M. D., Delaire, O., Stone, M. B., Abernathy, D. L., McGuire, M. A., Sefat, A. S., Jin, R., Sales, B. C., Mandrus, D., Mun, E. D., Canfield, P. C., Lin, J. Y. Y., Lucas, M., Kresch, M., Keith, J. B., Fultz, B., Goremychkin, E. A., and McQueeney, R. J. (2008). *Phys. Rev. Lett.*, 101(15):157004. 2

Chubukov, A. V., Efremov, D. V., and Eremin, I. (2008). *Phys. Rev. B*, 78(13):134512. 74, 76, 85, 93

Cricchio, F., Grånäs, O., and Nordström, L. (2010). *Phys. Rev. B*, 81:140403. 110

Cvetkovic, V. and Tesanovic, Z. (2009). *Europhys. Lett.*, 85:37002. 74

Daghofer, M., Moreo, A., Riera, J. A., Arrigoni, E., Scalapino, D. J., and Dagotto, E. R. (2008). *Phys. Rev. Lett.*, 101(23):237004. 33, 41, 42, 44, 55, 60, 75, 83, 108

Daghofer, M., Nicholson, A., and Moreo, A. (2012). *Phys. Rev. B*, 85:184515. 137

Daghofer, M., Nicholson, A., Moreo, A., and Dagotto, E. R. (2010). *Phys. Rev. B*, 81(1):014511. xi, xvi, 51, 75, 105, 106, 113, 114, 115, 118, 121, 122, 126, 129, 131

Dagotto, E. (1994). *Rev. Mod. Phys.*, 66:763–840. 1, 3, 5, 10, 33, 44

Dagotto, E., Hotta, T., and Moreo, A. (2001). *Physics Reports*, 344(13):1 – 153. 112, 117

Dagotto, E., Riera, J., and Young, A. P. (1990). *Phys. Rev. B*, 42:2347–2352. 54, 66

Daul, S., Scalapino, D. J., and White, S. R. (2000). *Phys. Rev. Lett.*, 84:4188–4191. 42

de la Cruz, C., Huang, Q., Lynn, J. W., Li, J., II, W. R., Zarestky, J. L., Mook, H. A., Chen, G. F., Luo, J. L., Wang, N. L., and Dai, P. (2008). *Nature*, 453:899–902. 2, 4, 33, 74, 112

Ding, H., Richard, P., Nakayama, K., Sugawara, K., Arakane, T., Sekiba, Y., Takayama, A., Souma, S., Sato, T., Takahashi, T., Wang, Z., Dai, X., Fang, Z., Chen, G. F., Luo, J. L., and Wang, N. L. (2008). *Europhys. Lett.*, 83(4):47001. 3, 55, 128

Dolgov, O. V., Mazin, I. I., Parker, D., and Golubov, A. A. (2009). *Phys. Rev. B*, 79:060502. 133

Dong, J., Zhang, H. J., Xu, G., Li, Z., Li, G., Hu, W. Z., Wu, D., Chen, G. F., Dai, X., Luo, J. L., Fang, Z., and Wang, N. L. (2008). *Europhys. Lett.*, 83(2):27006. 2, 4, 112

Dong, J. K., Zhou, S. Y., Guan, T. Y., Zhang, H., Dai, Y. F., Qiu, X., Wang, X. F., He, Y., Chen, X. H., and Li, S. Y. (2010). *Phys. Rev. Lett.*, 104:087005. 3, 39, 55

Eremin, I. and Chubukov, A. V. (2010). *Phys. Rev. B*, 81:024511. 99

Fulde, P. (1991). *Electron Correlations in Molecules and Solids*. Springer Series in Solid-State Science. 15, 21

Gang, W., Xi-Yu, Z., Lei, F., Lei, S., Cong, R., and Hai-Hu, W. (2008). *Chin. Phys. Lett.*, 25(6):2221–2224. 3, 39

Gao, Y., Su, W.-P., and Zhu, J.-X. (2010). *Phys. Rev. B*, 81:104504. 57

Goldman, A. I., Argyriou, D. N., Ouladdiaf, B., Chatterji, T., Kreyssig, A., Nandi, S., Ni, N., Bud'ko, S. L., Canfield, P. C., and McQueeney, R. J. (2008). *Phys. Rev. B*, 78(10):100506. 2, 4, 22, 26, 112

Goswami, Pallab, Nikolic, Predrag, and Si, Qimiao (2010). *EPL*, 91(3):37006. 75

Grafe, H.-J., Paar, D., Lang, G., Curro, N. J., Behr, G., Werner, J., Hamann-Borrero, J., Hess, C., . . . , N. L., Klingeler, R., and Büchner, B. (2008). *Phys. Rev. Lett.*, 101(4):047003. 3, 38, 39, 55

Graser, S., Maier, T. A., Hirschfeld, P. J., and Scalapino, D. J. (2009). *New J. Phys.*, 11(2):025016 (34pp). xii, 2, 5, 32, 55, 57, 75, 79, 83, 101, 107

Hai-Jun, Z., Gang, X., Xi, D., and Zhong, F. (2009). *Chinese Physics Letters*, 26(1):017401. 3, 5

Hansmann, P., Arita, R., Toschi, A., Sakai, S., Sangiovanni, G., and Held, K. (2010). *Phys. Rev. Lett.*, 104:197002. 52

Haule, K., Shim, J. H., and Kotliar, G. (2008). *Phys. Rev. Lett.*, 100(22):226402. 116

Higashitaniguchi, S., Seto, M., Kitao, S., Kobayashi, Y., Saito, M., Masuda, R., Mitsui, T., Yoda, Y., Kamihara, Y., Hirano, M., and Hosono, H. (2008). *Phys. Rev. B*, 78:174507. 2

Hotta, T. (2010). *Journal of the Physical Society of Japan*, 79(2):023709. 76

Hubbard, J. (1963). *Proceedings of the Royal Society of London Series A*, 276(1365):238–257. 7, 8

Ikeda, H., Arita, R., and Kuneš, J. (2010). *Phys. Rev. B*, 81:054502. 63, 67

Johnston, D. (2010). *Advances in Physics*, 59(6):803–1061. 5

Kamihara, Y., Watanabe, T., Hirano, M., and Hosono, H. (2008). *J. Am. Chem. Soc*, 130(11):3296. 1, 2

Kariyado, T. and Ogata, M. (2009). *Journal of the Physical Society of Japan*, 78(4):043708. 101

Kawabata, A., Lee, S. C., Moyoshi, T., Kobayashi, Y., and Sato, M. (2008). *J. Phys. Soc. Jpn.*, 77:103704. 3, 38

Kemper, A., Maier, T., Graser, S., Cheng, H.-P., Hirschfeld, P., and Scalapino, D. (2010). *New Journal of Physics*, 12:073030. 67, 75, 82, 101

Kim, K. W., Rössle, M., Dubroka, A., Malik, V. K., Wolf, T., and Bernhard, C. (2010). *Phys Rev B*, 81(21):214508. 3, 128

Kondo, T., Santander-Syro, A. F., Copie, O., Liu, C., Tillman, M. E., Mun, E. D., Schmalian, J., Bud'ko, S. L., Tanatar, M. A., Canfield, P. C., and Kaminski, A. (2008). *Phys. Rev. Lett.*, 101(14):147003. 3, 55, 127

Krellner, C., Caroca-Canales, N., Jesche, A., Rosner, H., Ormeci, A., and Geibel, C. (2008). *Phys. Rev. B*, 78(10):100504. 2, 4, 112

Krüger, F., Kumar, S., Zaanen, J., and van den Brink, J. (2009). *Phys. Rev. B*, 79(5):054504. 42, 75, 116

Kugel, K. I. and Khomskii, D. I. (1982). *Soviet Physics Uspekhi*, 25(4):231. 42

Kuroki, K., Onari, S., Arita, R., Usui, H., Tanaka, Y., Kontani, H., and Aoki, H. (2008). *Phys. Rev. Lett.*, 101(8):087004. 39, 50, 74, 75, 79

Lebegue, S. (2007). *Phys. Rev. B*, 75(3):035110. 3, 112

Lee, P. A. and Wen, X.-G. (2008). *Phys. Rev. B*, 78:144517. 56, 112

Luo, Q., Martins, G., Yao, D.-X., Daghofer, M., Yu, R., Moreo, A., and Dagotto, E. (2010). *Phys. Rev. B*, 82:104508. 45, 52, 63, 69, 70, 75, 90, 96, 97, 137

Luo, Q., Yao, D.-X., Moreo, A., and Dagotto, E. (2011). *Phys. Rev. B*, 83:174513. 137

Matano, K., Ren, Z.-A., Dong, X., Sun, L.-L., Zhao, Z. X., and qing Zheng, G. (2008). *Europhys. Lett.*, 83(5):57001. 3, 38, 39

Mazin, I. I., Singh, D. J., Johannes, M., and Du, M.-H. (2008). *Phys. Rev. Lett.*, 101(5):057003. 39, 50, 74, 75, 85, 93

Millo, O., Asulin, I., Yuli, O., Felner, I., Ren, Z.-A., Shen, X.-L., Che, G.-C., and Zhao, Z.-X. (2008). *Phys. Rev. B*, 78(9):092505. 3, 39

Moreo, A., Daghofer, M., Nicholson, A., and Dagotto, E. R. (2009a). *Phys. Rev. B*, 80:104507. 37, 133

Moreo, A., Daghofer, M., Riera, J. A., and Dagotto, E. (2012). *Phys. Rev. B*, 85:139904. 24

Moreo, A., Daghofer, M., Riera, J. A., and Dagotto, E. R. (2009b). *Phys. Rev. B*, 79(13):134502. xiii, 5, 20, 25, 27, 30, 33, 34, 37, 41, 42, 44, 50, 51, 55, 56, 60, 64, 75, 76, 83, 90, 105

Mukuda, H., Terasaki, N., Kinouchi, H., Yashima, M., Kitaoka, Y., Suzuki, S., Miyasaka, S., Tajima, S., Miyazawa, K., Shirage, P. M., Kito, H., Eisaki, H., and Iyo, A. (2008). *J. Phys. Soc. Jpn.*, 77(9):093704. 3, 39

Nakai, Y., Ishida, K., Kamihara, Y., Hirano, M., and Hosono, H. (2008). *J. Phys. Soc. Jpn.*, 77(7):073701. 3, 39

Nakamura, K., Arita, R., and Imada, M. (2008). *J. Phys. Soc. Jpn.*, 77(9):093711. 75

Nakayama, K., Sato, T., Richard, P., Xu, Y.-M., Sekiba, Y., Souma, S., Chen, G. F., Luo, J. L., Wang, N. L., Ding, H., and Takahashi, T. (2009). *EPL (Europhysics Letters)*, 85(6):67002. 3, 128

Nandi, S., Kim, M. G., Kreyssig, A., Fernandes, R. M., Pratt, D. K., Thaler, A., Ni, N., Bud'ko, S. L., Canfield, P. C., Schmalian, J., McQueeney, R. J., and Goldman, A. I. (2010). *Phys. Rev. Lett.*, 104:057006. xii, 4, 5

Nicholson, A., Ge, W., Riera, J., Daghofer, M., Moreo, A., and Dagotto, E. (2012). *Phys. Rev. B*, 85:024532. xiv, 41, 58, 59, 61, 69, 70, 71, 72, 73

Nicholson, A., Ge, W., Zhang, X., Riera, J., Daghofer, M., Oleś, A. M., Martins, G. B., Moreo, A., and Dagotto, E. (2011a). *Phys. Rev. Lett.*, 106:217002. 41, 46, 47, 48, 49, 51, 53, 56, 62, 63, 64, 65, 66, 105, 107, 108

Nicholson, A., Luo, Q., Ge, W., Riera, J., Daghofer, M., Martins, G. B., Moreo, A., and Dagotto, E. (2011b). *Phys. Rev. B*, 84:094519. xv, 80, 83, 87, 88, 91, 92, 96, 100, 103, 108

Oitmaa, J. and Betts, D. (1978). *Can. J. Phys.*, 56:897–901. 12

Oles, A. M. (1983). *Phys. Rev. B*, 28:327–339. 7, 9, 81

Parish, M. M., Hu, J., and Bernevig, B. A. (2008). *Phys. Rev. B*, 78(14):144514. 133

Parker, D., Dolgov, O. V., Korshunov, M. M., Golubov, A. A., and Mazin, I. I. (2008). *Phys. Rev. B*, 78(13):134524. 133

Parlett, B. N. (1980). *The Symmetric Eigenvalue Problem*. Prentice-Hall, NJ. 44

Raghu, S., Qi, X.-L., Liu, C.-X., Scalapino, D. J., and Zhang, S.-C. (2008). *Phys. Rev. B*, 77(22):220503. xii, 29, 30, 42, 43, 56, 74

Ran, Y., Wang, F., Zhai, H., Vishwanath, A., and Lee, D.-H. (2009). *Phys. Rev. B*, 79:014505. 78, 82

Ren, Z.-A., Che, G.-C., Dong, X.-L., Yang, J., Lu, W., Yi, W., Shen, X.-L., Li, Z.-C., Sun, L.-L., Zhou, F., and Zhao, Z.-X. (2008a). *Europhys. Lett.*, 83(1):17002. 1

Ren, Z.-A., Lu, W., Yang, J., Yi, W., Shen, X.-L., Li, Z.-C., Che, G.-C., Dong, X.-L., Sun, L.-L., Zhou, F., and Zhao, Z.-X. (2008b). *Chin. Phys. Lett.*, 25:2215. 1

Ren, Z.-A., Yang, J., Lu, W., Yi, W., Che, G.-C., Dong, X., Sun, L.-L., and Zhao, Z. (2008c). *Mater. Res. Innovations*, 12:105. 1

Rodriguez, J. P. and Rezayi, E. H. (2009). *Phys. Rev. Lett.*, 103:097204. 110

Scalettar, R. T., Singh, R. R. P., and Zhang, S. (1991). *Phys. Rev. Lett.*, 67:370–373. 107

Seo, K., Bernevig, B. A., and Hu, J. (2008). *Phys. Rev. Lett.*, 101(20):206404. 55, 75, 133

Shan, L., Wang, Y., Zhu, X., Mu, G., Fang, L., Ren, C., and Wen, H.-H. (2008). *EPL (Europhysics Letters)*, 83(5):57004. 3, 39

Shimojima, T., Ishizaka, K., Ishida, Y., Katayama, N., Ohgushi, K., Kiss, T., Okawa, M., Togashi, T., Wang, X. Y., Chen, C. T., Watanabe, S., Kadota, R., Oguchi, T., Chainani, A., and Shin, S. (2010). *Phys. Rev. Lett.*, 104(5):057002. 77, 111

Si, Q. and Abrahams, E. (2008). *Phys. Rev. Lett.*, 101:076401. 4 pages, 4 figures. 55, 74, 75, 105

Singh, D. J. and Du, M.-H. (2008). *Phys. Rev. Lett.*, 100(23):237003. 3, 19

Slater, J. C. and Koster, G. F. (1954). *Phys. Rev.*, 94(6):1498–1524. 17, 19, 22

Suhl, H., Matthias, B. T., and Walker, L. R. (1959). *Phys. Rev. Lett.*, 3(12):552–554. 75, 76

Tohyama, T., Inoue, Y., Tsutsui, K., and Maekawa, S. (2005). *Phys. Rev. B*, 72:045113. 12

Uhrig, G. S., Holt, M., Oitmaa, J., Sushkov, O. P., and Singh, R. R. P. (2009). *Phys. Rev. B*, 79:092416. 75

Vildosola, V., Pourovskii, L., Arita, R., Biermann, S., and Georges, A. (2008). *Phys. Rev. B*, 78(6):064518. 5

Wan, Y. and Wang, Q.-H. (2009). *Europhys. Lett.*, 85:57007. 5 pages, 1 table, 3 figures. 36

Wang, X. L., Dou, S. X., Ren, Z.-A., Yi, W., Li, Z.-C., Zhao, Z.-X., and Lee, S.-I. (2009a). *J. Phys.: Condens. Matter*, 21:205701. 3, 39

Wang, Y.-L., Shan, L., Fang, L., Cheng, P., Ren, C., and Wen, H.-H. (2009b). *Supercond. Sci. Technol.*, 22(1):015018. 3, 39

Wen, H.-H., Mu, G., Fang, L., Yang, H., and Zhu, X. (2008). *Europhys. Lett.*, 82(1):17009. 1

Wray, L., Qian, D., Hsieh, D., Xia, Y., Li, L., Checkelsky, J. G., Pasupathy, A., Gomes, K. K., Fedorov, A. V., Chen, G. F., Luo, J. L., Yazdani, A., Ong, N. P., Wang, N. L., and Hasan, M. Z. (2008). *Phys. Rev. B*, 78:184508. 3, 128

Xu, G., Ming, W., Yao, Y., Dai, X., Zhang, S., and Fang, Z. (2008). *EPL*, 82(6):67002. 3, 112

Yao, Zi-Jian, Li, Jian-Xin, Han, Q., and Wang, Z. D. (2011). *EPL*, 93(3):37009. 84, 99

Yi, M., Lu, D. H., Analytis, J. G., Chu, J.-H., Mo, S. K., He, R. H., Hashimoto, M., Moore, R. G., Mazin, I. I., Singh, D. J., Hussain, Z., Fisher, I. R., and Shen, Z. X. (2009). *Phys. Rev. B*, 80(17):174510. 118

Yildirim, T. (2008). *Phys. Rev. Lett.*, 101(5):057010. 75

Ying, J. J., Wang, X. F., Wu, T., Xiang, Z. J., Liu, R. H., Yan, Y. J., Wang, A. F., Zhang, M., Ye, G. J., Cheng, P., Hu, J. P., and Chen, X. H. (2011). *Phys. Rev. Lett.*, 107:067001. 63

Yu, R., Trinh, K. T., Moreo, A., Daghofer, M., Riera, J. A., Haas, S., and Dagotto, E. R. (2009). *Phys. Rev. B*, 79(10):104510. 45, 52, 63, 75, 90, 96, 97, 118, 137

Zeng, B., Mu, G., Luo, H. Q., Xiang, T., Mazin, I. I., Yang, H., Shan, L., Ren, C., Dai, P. C., and Wen, H. H. (2010). *Nature Communications*, 1(8):112. 52, 54

Zhang, J., Sknepnek, R., Fernandes, R. M., and Schmalian, J. (2009). *Phys. Rev. B*, 79:220502. 75, 112

Zhao, J., Huang, Q., de la Cruz, C., Li, S., Lynn, J. W., Chen, Y., Green, M. A., Chen, G. F., Li, G., Li, Z., Luo, J. L., Wang, N. L., and Dai, P. (2008). *Nat. Mater.*, 7(12):953–959. xii, 1, 4, 5

Appendix

Appendix A

Appendix

A.1 The Gell-mann Matrices

The λ_i matrices used in the text are presented here:

$$\lambda_0 = \begin{pmatrix} 1 & 0 & 0 \\ 0 & 1 & 0 \\ 0 & 0 & 1 \end{pmatrix}, \quad \lambda_1 = \begin{pmatrix} 0 & 1 & 0 \\ 1 & 0 & 0 \\ 0 & 0 & 0 \end{pmatrix},$$

$$\lambda_2 = \begin{pmatrix} 0 & -i & 0 \\ i & 0 & 0 \\ 0 & 0 & 0 \end{pmatrix}, \quad \lambda_3 = \begin{pmatrix} 1 & 0 & 0 \\ 0 & -1 & 0 \\ 0 & 0 & 0 \end{pmatrix},$$

$$\lambda_4 = \begin{pmatrix} 0 & 0 & 1 \\ 0 & 0 & 0 \\ 1 & 0 & 0 \end{pmatrix}, \quad \lambda_5 = \begin{pmatrix} 0 & 0 & -i \\ 0 & 0 & 0 \\ i & 0 & 0 \end{pmatrix},$$

$$\lambda_6 = \begin{pmatrix} 0 & 0 & 0 \\ 0 & 0 & 1 \\ 0 & 1 & 0 \end{pmatrix}, \quad \lambda_7 = \begin{pmatrix} 0 & 0 & 0 \\ 0 & 0 & -i \\ 0 & i & 0 \end{pmatrix},$$

$$\lambda_8 = \frac{1}{\sqrt{3}} \begin{pmatrix} 1 & 0 & 0 \\ 0 & 1 & 0 \\ 0 & 0 & -2 \end{pmatrix}.$$

Vita

Andrew Nicholson was born to ex-Peace Core volunteers in 1982 and lived until the age of five in Washington D.C. His family subsequently moved to various locations in Eastern North Carolina. Andrew attended the University of North Carolina at Asheville (Asheville, NC) where studied physics and mathematics. During his undergraduate Andrew performed a wide array of research, from radio astronomy at the Pisgah Astronomical Research Institute, to his undergraduate research on voting theory entitled “Voting and Markov Processes”. After graduating as an Undergraduate Research Scholar and with Departmental Distinction in the physics department, Andrew went on a Ph.D. program at the University of Tennessee (Knoxville, TN).

Andrew was awarded a full graduate research assistantship under the supervision of Dr. Adriana Moreo, to study theoretical condensed matter physics with an emphasis on multi-orbital superconductivity. In the course of this work he attended many conferences and was the author/co-author of ten publications. In 2012 Andrew was honored with the “Extraordinary Professional Promise” award. After earning hi Ph.D. in 2012, Andrew will be taking a post-doctoral appointment at Oak Ridge National Laboratory.